HYDROTHERMAL SYNTHESIS OF HIERARCHICAL NiO NANOPARTICLES LOADED SnO2 FOR ACETONE GAS SENSING

SHADY FOUAD AHMED SABER

FACULTY OF ENGINEERING
UNIVERSITI MALAYA
KUALA LUMPUR

2024

HYDROTHERMAL SYNTHESIS OF HIERARCHICAL NiO NANOPARTICLES LOADED SnO₂ FOR ACETONE GAS SENSING

SHADY FOUAD AHMED SABER

DISSERTATION SUBMITTED IN FULFILMENT OF THE REQUIREMENTS FOR THE DEGREE OF MASTER OF ENGINEERING SCIENCE

FACULTY OF ENGINEERING
UNIVERSITI MALAYA
KUALA LUMPUR

2024

UNIVERSITI MALAYA
ORIGINAL LITERARY WORK DECLARATION

Name of candidature: **Shady Fouad Ahmed Saber**

Matric No: **17198160/1 / KGA180033**

Name of Degree: **Master of Engineering Science**

Title of Dissertation ("this Work"):

Hydrothermal Synthesis of Hierarchical NiO Nanoparticles Loaded SnO$_2$ for Acetone Gas Sensing.

Field of Study: **Advance Materials/Nanomaterials (NEC 527: Materials Engineering)**

I do solemnly and sincerely declare that:

(1)   I am the sole author/writer of this Work;

(2)   This Work is original;

(3)   Any use of any work in which copyright exists was done by way of fair dealing and for permitted purposes, and any excerpt or extract from, or reference to or reproduction of any copyright work has been disclosed expressly and sufficiently, and the title of the Work and its authorship have been acknowledged in this Work;

(4)   I do not have any actual knowledge, nor do I ought reasonably to know that the making of this work constitutes an infringement of any copyright work;

(5)   I hereby assign all and every right in the copyright to this Work to the Universiti Malaya ("UM"), who henceforth shall be the owner of the copyright in this Work and that any reproduction or use in any form or by any means whatsoever is prohibited without the written consent of UM having been first had and obtained;

(6)   I am fully aware that if in the course of making this work, I have infringed any copyright whether intentionally or otherwise, I may be subject to legal action, or any other action as determined by UM.

Candidate's Signature   Date: **04/04/2024**

Subscribed and solemnly declared before,

Witness's Signature   Date: **04/04/2024**

Name:

Designation:

HYDROTHERMAL SYNTHESIS OF HIERARCHICAL NiO NANOPARTICLES LOADED SnO₂ FOR ACETONE GAS SENSING

ABSTRACT

The present study has successfully synthesized a cauliflower-like hierarchy microstructure of $NiO: SnO_2$ through a facile hydrothermal method for acetone detection. Among the sensors evaluated, the sensor synthesized with a $NiCl_2 \cdot 6H_2O: SnCl_2.2H_2O$ molar ratio of 5:100, labeled as K5, exhibited exceptional performance in acetone gas sensing, with a response of 1734 at 1000 ppm at 350 °C, two times more than pristine SnO_2. Also, at lower concentrations, the responses were recorded to be 325, 170, 70, and 35 for 200 ppm, 100 ppm, 50 ppm, and 20 ppm acetone balanced in nitrogen, respectively. Moreover, swift response and recovery times of 8 seconds and 2 minutes 18 seconds were recorded at 20 ppm acetone balanced in nitrogen, respectively, at the optimal operating temperature, 350 °C. Also, the sensor was further assessed for its ability to distinguish acetone from other gases by exposing it to equal concentrations of 200 ppm of acetone, carbon dioxide, ammonia, and ethanol, all balanced in nitrogen, and tested at 350°C. Moreover, K5 exhibited exceptional selectivity, with response levels in acetone surpassing those in carbon dioxide, ammonia, and ethanol by factors of 142.74, 143.39, and 2.42 times, respectively. Finally, when tested over five repeated exposure cycles of 200 ppm acetone in nitrogen, K5 displayed remarkable operational stability.

Keywords: Gas Sensor, Acetone Detection, Cauliflower Morphology

SINTESIS HIDROTERMAL NANOPARTIKEL NiO HIERARKI MEMUAT SnO$_2$ UNTUK PENDETEKSI GAS ASETON

ABSTRAK

Kajian ini telah berjaya menghasilkan struktur hierarki berbentuk bunga NiO: SnO$_2$ melalui kaedah hidrotermal yang mudah dan berkesan untuk pengesanan aseton. Di antara sensor yang diuji, sensor yang disintesis dengan nisbah molar NiCl$_2$·6H$_2$O: SnCl$_2$.2H$_2$O sebanyak 5:100, diberi label K5, menunjukkan prestasi yang luar biasa dalam pengesanan gas asetona, dengan tindak balas sebanyak 1734 pada 1000 ppm pada 350 °C, dua kali lebih tinggi daripada SnO$_2$ tulen. Juga, pada kepekatan yang lebih rendah, tindak balas direkodkan sebanyak 325, 170, 70, dan 35 untuk 200 ppm, 100 ppm, 50 ppm dan 20 ppm aseton masing-masing yang dicampur bersama nitrogen. Selain itu, masa tindak balas dan masa kembali yang cepat ialah 8 saat dan 2 minit 18 saat pada 20 ppm aseton masing-masing, pada suhu operasi yang optimal iaitu pada 350°C. Selain itu, sensor juga diperiksa keupayannya untuk membezakan aseton daripada gas lain dengan mendedahkannya kepada kepekatan yang sama iaitu 200 ppm aseton, karbon dioksida, ammonia, dan etanol, semuanya dicampur bersama nitrogen, dan diuji pada 350°C. Selain itu, K5 menunjukkan keanjalan luar biasa, dengan tahap respons dalam asetona melampaui tahap respons dalam karbon dioksida, ammonia, dan etanol sebanyak 142.74, 143.39, dan 2.42 kali ganda, masing-masing. Akhirnya, sensor menunjukkan kestabilan yang baik apabila diuji dalam kitaran pendedahan berulang terhadap gas aseton.

Kata kunci: Sensor Gas, Pengesanan Aseton, Kobis Bunga Morfologi.

TABLE OF CONTENTS

LIST OF FIGURES

LIST OF SYMBOLS AND ABBREVIATIONS

List of Symbols

ΔR: $|Ra-Rg|$ or $|Ra-Rg|$

ΔV_b: Change in barrier potential of metal oxide

2θ: Bragg angle in XRD analysis

A: the cross-sectional area of the sensor

d: Lattice spacing.

F: Gas flow rate

K: XRD constant (taken at 0.89m)

$K\Omega$: Kilo Ohm

L: the length of the sensor

Min: Minutes

R: Resistance

R_a: Resistance of sensor in the air or in the ambient atmosphere

R_g: Resistance of the sensor in target gas

R_o: Resistance of the sensor in the background environment

S: Response of the sensor

Sec: Seconds

T: Absolute temperature

T_0: reference temperature

T_{rec}: Recovery time of the sensor

T_{res}: Response time of the sensor

T_{RT}: Room temperature in Kelvin

λ: wavelength of the XRD Beam

ρ: resistivity

ρ_0: resistivity at the reference temperature

List of Abbreviations

1-D: One-dimensional

2-D: Two-dimensional

3-D: Three-dimensional

DAQ: Data acquisition

DGDE: Diethylene glycol dibutyl ether

DL: detection limit

EDL: Electron depletion layer

EDX: Energy-dispersive X-ray

FCC: Face center cubic

FESEM: Field emission scanning electron microscope

FWHM: The full width at half-maximum

HPMS: Hierarchical porous microspheres

IoT: Internet of things

MFC: Mass flow controller

OVLD: Overload resistance signal

OFS: Optical fiber sensors

ppb: Parts per billion

ppm: Parts per million

PTFE: polytetrafluoroethylene

rpm: Rotation per minute

RT: Room temperature

sccm: Standard cubic centimeters per minute

SEM: Scanning electron microscope

SMO: Semiconducting Metal Oxide

TCR: Temperature coefficient of resistance

VOC: Volatile organic compounds

Wt.%: Weight percent

XRD: X-ray diffraction

CHAPTER 1: INTRODUCTION

1.1   Research Background

In contemporary society, the integration of sensing technologies has become progressively indispensable, propelled by the rapid ascent of the Internet of Things (IoT) and the implementation of automation across various sectors, including industrial production, public health, and military domains. A noteworthy niche within this realm is gas sensing, a significant discipline that focuses on the detection of gas molecules and the subsequent conversion of their concentrations into electrical signals. A primary area of application for gas sensors is the monitoring of flammable and hazardous gases in residential and industrial settings to ensure atmospheric safety (Zhou et al., 2018). Another pivotal application lies within the medical sphere, exemplified by the measurement of acetone concentration in breath to aid diabetic patients (Gupta et al., 2023).

Sensing materials play a pivotal role in determining the efficacy of gas sensors. Within the context of gas sensor applications, there has been an extensive exploration of metal oxide semiconductor materials (SMOs), encompassing both n-type materials (such as ZnO, SnO_2, TiO_2, Fe_2O_3, In_2O, WO_3, etc.) and p-type materials (including NiO, CuO, Co_3O_4, etc.) across various periods. This inclination arises from the inherent advantages offered by metal oxide gas sensors, including elevated sensitivity, cost-effectiveness, adaptable preparation procedures, robustness, and rapid response times (Xiaoxi et al., 2023).

SMOs, at the same time, have several drawbacks and limitations. These materials, for example, need a high working temperature, which vastly limits the applications of SMOs, as high temperatures mostly create energy losses and safety hazards when subjected to

combustible and harmful gases. Moreover, high operating temperatures produce drift in sensor signals, resulting in inaccurate readings or misfires (Deng., 2019). Rapid advancements in nanotechnology and new hurdles have compelled the scientific community to seek new approaches to attain higher sensitivity, better selectivity, greater stability, and lower operating temperature.

Nanomaterials, which encompass various dimensional categories, including 0D nanoparticles, quantum dots, and nanoclusters; 1D nanowires, nanofibers, nanotubes, and nanorods; 2D nanosheets and nanobelts; or 3D nanoflowers, have been introduced as a strategic solution to rectify these limitations. Their exceptional gas-sensing attributes surpass those of traditional materials, elevating their effectiveness in this domain. In addition, due to their larger interaction zone over a cross-sectional area and their geometrically elevated surface-to-volume ratio, nanomaterials with different structures contribute significantly to enhance the adsorbability of different gaseous compounds and increase substantial alteration of electrical characteristics after encountering such analytes (Zhang et al., 2008). Moreover, the doping effect can achieve further improvements toward better gas sensors (Bharathi et al., 2020). Using noble metals or transition metals as additives can affect gas adsorption, catalytic activity, and band bending, drastically enhancing a sensor's performance (Walker, Akbar & Morris., 2019). Also, the heterojunctions of SMO-based gas sensing materials can significantly enhance gas sensing performance. Within the p-n junction, an electron will transition from an n-type substance to a p-type material, generating a depletion zone at the intersection. In a broader sense, As the heterojunction's materials diverge, an equilibrium is established at the Fermi level, accentuated by a rise in electron depletion within the surrounding atmosphere. This phenomenon subsequently induces heightened device resistance in the air, coupled with a substantial resurgence of electrons migrating back to the

conduction band of the gas sensor material upon analyte exposure. This intricate interplay culminates in a discernible augmentation of the gas sensor's operational efficiency, as evidenced by recent research findings (Yang et al., 2021). Furthermore, morphology can also impact the sensing functionality of gas sensors. For the purpose of producing different morphologies, various synthesis processes can be used. These procedures can be categorized into three primary sets: solid-phase method (ex., ball milling (Wu et al., 2018)), vapor method (ex: chemical vapor deposition (Chang et al., 2020)), liquid-phase method (ex: hydrothermal method (Hübner et al., 2011)). The liquid phase method has the advantages of a simple synthesis process, affordability, and controllable grain size; however, productivity remains a massive challenge for this method (Yuan et al., 2019).

SnO_2 is an essential n-type backbone that has been extensively explored over the years because of its broad band gap, affordability, high stability, strong electrical characteristics, and long-term durability (Kim & Lee., 2014). Moreover, the operating temperature of SnO_2 is relatively low and varies between 200 °C and 500 °C, with detection varying from 300 ppm to 500 ppm depending on the detecting gas (Goldoni et al., 2018).

On another front, NiO, a p-type heterostructure, has been demonstrated as an excellent catalyst for selecting volatile organic compounds (VOCs). In addition, NiO has garnered great attention due to its large surface area, gas diffusion, nontoxicity, and chemical stability. It is also considered to be a major research subject for gas sensing applications (John & Kumar, 2023).

Acetone sensors are unique among gas sensor biomarkers as they can precisely analyze acetone levels in the exhaled breath of patients for diabetes diagnosis. Diabetes patients have a much greater concentration of acetone, ranging from 300 ppb to 1800 ppb (Wongrat et al.,

2017). Compared to blood tests and endoscopy, disease detection by analyzing particular VOCs, such as acetone, has sparked significant interest owing to its non-invasiveness and painlessness. It is also considered much more affordable, quick, and convenient (Zhang et al., 2019).

This study aims to fabricate a gas sensor tailored for the detection of acetone, characterized by heightened sensitivity and selectivity with swift response at an appropriate working temperature. This goal will be achieved by developing a heterostructure composite comprising SnO_2 and NiO, which will be synthesized using a facile, cost-effective hydrothermal method.

1.2   Problem statement

Projections indicate a staggering rise in the worldwide occurrence of diabetes within the adult population aged 20 and above, from 10.5% (equivalent to approximately 536.6 million individuals) in 2021 to 12.2% (a total of around 783.2 million individuals)) by 2045. Concurrently, the economic burden of diabetes-related healthcare is projected to escalate exponentially, from an estimated 966 billion USD in 2021 to an astounding 1054 billion USD by 2045 (Sun, H., Saeedi, P. et al., 2022).

Acetone is an important biomarker for diabetes; it is well established that it is present in the human breath of diabetes patients in higher concentrations. Thus, developing a non-invasive, functional, sensitive, selective, and stable acetone gas sensor could be a keystone in determining and monitoring glucose levels and aid in the early detection of diabetes in the future, saving lives and billions of dollars yearly and enhancing the quality of life of millions of people around the globe.

4

Available acetone gas sensors often come with a trade-off between cost and performance. They are expensive to manufacture or exhibit suboptimal characteristics such as poor selectivity towards other gases, instability, slow recovery times, and high operating temperatures. One promising alternative is SnO_2, a widely studied n-type semiconductor known for its large band gap, low cost, stability, good electrical characteristics, and long-term durability. However, pristine SnO_2 gas sensors have limitations, including low selectivity and relatively high working temperatures. Endeavors have been undertaken in this research to overcome these limitations and enhance the gas-sensing capabilities of SnO_2 by combining it with NiO, a catalyst that can lower the working temperature and provide an additional site for analyte gas to react with oxygen ions adsorbed onto the surface, thus shortening response time. Also, combining NiO and SnO_2 can form a p-n heterojunction with greater intrinsic resistance value due to the flow of electrons and holes from SnO_2 and NiO towards each other, respectively. This initial alteration in the resistance state can enhance the response and selectivity of the sensor.

1.3 Research Objectives.

The aim of this research project is to develop a sensitive, selective, swift, and robust gas sensor tailored for acetone detection. The objectives of this research are listed below:

1.   To synthesize n-type SnO_2 and p-type NiO nanostructures and develop a hybrid material from their precursors.

2.   To characterize the gas sensor materials with different analytical methods, including SEM, XRD, and EDX.

3.   To assess NiO: SnO_2 gas sensors' effectiveness in detecting acetone

concentrations across temperature ranges, evaluating selectivity for common breath gases, and examining response and recovery times.

1.4 Scope of research

This research aims to hydrothermally synthesize hybrid sensors of SnO_2 and NiO using facile, hydrothermal methods from their precursors and evaluate their sensitivity, response, and recovery times towards acetone gas of different concentration levels across varying temperatures. In addition, testing the selectivity of the best-performing sensor towards other gases, especially those present in exhaled breath (ex, ethanol, carbon dioxide, ammonia), is a crucial factor for usability in the medical field because acetone is an essential biomarker for many diseases, including diabetes. Furthermore, the repeatability or durability of the best-performing sensor will be assessed by reevaluating its response after several exposure cycles of acetone.

On another track, the synthesized hetero-materials will be characterized using different analytical techniques, including X-ray diffraction (XRD), Scanning electron microscope (SEM), Energy Dispersive X-ray (EDX), and ImageJ Software. Through these assessments, the morphology and chemical composition of the materials will be elucidated, offering valuable insights into the gas-sensing mechanism underlying these sensors.

1.5 Organization of the Thesis

This thesis consists of five chapters. Chapter 1 provides a brief introduction to this research work. This chapter gives the research background, the current issues in this field, the research objectives, and the scope of this research. Chapter 2 provides a comprehensive

overview of the existing literature on various topics related to this research. These topics include metal oxides as gas sensors, the factors influencing gas sensing, the gas sensing mechanism of metal oxides, the synthesis processing routes of metal oxides, the recent developments in acetone gas sensing, and the research gap in gas sensing for acetone detection. Chapter 3 outlines the experimental procedure used in this work. This chapter contains raw materials used in the research, the characterization techniques, and the gas sensing experimental setup, and describes the gas sensing experiments conducted in the research. Moving forward, Chapter 4 presents the findings gleaned from the experimental endeavors, encompassing characterization results of various synthesized samples, outcomes of gas sensing experiments, and elucidation of gas sensing mechanisms. Finally, Chapter 5 encapsulates the research with a conclusive summary and offers recommendations for future explorations.

CHAPTER 2: LITERATURE REVIEW

2.1 Introduction

In recent times, the field of gas sensing has garnered considerable attention from both industry and academia, emerging as a fundamental capability within intelligent detection systems. Gas sensors, notably chemical sensors, hold paramount significance in this domain (Liu, Cheng et al., 2012). A chemical sensor comprises two core components: a transducer and a receptor. While the receptor facilitates the conversion of chemical information into a measurable output signal, the transducer measures this signal which manifests as changes in resistance, frequency, current, or electrical voltage (Witkiewicz et al., 2023). The importance of detecting specific gases lies in the air's composition, which encompasses an array of toxic or combustible gases. This reality underscores the critical nature of precision gas sensing in various industrial settings. Beyond health concerns, these gases also play a pivotal role in environmental contexts, contributing to atmospheric pollution. Furthermore, they hold significant implications within the industrial, medical, and environmental sectors, promptly identifying hazardous gas emissions to prevent potential risks that ensure safe working conditions (Abduljawwad et al., 2023). In this intricate interplay of factors, the evolution of gas sensing technologies acquires profound importance, bridging health and environmental considerations while simultaneously contributing to advancements in industrial processes.

In the present era, traditional detection mechanisms that rely on audible alerts to signal the presence of hazardous gas leaks have become less effective. This shift arises from the increasing necessity for accurate, instantaneous assessments of target gas concentrations rather than relying solely on alarm sounds. Throughout history, a diverse range of gas sensor technologies, including semiconductor, catalytic, electrochemical, optical, and acoustic

sensors, have been employed to detect a wide array of gases. The effectiveness of these technologies hinges upon factors such as sensitivity, selectivity, detection limits, reaction times, and recovery times, collectively defining the overall efficiency of a sensor's performance (Yunusa et al., 2014). Furthermore, this technology has grown in importance due to being utilized in the following territories:

(1) In the medical domain, portable gas-sensing systems find valuable applications as non-invasive tools for breath analysis. Illustratively, breath evaluation by the detection of certain volatile organic compounds can be used to identify various diseases. For instance, diverse NH_3 levels may indicate kidney dysfunction, while the presence of isoprene could suggest heart disease and high levels of toluene may be linked with lung cancer, among others (Singh et al., 2023). Moreover, a pivotal parameter in diagnosing diabetes lies in the precise quantification of acetone concentration, highlighting gas sensors as a promising technology for non-invasive detection (Rodriguez-Torres et al., 2023).

(2) In the automobile industry, oxygen sensors are employed to periodically examine car air-fuel ratio. This sector is especially interested in NO_x sensors because nitrogen oxide (NO and NO_2 are collectively known as NO_x) is a common air pollutant that poses an environmental threat and is mainly produced when fuel burns at high temperatures. So, it is crucial to be able to determine the levels of these gases (Balamurugan, Song & Kim., 2018),

(3) In the realm of environmental monitoring, the demand for sensors such as optical fiber sensors (OFS) has grown significantly, particularly for assessing temporal and spatial changes with a single lead cable without the use of any other electronics in extreme conditions, such as subterranean or subsea pipelines. OFS have emerged as a viable approach for environmental investigations, boasting attributes like resistance to electromagnetic

interference, durability in harsh temperatures and pressures, rapid data transmission, light weight, compactness, corrosion-resistant, and flexibility. Additionally, OFS serves as a potent instrument for enhancing process control efficiency and precisely detecting small leakages that often go undiscovered by traditional methods (Gemeinhardt & Sharma., 2023).

(4) In the supervision of indoor air quality, it is vital to detect unfavorable conditions and implement interventions within buildings to enhance living environments. Presently, smart systems can collect data from gas sensors that assess a range of air quality parameters, including ammonia (NH_3), carbon monoxide (CO), nitrogen dioxide (NO_2), propane (C_3H_8), butane (C_4H_{10}), methane (CH_4), hydrogen (H_2), and ethanol (C_2H_5OH). To ensure healthy living conditions, managing the concentration of these gases becomes indispensable (Marques et al., 2019).

2.2   Metal Oxides as Gas sensors

Theoretically, there are no inherent constraints when it comes to adopting various solid-state gas sensor materials, regardless of their physical, chemical, structural, or electrical attributes. Extensive research has already delved into the performance and characteristics of diverse sensor materials. Prototypes of gas sensors have been tested using a range of materials, including ionic semiconductors, semiconducting metal oxides, solid electrolytes, polymers, ionic membranes, organic semiconductors, and ionic salts. However, there is no conclusive evidence indicating equal effectiveness across all materials for gas sensor applications. With such a vast material landscape to navigate, selecting the most suitable detection material becomes a substantial challenge in the design and fabrication of gas sensors. Furthermore, a gas sensor must satisfy performance-based criteria (such as

sensitivity and selectivity) and reliability-related requisites (such as response time, recovery duration, and stability). These aspects are intrinsically tied to the sensing materials employed, making the material selection, and processing pivotal in the gas sensor development process (Korotcenkov et al., 2007).

Moreover, there is a growing demand for gas sensors that are cost-effective, durable, compact, and energy-efficient, given their versatile applications. Furthermore, the rising requirement for gas sensors with enhanced selectivity and sensitivity has prompted endeavors to identify more suitable materials boasting the necessary surface and bulk properties (Eranna, Joshi, et al., 2004). In this regard, semiconducting metal-oxide (SMO) gas sensors have garnered attention due to their alignment with these requisites. Notably, SMO gas sensors, characterized by size-dependent traits, have emerged as one of the most extensively explored gas sensor variants with their sizes spanning from 1nm to 90nm (Goel et al., 2023).

Numerous metal oxide semiconductors, encompassing both n-type materials (like ZnO, SnO_2, TiO_2, Fe_2O_3, In_2O, WO_3) and p-type counterparts (such as NiO, CuO, Co_3O_4,), have been subjected to scrutiny for their potential in gas sensing applications, yielding mixed outcomes. However, as technology propels forward, fresh obstacles have surfaced, prompting researchers to seek out materials characterized by heightened sensitivity, selectivity, stability, and operational temperature ranges. Hence, nanomaterials were introduced due to their superior gas sensing characteristics to conventional methods.

On a related note, researchers used the p-n junction technique to improve gas-sensing behavior toward a specific analyte by manufacturing a hybrid material made up of one or two metal oxides. According to reviews, the heterojunction created will significantly impact a sensor's sensitivity, response rate, recovery rate, detection limit, and operating temperature.

This study will develop a sensor to detect acetone using SnO_2 nanomaterial as an n-type material infused with NiO as a p-type nanomaterial. acetone is a precious volatile organic compound (VOC) that tracks various health issues, including diabetes. Some composites feature qualities that are not obtained in individual components. For example, composites were found to not only enhance gas sensitivity performance but also show other outstanding gas-sensing properties (Zhang et al., 2023). SnO_2-NiO composite used in this study will highlight such advantages of gas sensors.

Furthermore, SMOs are typically divided into two categories (Korotcenkov., 2007):

1. Transition-metal oxides: This category encompasses compounds like Fe_2O_3, NiO, and Cr_2O_3.

2. Non-transition metal oxides: This group encompasses pre-transition metal oxides like MgO and post-transition metal oxides such as SnO_2.

Due to their large band gaps, pre-transition metal oxides are considered to be relatively inert. Therefore, it is hard to produce electrons or holes. Given the challenges in measuring electron conductivity, they are rarely used as gas sensor materials. However, transition-metal oxides exhibiting d^0 and d^{10} electronic configurations, including binary transition metal oxides like TiO_2, V_2O_5, and WO_3 characterized by the d^0 configuration, as well as post-transition metal oxides such as ZnO and SnO_2 with the d^{10} electronic configuration, are practically employed as gas sensors in real-world applications.

Specifically, SnO_2 and NiO will be covered in the succeeding sections since they will be used in this research.

2.2.1 SnO$_2$ for Gas Sensing

SnO$_2$, or stannic oxide, is a prominent n-type backbone that many researchers have extensively explored over the years due to its porous structure, reduced size, large band gap, high surface area, excellent stability, and good electrical characteristics (Kononova et al., 2023). In SnO$_2$ gas sensors, highly flammable gases, including hydrogen, ethanol, and carbon monoxide, are monitored by electrical resistance changes. At around 250-350°C, the adsorbed oxygen with combustible gases reaction causes an electrical resistance shift. The gas detection process of SnO$_2$ gas sensors relies on the reaction occurring at the surface. (Suematsu & Ma et al., 2018).

Moreover, SnO$_2$ stands out with a substantial band gap of 3.6 eV, drawing significant attention owing to its remarkable chemical and thermal stability. Moreover, its exceptional sensitivity enhances its attractiveness as a sensing material for the detection of hazardous gases. However, it's essential to note that while SnO$_2$-based gas sensors have garnered interest, they do face certain limitations. These include challenges such as reduced selectivity and a relatively elevated operational temperature, which could potentially constrain their wider applicability (Khuspe & Navale et al., 2013; Sakhare & Khuspe et al., 2013).

Numerous endeavors have been undertaken to enhance the gas detection capabilities of this n-type semiconductor, including introducing noble gases, doping of metal components, and conjunction with other metal oxides. Among these strategies, combining SnO$_2$ with a second semiconductor metal oxide to generate an n-n, p-n heterojunction is a suitable approach that may considerably increase gas sensing ability (Murugan, Subramanian & Padiyan., 2014).

This work will highlight the SnO_2-NiO composite and will be extensively discussed later in the literature review. The subsequent section will provide a comprehensive overview of NiO, which will aid in understanding the advantages of combining it with another thermally stable SMO, in particular, SnO_2.

2.2.2 NiO for Gas Sensing

NiO stands as a p-type semiconductor with a cubic structure, renowned for its diverse applications encompassing catalysts, battery materials, electrochromic coatings, active optical fibers, fuel cell electrodes, and more (Zhu et al., 2012). This remarkable versatility has driven substantial interest in its properties. Furthermore, NiO has garnered heightened attention, particularly within the domain of gas sensors, due to its distinct attributes. Notably, it boasts a reasonably wide band gap ($Ev = 3.6\text{-}4.0$ eV) and exhibits significant changes in electrical conductivity through surface-based chemical reactions. These inherent features position it exceptionally well for gas-sensing applications (Zhao et al., 2013).

However, despite its prowess, NiO's gas sensing capabilities, especially when compared to some n-type semiconductor metal oxides (SMOs), remain relatively modest. Challenges persist, especially concerning the cost-effective and large-scale fabrication of high-quality standalone one-dimensional NiO nanoparticles. Nevertheless, NiO has showcased impressive catalytic prowess in volatile organic compound oxidation, propelling the necessity for enhancing its gas-sensing attributes. To this end, the creation of NiO nanostructures boasting extensive surface areas and optimized gas diffusion proves pivotal. Among the array of factors in nanomaterial manufacturing, morphology alteration takes precedence.

Furthermore, augmenting NiO through multi-doping and the construction of heterostructures alongside n-type SMOs has ushered in improved gas sensing characteristics (Kumar et al., 2018; Mokoena et al., 2019). Notably, the research landscape has witnessed an exponential surge in studies focusing on doped NiO and heterostructures in recent years. In this context, this study embarks on showcasing compelling evidence for the excellence of the NiO: SnO_2 nanocomposite hybrid material in acetone gas sensing. This work will demonstrate and provide insightful evidence on how the NiO: SnO_2 nanocomposite hybrid material can be excellent for acetone gas sensing.

2.3   Factors Influencing Gas Sensing

2.3.1   Morphology

Surface morphology, particularly nanostructure, has an important impact on the gas-sensing performance of SMOs. Several unique or improved qualities arise when the size of the most investigated materials is shrunk to nanoscale levels. Given their large specific surface areas, conducting metal oxides of 1D nanostructures are suitable for gas-sensing applications (Lu et al., 2011). Numerous attributes defining polycrystalline materials in the context of gas sensor advancements become less significant when applied to one-dimensional structures, as the latter are composed of single crystals. Elements such as film thickness, porosity, grain size, grain network, grain boundaries, agglomeration, and texture, which hold importance in conventional scenarios, experience a shift in relevance. Conversely, the core structural and morphological factors shaping one-dimensional structures encompass geometric dimensions, the profile of these structures, and the crystallographic planes that underpin their composition (Korotcenkov, 2008).

Researchers have analyzed nanostructures with novel morphologies, which is considered one of the fundamental variables that affect their characteristics. For instance, in a study conducted by (Li et al., 2009), the sensor's response and selectivity of the as-synthesized mesoporous In_2O_3 nanorods displayed outstanding gas-sensing characteristics towards ethanol (C_2H_5OH). The simple sol-gel technique was used to make mesoporous In_2O_3 nanorods formed of several tiny, highly-ordered crystal nanomaterials. The results showed that mesoporous In_2O_3 nanorods have a response intensity of 8.43 at 100 ppm ethanol, which is higher than other conventional In_2O_3 nanowire-sensors, and 1.71 towards 500 ppb of ethanol. This study implies how significant morphological alterations such as size, porosity, structure geometry, and other morphological aspects are in gas-sensing practices. The following will discuss the effect of size, porosity, and structure geometry in more detail.

Moreover, the impact of morphologies in nanosized metal oxide materials on their practical applications cannot be understated. It is crucial to engineer meticulously controlled morphologies that offer a high surface-to-volume ratio, superior performance, and heightened reactivity. Extensive exploration of various SnO_2 morphologies, such as nanoparticles, hollow spheres, nanosheets, nanoflowers, polyhedrons, and 3D hierarchical nanostructures, has transpired. These morphologies intricately contribute to the gas-sensing and photocatalytic attributes, demanding adjustments in size and shape, including, the reduction of nanorod or nanosheet dimensions—to yield significant performance enhancements (Kaur, Bhatti & Singh, 2019). To elevate the sensitivity of chemiresistive gas sensors, the incorporation of 1D nanostructures like nanorods, nanofibers, nano ribbons, and nanowires emerges as a strategic approach (Betty et al., 2023). Their inherent larger surface-area-to-volume ratio plays a pivotal role in enhancing gas analyte absorption and inducing substantial changes in electrical characteristics upon analyte exposure (Khomarloo et al.,

2024). The diameter size of these 1D nanostructures also has a noteworthy impact on gas-sensing performance. A smaller diameter translates to a larger surface-to-volume ratio, thereby yielding more active sites, better charge carrier transfer, and increased surface energy. Notably, grain size and crystallinity, coupled with the constrained diameter of nanostructures, significantly steer gas sensing performance. A proportional grain size to double the Debye length for polycrystalline 1D nanostructures like electro-spun nanofibers results in exponential enhancements (Yang, Myung & Tran, 2021).

Furthermore, research conducted by Akhir et al. (2019) demonstrated the paramount role of crystallite size. Smaller crystallite sizes translated to higher sensitivity (28.69) and faster response times (20s) compared to their larger counterparts in SnO_2 nanostructures. A straightforward hydrothermal method yielded tin oxide (SnO_2) nanorods, nanocubes, and nanospheres, with an additional 3% palladium (Pd) doping for ethylene gas sensing evaluation. This study substantiates the significance of grain size and crystallite size in gas sensing, impacting semiconductor gas sensor response dynamics. Diminished crystallite sizes constrict conduction area, bolster charge depletion layer thickness, and significantly amplify gas response behavior.

In addition, the exploration of 1D oxide structures such as nanowires, nanoflowers, and nanorods presents promising prospects for gas sensing applications, attributed to their unique surface properties, anisotropic shapes, and scalability for technology (Simo et al., 2017). Shaalan et al. (2011) researched SnO_2 microwires, nanowires, and rice-shaped nanoparticles through thermal evaporation. The microwire and nanowire widths stood at 2 μm and 50-100 nm, respectively, maintaining a similar length of 20 μm. The nanoparticles measured approximately 100 nm. These compounds showcased a crystalline rutile structure. A

comparison between SnO_2 particle and wire-like structures revealed significant reliability and sensitivity improvement in the latter's gas sensing capabilities.

Additionally, Tan and Zhang (2023) introduced highly sensitive and stable ethanol sensors based on Co-doped SnO_2 nanobelts. Their fabrication utilized a chemical vapor deposition, with altered morphology and flexibility. At the optimum temperature of 300 ℃, ethanol senors demonstrated high sensitivity, quick response, and good stability. Notably, Co-doped SnO_2 nanobelts held promising potential for sensor applications.

Moreover, 3D porous SnO_2 structures in the form of blooming nanoflowers were generated through a straightforward hydrothermal method employing various surfactants. These structures yielded enhanced ethanol-sensing behaviors marked by lower operating temperatures, rapid reactions, and swift response-recovery times, attributed to their multitude of mesopores. This abundance of mesopores led to heightened porosity, promoting ethanol gas adsorption and diffusion (Zhao et al., 2018).

On another track, porosity takes center stage as it influences interactions within the gas-sensing matrix. Enhanced porosity curtails interactions with non-overlapping necks during the gas collision, minimizing the occurrence of encapsulated zones that remain detached from the gas-sensing layer's environment. These zones operate independently in terms of resistance relative to surrounding gas (Korotcenkov, 2008). Investigating SnO_2 sensors employing successive ionic layer deposition highlighted the gas sensitivity enhancement achieved through reduced crystallite (grain) sizes. To optimize performance, gas-sensing matrices should exhibit high porosity and minimal agglomeration. Conversely, heavily agglomerated structures trigger counterproductive scenarios where the advantage of smaller

grain size (crystallite) diminishes. Smaller grains agglomerate more tightly, impeding gas permeability (Korotcenkov, 2003).

In summary, in the realm of nanosized metal oxides, the synergy of size, porosity, and structure geometry intricately influences gas sensing capabilities. As scientific inquiry propels innovation, these findings pave the way for advanced sensing materials, catalyzing the evolution of gas sensing technologies.

2.3.2 Doping with Transition Metals

Many studies have been conducted to improve the sensitivity and selectivity of metal oxides by doping them with appropriate transition metals. Doping of impurities causes the band gap to be tuned and the electrical and optical characteristics to be improved. However, it can also affect morphology, which boosts the surface-to-volume ratio. Consequently, additional interaction centers between gas and metal oxides emerge (Bharathi et al., 2020).

Bharti et al. (2017) synthesized needle-shaped Ni-doped SnO_2 nanocrystals using the sol-gel chemical precipitation method at shallow temperatures (500°C). The Ni-doped SnO_2 demonstrated room-temperature ferromagnetism and a reduction in band gap with higher Ni doping levels. Furthermore, the study also revealed the varying size of nanoparticles from 110 nm to 140 nm with high porosity. Hence, these nanoparticles can be employed in a range of applications, such as solar cells and gas sensing. Due to the doping material, the morphology will comprise two distinct types of chemical structure, causing the particles to agglomerate and form a cluster.

In another example, Al-Hardan et al. (2013) observed that the 1 atomic% (at%) Cr doped ZnO sensor had a substantially stronger reaction to oxygen than the undoped one. In addition,

the authors also observed that a Cr-doped ZnO gas sensor had outstanding reliability after being exposed to 500 ppm acetone for 15 minutes, indicating the capacity of the developed ZnO gas sensor to work for an extended amount of exposure time. The undoped and 1%-Cr doped ZnO surge time was 210 and 70 s, respectively, whereas the recovery times were 170s and 95s. The enhancement is due to improved gas diffusion and a quicker rate of surface response for gas sensing after Cr doping.

2.3.3   Doping with Noble Metals

To enhance the gas sensing performance, precious metals such as palladium, platinum, gold, and silver have been employed to modify the semiconducting metal oxides (SMOs) by leveraging catalytic and sensitization effects. This action leads to a decrease in the Fermi level, which in turn increases the depletion layer within the SMOs (Ma et al., 2017). The addition of these noble metals can impact gas adsorption, catalytic activity, and the bending of energy bands in various ways. When a noble metal comes into contact with another material, there is an exchange of charges until the Fermi levels of both materials are in equilibrium. Electrons tend to accumulate in the noble metal, leading to the formation of a depletion region in the metal oxide. Noble metals have a higher number of mobile charge carriers compared to metal oxides, allowing electrons to redistribute themselves and neutralize any charge accumulation near the junction where the two materials meet. This interaction results in the creation of a "Schottky potential barrier" in the electrical structure (Walker, Akbar & Morris, 2019).

Moreover, in a study by Tofighi et al. (2019), a microfluidic reactor with efficient micromixers was utilized to synthesize single-metal Au and Pd nanoparticles (NPs) and

bimetallic AuPd nanoalloys. These nanoparticles were subsequently supported on SnO_2. Gas sensing experiments conducted at 300°C, comparing pure Au, AuPd alloy, and pure Pd NPs supported on various SnO_2 substrates, revealed that the loading and composition of noble metals significantly influence the gas sensing capabilities. The study's observations on the sensitization effect indicated that the presence of oxygen spill-over improved the sensing characteristics of SnO_2 surfaces when paired with Au. In contrast, for Pd-containing loadings, the control of the Fermi level played a decisive role in determining the sensing properties. The presence of Au NPs yielded enhancements in all sensor signals compared to the unmodified material. Beyond alloy composition, fine-tuning the concentration of noble metals, the support materials, and operational temperature could open up further possibilities for noble metal NP-based gas sensors.

Furthermore, Zhang and Xiao (2019) effectively produced ZnO and Au/ZnO hierarchical porous microspheres (HPMSs) using a one-step hydrothermal method followed by annealing. The gas response and response-recovery speed of Au/ZnO HPMSs outperformed those of pure ZnO HPMSs. The introduction of Au/ZnO HPMSs led to a more significant resistance shift in response to acetone, attributed to the formation of a Schottky junction and a more pronounced depletion layer. These factors resulted in an improved reaction compared to pure ZnO. Additionally, the study indicated that ZnO HPMSs doped with 0.5 mol% Au NPs displayed a marked enhancement in gas response when compared to other Au-doped ZnO composites. This improvement was attributed to the optimal amount of Au doping (0.2-0.5 mol%) influencing the results.

2.3.4 Heterojunctions

For more performance improvements, different heterostructure materials (secondary materials) can be added to the backbone materials (base materials) to form a heterojunction that drastically enhances a sensor's response and selectivity. In general, the backbone material is an n-type material where the predominant carriers of charge are electrons like SnO_2, ZnO, and TiO2, and the heterostructure has the potential to be either n-type or p-type. Nonetheless, the utilization of p-type backbones, such as CuO and NiO, is infrequent due to their lower stability and their tendency to show responses that are proportional to the square root of the n-type backbone (H bner et al., 2011).

As an illustration, Li et al. (2019) adeptly fabricated meticulously structured porous nanobelts infused with CuO, introducing p-type CuO| n-type ZnO heterojunctions through a technique combining partial cation-exchange and thermal oxidation. This innovative approach significantly amplified their sensing performance. The amount of CuO infusion was meticulously regulated by adjusting the exchanged Cu^{2+} cations. Furthermore, the distribution of Cu throughout the porous ZnO nanobelts was uniform. In comparison to the unperturbed porous ZnO nanobelts, the resulting porous CuO-ZnO heterojunctions showcased elevated sensing capabilities toward volatile organic compounds (VOCs), specifically ethanol, acetone, and formaldehyde.

Moreover, recognizing the evident advantages of NiO as a promising binding option for constructing p-n heterojunctions in gas sensing applications, (Xu et al., 2019) devised a precisely structured one-dimensional α-MoO_3@NiO core-shell p-n heterostructure by attaching porous NiO nanosheets onto α-MoO_3 nanobelts through a straightforward approach. Through gas sensing experiments, it was revealed that the inclusion of NiO nanosheets significantly enhanced the sensing capabilities of the α-MoO_3 nanobelts,

attributed to the formation of p-n heterojunctions. Notably, in comparison to unmodified α-MoO₃ and pristine NiO, the gas sensing response of the α-MoO₃@NiO nanocomposites exhibited substantial improvement.

Such heterojunctions mentioned above manipulate sensor transduction pathways, which increases sensitivity. In addition, electronic structure and charge distribution due to formations of heterojunctions and composites are also responsible for enhancing sensitivity and selectivity (Walker, Akbar & Morris., 2019).

2.4 Gas Sensing Mechanism of Metal-Oxides

2.4.1 Gas Sensing Mechanism of n-type Metal-Oxides

The resistance-type gas sensor's sensing mechanism is commonly described by the surface-depletion model, a framework often employed in the field (Zhang and Mubeen et al., 2008). Within n-type semiconductor metal oxide sensors, the interaction with oxygen molecules from the environment results in the confinement of conduction electrons at the surface (Kondo et al., 2017). These oxygen molecules, when trapped, engage in electron exchange with the surface layer's conduction band, producing negatively charged chemisorbed oxygen ions like O_2^-, O^-, and O^{2-}. Consequently, a decline in sensor conductivity ensues, accompanied by the bending of the energy band upwards. This phenomenon contributes to the formation of an electron-depleted region on the surface, characterized by an energy barrier (Li et al., 2015). The decrease in sensor conductivity corresponds to an increase in resistance (Li et al., 2019).

Upon exposure to oxidizing gases like NO or O_3, the chemisorbed oxygen ions seize electrons, leading to an expansion of the depletion layer. This process heightens the potential

23

energy barrier and augments surface resistance. Conversely, when the target gas is a reducing agent such as NH_3, H_2S, or acetone, the chemical reaction liberates electrons that are infused into the electron depletion layer (EDL). As a result, the EDL diminishes, leading to a decrease in the potential energy barrier and, consequently, an overall reduction in surface resistance.

In the context of H_2S detection, a study conducted by Xiao et al. (2018) involved the fabrication of mesoporous SnO_2. The interaction between the n-type gas sensor and the target gas can be elucidated through a straightforward electron depletion model. When SnO_2 nanograins come in contact with oxygen molecules in the air, these molecules infiltrate the mesopores of the nanograins, enveloping the entire surface. This interaction results in the capture of electrons from the nanograins, prompting the formation of an EDL and the establishment of a potential energy barrier on the surface. Upon exposure to H_2S, a pronounced increase in the voltage across the loading resistor is observed due to the return of electrons from H_2S to SnO_2. The ensuing reaction mechanism involves the chemisorbed oxygen and SnO_2 nanograins reacting with H_2S to yield SO_2 and SnS_2 as indicated by equations 2.1 and 2.2.

$$2H_2S + 3O_2 \rightarrow 2H_2O + 2SO_2 \tag{2.1}$$

$$2H_2S + SnO_2 \rightarrow SnS_2 + 2H_2O \tag{2.2}$$

Figure 2.1 depicts a standard response-recovery curve showcasing the behavior of n-type ZnO nanoparticles upon exposure to 1000 ppm of the reducing gas acetone at 400 °C.
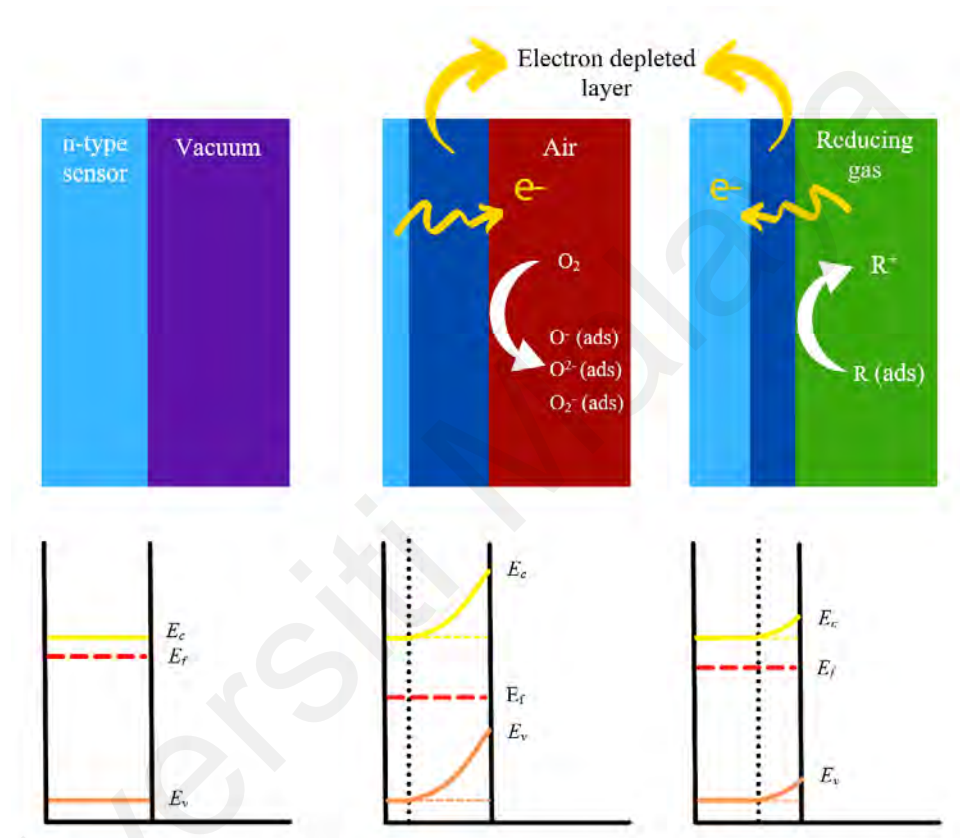
Moreover,

Figure 2.2 summarizes the gas sensing mechanism for an n-type SMO gas sensor when exposed to a reducing gas.
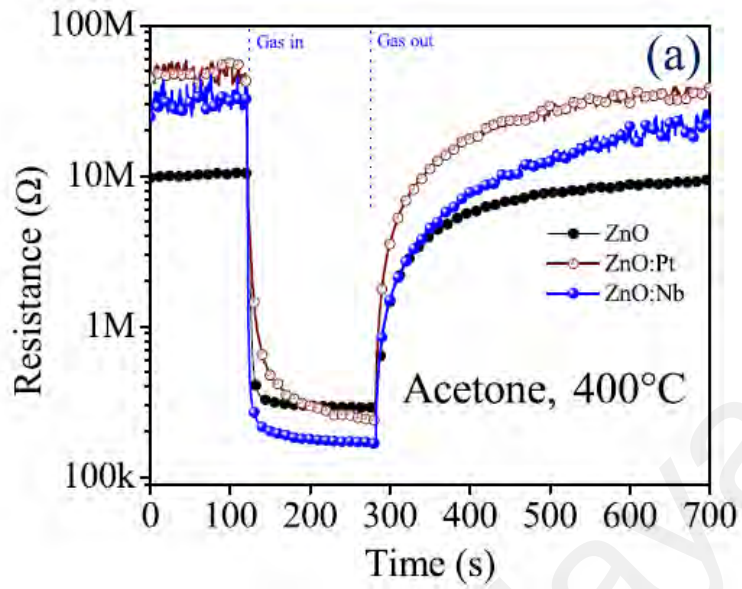
Figure 2.1 Response-Recovery curve of n-type ZnO, ZnO:Pt, and ZnO:Nb nanoparticles toward 1000 ppm of the reducing gas, acetone, at 400 °C (Reprinted with permission from (Wongrat et al., 2017)).
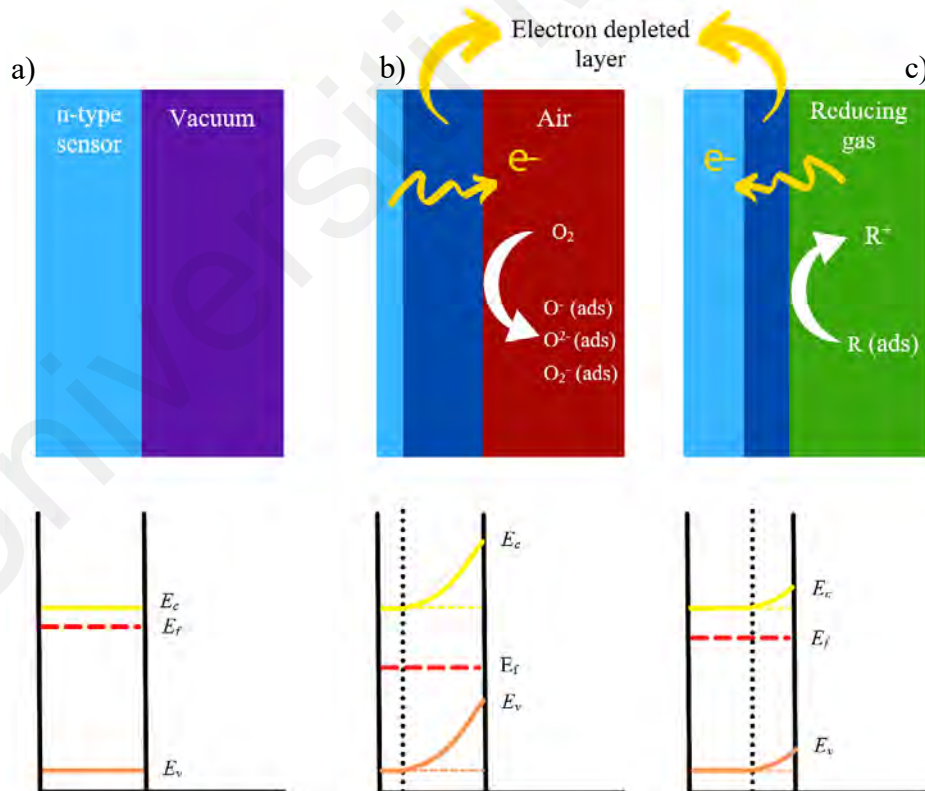
Figure 2.2 The gas sensing mechanism stages of an n-type gas sensor and the corresponding changes in the Fermi level when in a) the intrinsic state, b) in air, and c)after exposure to a reducing gas. (Adopted from Arafat et al., 2014 and C.Wang et al., 2010)

2.4.2　Gas Sensing Mechanism of p-type Metal-Oxides

In contrast to n-type materials, when a p-type SMO comes into contact with air under room temperature conditions, the adsorbed oxygen molecules on the surface of the p-type SMOs generate oxygen ions in the form of O_2^-, thereby absorbing electrons from the conduction band. This electron uptake contributes to an increased density of hole carriers, resulting in the reduction of the Fermi level of the surface layer closer to the valence band. With the emergence of an accumulated layer of holes, the conductivity of p-type SMOs escalates, leading to a decline in sensor resistance (Li et al., 2019). In the presence of oxidizing gases, the hole accumulation layer expands due to the absorption of more valence-band electrons by the gas molecules. This phenomenon enlarges the electrical transport pathway, ultimately leading to a decrease in resistivity. Conversely, when a reducing gas is introduced, the adsorbed oxygen disperses from the SMO surface as gas molecules interact with them, yielding volatile compounds. As a result, the captured electrons revert to the valence band, resulting in electron-hole compensation and a reduction in the hole accumulation layer. This decrease prompts an increase in resistance (Choi et al., 2014). For instance, when a p-type NiO, characterized by holes as the primary carriers, is exposed to air containing 21% oxygen gas, electrons are extracted from NiO and attracted to the oxygen molecules covering the material's surface. This process generates additional holes, thereby augmenting electrical conductivity and forming a depletion layer. This increase in electron mobility causes a reduction in the potential energy barrier's height, leading to lower sensor resistance (Mokoena et al., 2019). Subsequently, when the sensor encounters a reducing gas like acetone, electrons are reintroduced into the material, recapturing holes from the depletion layer, consequently causing an increase in resistance. For instance, Figure 2.3 visually illustrates a typical response-recovery curve for p-type NiO nanoparticles when exposed to

100 ppm of the reducing gas acetone at 260 °C. Finally, Table 2.1 encapsulates the alterations in electrical characteristics of n-type and p-type SMOs upon exposure to distinct environments containing reducing and oxidizing gases.
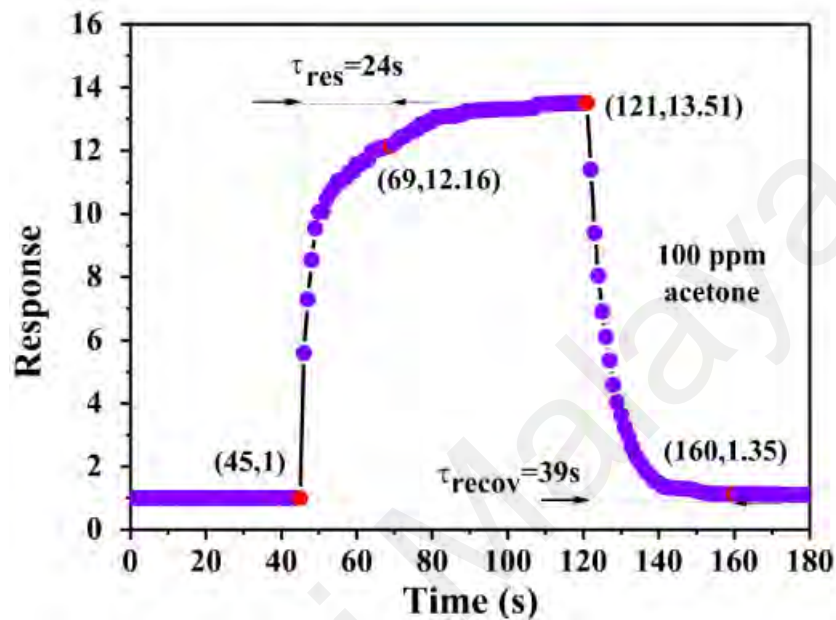
Figure 2.3 Response-Recovery curve of p-type NiO nanoparticles toward 100 ppm of the reducing gas, acetone, at 260 °C (Reprinted with permission from (Lu et al., 2016)).

Table 2.1 Summary of the electrical properties' changes for n-type and p-type SMOs in reducing and oxidizing gases.

Type of Target Gas	n-type SMO (Ex: ZnO, SnO$_2$, TiO$_2$,)	p-type SMO (Ex: NiO, CuO, Co$_3$O$_4$)
Reducing Gas (Ex: C$_3$H$_6$O, C$_2$H$_6$O, CH$_4$,CO, CO$_2$, NH$_3$, H$_2$)	Resistivity decreases	Resistivity increases
Oxidizing Gas (Ex: NO$_x$, O$_2$, Cl$_2$)	Resistivity increases	Resistivity decreases

2.4.3   Gas sensing Mechanism of Heterojunction Metal-Oxides

To begin, upon the formation of the hetero p-n junction, a transfer of electrons from the n-type to the p-type region and an opposite movement of holes from p-type to n-type transpire until equilibrium is achieved. Consequently, during this initial stage, the electron concentration within the n-type's conducting band diminishes. Subsequently, in the presence of air, the high electronegativity of oxygen prompts the capture of electrons from both the n-type and p-type segments of the hetero-material. This action results in further electron depletion in the n-type region and intensified p-type characteristics. These concurrent phases lead to a substantial elevation in sensor resistance when exposed to air, potentially resulting in complete electron depletion within the n-type's conduction band (R_{air} increased).

Additionally, when a reducing gas, such as acetone, is introduced, electrons are returned to the material, thereby lowering the electronic barrier, and causing a rapid reduction in resistance (R_{gas} decreased). This favorable change is expected to correspond to heightened sensitivity, considering the response ratio is defined as R_{air} / R_{gas} (Lu et al., 2017). For instance, the combination of SnO_2 and NiO composite nano-webs is subjected to air. The electrons in SnO_2 and the holes in NiO disperse in opposite directions due to the steep gradient of their respective carrier concentrations. Upon reaching equilibrium, the energy band within the depletion layer undergoes bending. Consequently, electrons migrate from n-type SnO_2 to p-type NiO, while holes shift from NiO to SnO_2 until Fermi levels align. This process results in the expansion of the depletion layer and heightened resistance. Upon exposure to reducing ethanol gas, interactions occur with oxygen ions, leading to the transfer of electrons back to the bulk, thus diminishing the sensor's resistance (Wang et al., 2016). Likewise, within the context of the ZnO/C_3O_4 composite, the phenomenon unfolds as described earlier. Electrons migrate from n-type ZnO to p-type C_3O_4, while holes move in

the opposite direction until Fermi levels equalize. As a consequence, depletion layers form in ZnO, while accumulation layers expand within C_3O_4. Upon encountering acetone, generated electrons contribute to the electron density on the ZnO surface, simultaneously reducing hole density on the C_3O_4 surface. The introduction of a small amount of C_3O_4 narrows ZnO's depletion layer in acetone relative to air. Furthermore, the potential barrier height discrepancy between the p-n junction and the n-n junction amplifies during acetone adsorption and desorption, substantially influencing sensing capabilities (Zhang & Yang et al., 2019). Figure 2.4 shows a schematic diagram of the acetone sensing mechanism of ZnO/C_3O_4.
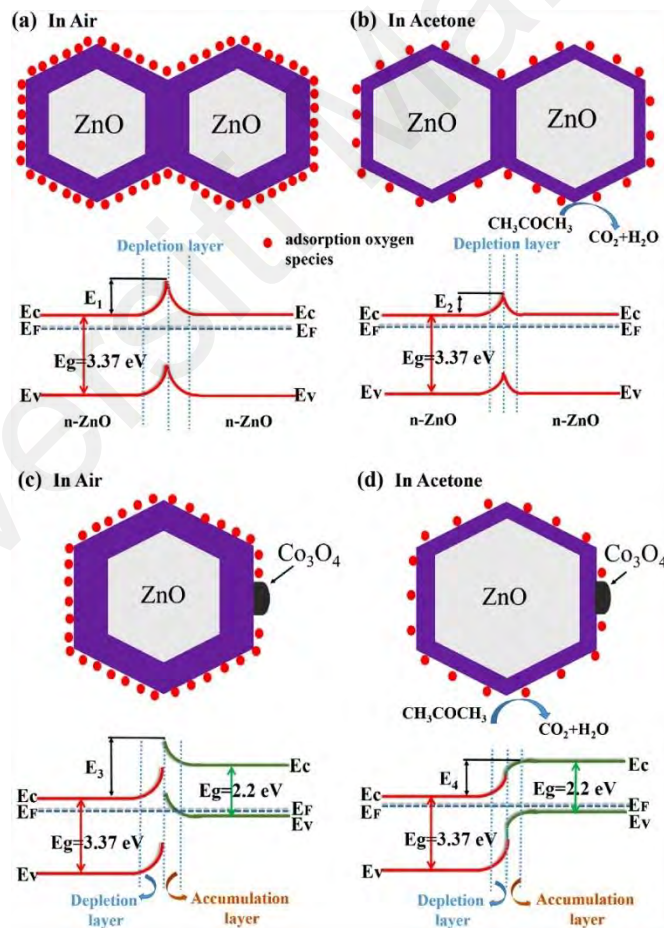
Figure 2.4 A schematic diagram of acetone gas sensinsing mechanism for ZnO and the heterostructure ZnO/C_3O_4: (a,c) in air and (b,d) in acetone (Reprinted with permission from (Zhang & Yang et al., 2019).

2.5   Synthesis Processing Routes of Metal-Oxides

Metal oxide nanoparticles can be effectively fabricated through a diverse array of techniques encompassing both physical and chemical processes. These methodologies yield nanoparticles with a wide spectrum of characteristics, including elemental composition, size, shape, and inherent chemical or physical traits (Haldorai & Shim, 2014).

As illustrated in Figure 2.5, these processing routes can be classified into several categories: (1) wet processing techniques such as hydrothermal, ultrasonic irradiation, electrospinning, anodization, and sol-gel, (2) solid-state processing including solid-state chemical reactions, dry plasma etching, and nano-carving, (3) molten-state processing involving molten-salt methods, and (4) vapor phase processing encompassing carbothermal reduction, chemical vapor deposition, thermal evaporation, aerosol techniques, RF sputtering, and molecular beam epitaxy (Arafat et al., 2012).

For the specific scope of this project, the hydrothermal synthesis approach has been chosen as the preferred processing route. This method will be examined in further detail in the upcoming subsection, owing to its distinct advantages and relevance to the project's objectives.
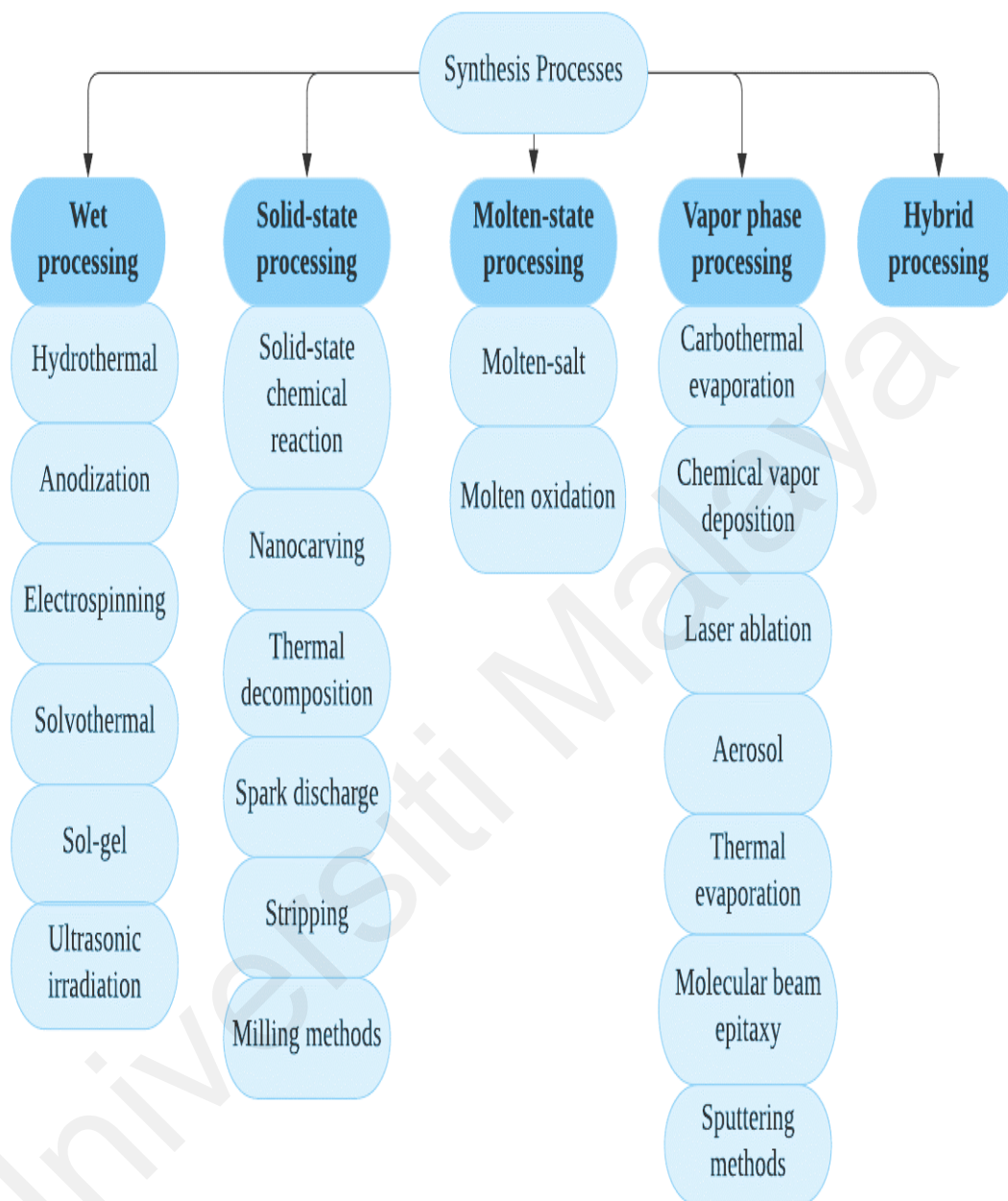
Figure 2.5 Synthesis processes of metal oxide nanoparticles.

2.5.1   Hydrothermal Synthesis

Hydrothermal synthesis was initially used to create crystalline structures in the 1970s. First, the reactants are mixed in a sealed container with water as the reaction medium. Then, the reaction is carried out at high temperatures and pressures. This process can speed up ion

reactions and boost the hydrolysis reaction. This process's benefits include low cost, moderate reaction conditions, and simple device control. In addition, the result's morphology, structure, and qualities may be well manipulated by altering the experimental conditions (temperature, pressure, time, reaction medium, etc.) (Guo and Yao et al., 2015).

This process is also environmentally favorable as the reactions occur in a closed container, and the contents can be collected and reused after cooling to room temperature (Liu et al., 2007). Furthermore, since it is a simplified process and can produce free-standing nanostructures, Vanalakar et al (2018) adopted this method to fabricate ZnO thin films with nanorods.

Finally, to optimize the synthesis procedure, surfactants can be introduced, constituting a remarkably efficient approach to crafting metal oxides showcasing diverse morphologies. However, surfactants might limit the development of the product during the procedure. Examples of the processing route and details of the fabrication of nanostructures with various morphologies are given in Table 2.3.

2.6   Acetone for Gas Sensing

Acetone stands as a notable volatile organic compound (VOC) reagent extensively employed across industries and laboratories for tasks such as plastic dissolution, paraffin purification, and tissue dehydration within the pharmaceutical realm. Despite its industrial utility, acetone exhibits anesthetic impacts on the central nervous system and possesses the potential to induce harm to vital organs like the liver, kidneys, and pancreas in living organisms. Consequently, the vigilant monitoring of acetone concentrations within both the environment for health considerations and workplace settings for safety purposes emerges as

a critical imperative (Song, Wang & Yang, 2012). Moreover, acetone can also be used as a solvent and extraction reagent. A high concentration of acetone in the air (>10,000 ppm) may induce cephalalgia and nausea (Al-Hardan, Abdullah & Aziz., 2013).

Furthermore, the detection of acetone holds the potential to serve as a biomarker for certain illnesses and diseases, as highlighted (Masikini et al., 2020). The subsequent section will delve into a comprehensive discussion regarding the successful utilization of acetone as a biomarker.

2.6.1 Acetone as a Biomarker

Human breath includes volatile VOCs, some of which are recognized as biomarkers because their content may be legitimately associated with specific ailments or medical issues and can provide fundamental data to investigate or diagnose specific diseases (Masikini et al., 2020). In Table 2.2, concentrations of acetone and other analytes, identified as breath biomarkers, are presented, derived from clinical investigations. These studies encompassed experiments conducted on both control groups or healthy adults and individuals with specific medical conditions such as diabetes, schizophrenia, or lung cancer. Notably, the data were drawn from studies conducted by Deng et al. (2004), Ulanowska et al. (2011), and Popa et al. (2015). These studies utilized distinct participant groups, with Deng et al. (2004) drawing from 15 controls and diabetes patients, Popa et al. (2015) reporting values from 15 healthy adults and adults with schizophrenia, and Ulanowska et al. (2011) compiling data from 86 healthy adults and 137 adults with lung cancer. Although the health status of control subjects in the study by Deng et al. (2004) remains unspecified, control subjects in the investigations conducted by Ulanowska et al. (2011) and Popa et al. (2015) were confirmed as disease-free

individuals without a history of other medical conditions, and they were also nonsmokers (A.Baharuddin et al., 2019).

Table 2.2 Concentrations of biomarkers from breath of healthy individuals and patients with diseases (A.Baharuddin et al., 2019).

Biomarker	Concentration of the gas for control subjects (ppb)	Concentration of the gas for patients with the disease (ppb)	Type of disease	Reference
Acetone	200	1800	Diabetes	(C.Deng et al., 2004)
Ethanol	4.50	12.80	Lung cancer	(A.Ulanowska et al., 2011)
Ammonia	0.29	2.02	Schizophrenia	(C.Popa et al., 2015)

Among gas sensor biomarkers, acetone sensors have added benefits for precisely analyzing acetone amounts to diagnose diabetes. Patients with diabetes have a considerably higher acetone concentration in their exhaled breath, ranging from 300 ppb to 1800 ppb (Wongrat et al., 2017). Disease diagnosis by analyzing certain VOCs, such as acetone, has received widespread interest due to its non-invasive and painlessness and its convenience, speed, and cost-effectiveness compared to blood tests and endoscopy (Zhang et al., 2019).

The concentration of acetone in exhaled breath exhibits notable variations in unmanaged diabetic patients compared to healthy individuals, particularly during regular overnight sleep and extended fasting. In fact, the concentration in diabetic patients can increase up to fivefold during sleep and nearly 20-fold after extended fasting. Furthermore, following a protein-rich

meal, acetone concentration decreases and reaches a minimum point after approximately 4 hours (Righettoni et al., 2013).

For individuals with insulin-dependent diabetes, heightened acetone production and ketogenic flux in the liver lead to an elevation in circulating ketone bodies, including acetoacetate, beta-hydroxybutyrate, and acetone itself. These ketone bodies serve to distribute stress hormones or maintain the fasting response in instances of declining insulin levels among healthy individuals (Turner et al., 2009). Notably, the presence of acetone in breath can provide insights into diabetes-related metabolic processes. This is because gas-phase acetone in the blood connects with alveolar air through the alveoli, thus enabling its measurement and detection in breath. In fact, breath acetone analysis can prove to be more effective than urine sampling for monitoring ketosis in diabetic patients with elevated ketone levels (Gunawan et al., 2012).

Gas chromatography coupled with mass spectrometry has been instrumental in assessing acetone concentrations, revealing that breath from diabetic individuals contains higher levels of acetone compared to normal breath. For instance, while the acetone concentration in the breath of 15 control adults ranged from 0.2 to 0.8 ppm, the breath of 15 diabetic adult patients showed a validated concentration of up to 1.8 ppm (Deng et al., 2004).

An investigation by Galassetti et al. (2005) demonstrated a strong correlation between breath ethanol and acetone measurements, both of which are linked to glucose metabolism and variations in serum glucose levels. Furthermore, a declining trend in exhaled acetone levels below baseline values corresponded with postprandial hyperglycemia, a state where blood glucose levels rise after meals. This decline in acetone levels after 120 minutes was approximately 30% lower than baseline. The oral glucose tolerance test (OGTT), a measure

of glucose responsiveness, exhibited a pattern analogous to blood beta-hydroxybutyrate levels and resonated with acetone but displayed greater stability.

In the realm of sensor technology, Narjinary et al. (2017) successfully engineered SnO_2-MWCNT nanocomposites through a straightforward chemical approach. Validation through XRD and TEM analyses confirmed the nanocomposites' phase purity and nanocrystalline structure. Remarkably, this sensor outperformed pure SnO_2 at lower temperatures and demonstrated the capacity to detect acetone at sub-ppm levels with precision and minimal moisture interference. These attributes are essential for developing non-invasive breath analysis tools for diabetes monitoring.

Furthermore, the feasibility of room temperature operation is a pivotal consideration for the development of wireless or portable acetone gas sensors. Composite metal oxide nanostructures offer a promising avenue for achieving this objective (Nazemi et al., 2019). In fact, according to the findings of Yu et al. (2021), a sensor based on pod-like SnO_2 hierarchical micro-nano structures exhibited a superior response to acetone among six target gases and displayed enhanced selectivity towards acetone. This may be attributed to an intensified surface redox reaction between acetone and adsorbed oxygen. In light of these advancements, the medical community stands to gain significantly from the establishment of a robust, accessible, cost-effective, and non-invasive tool for diabetes management. Table 2.3 shows examples of acetone sensors in literature and their morphologies and synthesis processes.

Table 2.3 Examples of acetone sensors in literature and their nanostructures' synthesis processes and characteristics.

Gas sensor materials	Processing route	Synthesis process	Synthesis temperature (°C)	Morphology	Diameter of nanostructure	Length of nanostructure	Reference
SnO$_2$	Hybrid	Vapor-solid	80	Nano-belt	330 nm	20 μm	(Fields et al., 2006)
NiO	Wet process	Hydrothermal	120	Hollow microspheres	~ 25 nm	-	(G.Zhu, C.Xi, et al., 2012)
SnO$_2$	Hybrid	Vapor-liquid-solid	300	Nano-wire	-	10-80 μm	(Jung, Choi & Kim., 2012)
VO$_2$	Wet process	Hydrothermal	240	Nano-rods	-	< 1 μm	(Simo et al., 2017)
ZnO-NiO hierarchical composite	Wet process	Hydrothermal	120	Nano-flower	5 μm	1–3 μm	(Y.Lu et al., 2017)
Cr-doped ZnO	Wet process	Hydrothermal	120	Nano-rods	-	-	(Zhu, Li & Zeng., 2017)
Ce-doped In$_2$O$_3$	Wet process	Hydrothermal	160	Nano-spheres	170 nm	-	(Liu et al., 2018)
Pd-doped ZnO	Hybrid	Electrospinning & Magnet sputtering	50	Nano-fiber	~ 200 nm	-	(Hu et al., 2020)
SnO$_2$-CuO	Wet process	Electrospinning	600	Nano-tubes	150 nm	-	(Park et al., 2020)
Ag-ZnO	Wet process	Hydrothermal	-	Nano-wire	500 nm	-	(Zhang et al., 2021)

2.6.2 Recent Developments in Acetone Detection

In recent times, significant strides have been made in the realm of acetone gas sensing, leading to innovative breakthroughs that enhance our ability to detect and analyze this compound. These advancements not only promise heightened sensitivity and accuracy but also offer the potential to revolutionize various fields where acetone detection plays a crucial role. Table 2.4 illustrates recent advancements in gas sensors specifically designed for detecting acetone.

Table 2.4 Recent acetone gas sensors in literature for varied SMOs and their performance.

Gas sensor materials	n-type/ p-type	Acetone detection range (ppm)	Operating temperature (°C)	Response (R_a/R_g) or (R_g/R_a)	Response time (s)/ Recovery time (s)	Synthesis process	Reference
TiO₂ nanotubes	n-type	100	RT	70.18 [1]	19 / 14	Electrochemical (RT., 2 h)	(Bhowmik, B., Hazra, A., et al., 2014)
V₂O₄ nanoneedles	n-type	1.7	RT	1.025	73 / NA	Vapor deposition	(Hakim, S. A., Liu, Y., et al., 2015)
SnO₂ nanoporous	n-type	100	RT	14.64	30 / 20	Hydrothermal (120 ℃, 12h)	(Shao, S., Wu, H., et al., 2015)
SnO₂ nanofibers	n-type	1 - 300	275	4.1 - 150.7	NA	Electrospinning (600 ℃, 2 h)	(Tang, W., Wang, J., et al., 2015)
ZnO flower-like hierarchical nanostructure	n-type	50 - 300	300	5 - 70	7 / NA	Hydrothermal (200 ℃, 3 h)	(Peng, C., Guo, J., et al., 2016)
PdO-Co₃O₄ hollow nanocages	p-type	0.4-5	350	1.16 - 2.51	NA	Precipitation reaction (RT, 5hrs) +Calcination (600 ℃, 1h)	(Koo, W., Yu, S., et al., 2017)

Table 2.4 continued.

Gas sensor materials	n-type/ p-type	Acetone detection range (ppm)	Operating temperature (°C)	Response (R_a/R_g) or (R_g/R_a)	Response time (s)/ Recovery time (s)	Synthesis process	Reference
SnO_2/Au-In_2O_3 core-shell Nanoflowers	n-type	100	280	21	2 / 9	Electrospinning	(Li, F., Zhang, T., et al., 2017)
ZnO porous nanosheets	n-type	5-1000	300	10 - 205	26 / 27	Precipitation method	(Li, S., Zhang, L., et al., 2017)
NiO/ZnO Hollow Spheres	n-type	100	275	29.8	1 / 20	Solvothermal	(Liu, C., Zhao, L., et al., 2017)
Fe_2O_3/CuO mesoporous skeleton	n-type	100	300	50	5 / 5	Sol-gel	(Zhang, L., Dong, B., et al., 2017)
Co_3O_4 nanocubes	p-type	10 - 1000	240	1.34 - 5.41	2 / 5	Hydrothermal (180 °C, 5h)	(Zhou et al., 2017)
NiO/SnO_2 hierarchical structures	n-type	50	300	20.18	2 / 9	Hydrothermal (180 °C, 12h)	(Hu, J., Yang, J., et al., 2018)
Sm_2O_3/SnO_2 hierarchical structures	p-type	100	200	41.1	NA	Hydrothermal (120 °C, 8 h)	(Zhang, Y. et al., 2018)

34

Table 2.4 continued.

Gas sensor materials	n-type/ p-type	Acetone detection range (ppm)	Operating temperature (°C)	Response (R_a/R_g) or (R_g/R_a)	Response time (s)/ Recovery time (s)	Synthesis process	Reference
ZnO/SnO$_2$ nanosheets	n-type	0.5 - 10	110	30-54.4% [2]	54.9 / 19.1	Hydrothermal (90 °C, 17h)	(Asal & Nasirian., 2019)
N-incorporated SnO$_2$	n-type	100	300	357 [3]	1.19 min / 1.52 min	Solvothermal (180 °C, 24h)	(Guan, X., Wang, Y., et al., 2019)
PdAu-decorated SnO$_2$ nanosheet	n-type	2	250	6.5	4 / 6	Hydrothermal (180 °C, 12 h)	(Li, G., Su, Y., et al., 2019
Al-doped ZnO nanoparticles	n-type	10	450	56	12 / NA	Hydrothermal (300 °C, 1h)	(Yoo, R., Güntner, et al., 2019)
Al-doped ZnO nanoparticles	n-type	10	450	245	3 / NA	Flame spray pyrolysis	
ZnO/MoS$_2$ nanosheets	n-type	2 - 20	100	1.52	56 / 69	Hydrothermal (210 °C, 12h)	(Chang, X., Qiao, et al., 2020)
α-Fe$_2$O$_3$/SnO$_2$ nanosheets	n-type	1	340	13.63	14 / 70	Chemical bath deposition	(Gong, H., Zhao, C., et al., 2020)

Table 2.4 continued.

Gas sensor materials	n-type/ p-type	Acetone detection range (ppm)	Operating temperature (°C)	Response (R_a/R_g) or (R_g/R_a)	Response time (s)/ Recovery time (s)	Synthesis process	Reference
Co_3O_4 loaded SnO_2 nanowires	p-type	50	300	70	20 / 122	Vapor-Liquid-Solid (900 °C) + Sol-gel	(Kim, H et al., 2020)
Pt-doped 3D porous SnO_2 nanosheets and micro flowers	n-type	0.5 - 1000	153	2.1 - 505.7	130 / 140 (at 100 ppm)	Hydrothermal (150 °C, 16h)	(Quan, W., Hu, et al., 2020)
SnO_2/Co_3O_4 nanospheres	n-type	0.5 - 100	220	23.5	12 / 18	Hydrothermal (190 °C, 18h)	(Xu, Y., Zheng, L., et al., 2020)
CuO-doped ZnO nanowires	n-type	1- 10	RT	1.55 - 3.5	450 / 100	Chemical vapor deposition (500 °C, 30 mins)	(Brahma, S., Yeh, Y., et al., 2021)
$SnO_2/ZnSnO_3$ double shelled hollow microspheres	n-type	2 - 300	290	30	5 / 115	Chemical vapor deposition (80 °C, 12h)	(Cheng et al., 2021)
NiO nanostructures	p-type	50 - 500	325	2.3 - 3.4	NA	Microwave irradiation (70 (±5) °C, 5 h)	(Kaowphon, S., et al, 2021)

Table 2.4 continued.

Gas sensor materials		n-type/ p-type	Acetone detection range (ppm)	Operating temperature (°C)	Response (R_a/R_g) or (R_g/R_a)	Response time (s)/ Recovery time (s)	Synthesis process	Reference
Au-loaded Co_3O_4 porous hollow nanocages		p-type	100	190	14.5	319 / 280	Sacrificial template (60 °C, 24 h)	(Li, Z. et al., 2021)
SnO_2 nanorod on spindle-like α-Fe_2O_3		n-type	200	280	16.8	5 / 25	Hydrothermal (220 °C, 3h)	(Liu et al., 2021)
WO_3 nanoplates		n-type	10	300	39.7	3 / 7	Hydrothermal (180 °C, 12h)	(Liu, Zhu et al., 2021)
SnO_2 pod-like micro-nanostructure		n-type	1 - 100	280	2 - 19.1	5 / 34	Hydrothermal (180 °C, 12 h)	(Yu, H., Zhang, Y., et al., 2021)
TiO_2 - different crystal phases	Rutile TiO_2 - nanorod	n-type	100	320	12.3	3 / 421	Hydrothermal (200 °C, 12 h)	(Cao, S., Sui, N., et al., 2022)
	Anatase TiO_2 - nanoparticle	n-type	100	320	4.1	3 / 292	Hydrothermal (200 °C, 12 h)	
	Brookite TiO_2 - nanorod	n-type	100	320	2.3	3 / 183	Hydrothermal (160 °C, 24 h)	

[1] The response is defined as $S = \Delta R/R_g$, [2] The response is defined as $S\% = [R_0-R_g] / R_0 \times 100$, [3] The response is defined as $S = R_0/R_g - 1$

2.7 Summary and Research Gap

Various semiconducting metal oxides have been studied to detect different gas analytes in different environments. One of the gases that attracted researchers recently is acetone because it can be an important biomarker for many diseases, including diabetes, which is estimated to be upsetting 536.6 million people or around 10.5% of the global population in 2021. Furthermore, sadly, the numbers are anticipated to climb up to affect the quality of life of 643 million and 783 million people by 2030 and 2045, respectively. (Sun, H., Saeedi, P., et al., 2022).

From there, the need to develop a robust, convenient, affordable, and non-invasive tool to monitor glucose levels for diabetic patients is a crucial demand for almost $1/10^{th}$ of the global population. Various attempts have been highlighted in Table 2.3 of the recent developments in detecting acetone at different concentrations, from sub-ppm levels up to 1000 ppm at different optimum temperatures ranging from room temperature (RT.) to 450 ℃. However, there are vital aspects for a sensor to perform well for the application of detecting acetone from the exhaled breath, including durability, high sensitivity, selectivity, low response times, recovery times at low temperatures, preferably RT., towards ppm and sub-ppm concentrations of acetone, altogether, which are not all met in the mentioned works. Finally, the goal of this research is to develop a robust, sensitive, and selective gas sensor for acetone that has fast response and recovery times and works at an adequate temperature that could be used in the future to monitor glucose levels and help in the early detection of diabetes by using a facile hydrothermal synthesis method to form a hetero-material of NiO: SnO_2 from their precursors.

CHAPTER 3: METHODOLOGY

3.1   Raw Materials

First, for materials synthesis, tin (II) chloride dihydrate ($SnCl_2.2H_2O$) and nickel (II) chloride hexahydrate ($NiCl_2 \cdot 6H_2O$) were procured from Sigma-Aldrich, bearing product IDs 208035-100G and 223387-500G, respectively. Furthermore, for the formulation of the ink, diethylene glycol dibutyl ether (DGDE), α-terpineol, and ethyl cellulose were obtained from Sigma-Aldrich, identified by product IDs 205621-100ML, 432628-50ML, and 200646-250G, respectively. Next, for gas sensing experiments, Au interdigitated alumina substrates were ordered from Case Western Reserve University, USA, measuring 5 mm x 5 mm, were sourced from Case Western Reserve University in the USA. An Au wire, with a diameter of 0.2 mm and a purity of 99.9%, was acquired from Alfa Aesar, also located in the USA. Concurrently, an Au paste was secured from Heraeus. Furthermore, gas cylinders containing both pure and mixed gases were obtained from Linde Malaysia Sdn Bhd. It's noteworthy that all chemicals and reagents utilized throughout the research adhered to the standards of analytical grade, rendering additional purification processes unnecessary.

3.2   Material Synthesis and Gas Sensor Preparation

3.2.1   Preparation of Pristine SnO$_2$ and Pristine NiO

The synthesis process of SnO$_2$ and NiO employed in this research closely resembled the methodology outlined by Hu, J., et al. (2020). For the preparation of SnO$_2$, 4 mmol of tin (II) chloride dihydrate ($SnCl_2.2H_2O$) (0.903 gm) (Sigma-Aldrich) was mixed with 10 mmol of tri sodium citrate dihydrate (2.941 gm) (Sigma-Aldrich) in a glass beaker. After that, ethanol and distilled water were added to the glass beaker in a 1:1 ratio (15 ml each),

and the liquid was magnetically agitated for 15 minutes. After that, the mixture was transferred to a 100 ml polytetrafluoroethylene (PTFE) hydrothermal autoclave and placed in the furnace for 12 hours at 180 °C. After the autoclave cooled naturally in the furnace, the precipitated powder was recovered using centrifugation at 6000 rpm for 15 minutes. The resulting powder was then rinsed with water and ethanol before being centrifuged at 6000 rpm for five minutes three times.

For the preparation of pristine NiO particles, 3.182 gm $NiCl_2 \cdot 6H_2O$ (Sigma-Aldrich) were added to a glass beaker. Next, ethanol and distilled water were put in the beaker in a 1:1 ratio (15 ml each), and the mixture was magnetically stirred for 15 mins. After that, the NaOH solution was added to the precursor-ethanol-water mixture dropwise until pH=10. After 30 mins of magnetically stirring, the new mixture was transferred to a 100 ml PTFE hydrothermal autoclave and set in the furnace for 12 hours at 180 °C. After the autoclave cools down naturally in the furnace, the precipitated powder was collected by centrifugation at 4000 rpm for 15 mins. Then, the obtained powder was washed with water and ethanol and centrifuged at 4000 rpm for 5 mins several times. Next, the powder was left in the furnace at 90 °C. Next, the powder was put in a quartz boat and placed inside the quartz tube furnace at 500 °C for 4 hours for annealing. Finally, NiO particles were harvested and kept in containers in a dry cabinet for future use.

3.2.2 Preparation of NiO: SnO_2

The synthesis methodology utilized in this investigation closely mirrored the approach outlined by Hu, J., et al. (2020). Four mmol of tin (II) chloride dihydrate ($SnCl_2.2H_2O$) (0.903 gm) (Sigma-Aldrich) was mixed with 10 mmol of tri sodium citrate dihydrate (2.941 gm) in a glass beaker. After that, different molar ratios of $NiCl_2 \cdot 6H_2O$ (Sigma-Aldrich) were added to the glass beaker with respect to $SnCl_2.2H_2O$. The

NiCl$_2$·6H$_2$O to SnCl$_2$.2H$_2$O molar percentages used were (1%, 5%, 10%, 25%). Afterward, ethanol and distilled water were added to the glass beaker in a 1:1 ratio (15 ml each), and the mixture was magnetically stirred for 15 mins. Afterward, the mixture was transferred into a 100 ml PTFE hydrothermal autoclave and set in the furnace for 12 hours at 180 °C. After the autoclave cooled down naturally in the furnace, the precipitated powder was collected by centrifugation at 6000 rpm for 15 mins. Then, three times, the obtained powder was washed with water and ethanol and centrifuged at 6000 rpm for 5 mins. Finally, the obtained white powder was left to dry overnight in the furnace at 90 °C. Subsequently, all powders were put in quartz boats and placed inside the quartz tube furnace at 500 °C for 4 hours in the air for annealing.

Table 3.1 summarizes the samples' codes and the respective molar ratios of NiCl$_2$·6H$_2$O: SnCl$_2$.2H$_2$O used during the synthesis process. The NiCl$_2$·6H$_2$O: SnCl$_2$.2H$_2$O ratio was calculated by dividing the molar% used of NiCl$_2$·6H$_2$O by the molar% of SnCl$_2$.2H$_2$O.

Table 3.1 Synthesized sample codes and their respective NiCl$_2$·6H$_2$O: SnCl$_2$.2H$_2$O molar ratios during the synthesize process.

Sensor/Material Code	NiCl$_2$·6H$_2$O (mmoles)	SnCl$_2$.2H$_2$O (mmoles)	NiCl$_2$·6H$_2$O: SnCl$_2$.2H$_2$O (Molar ratio)	Remarks
K0	0	4	-	Pristine SnO$_2$
K1	0.04	4	1:100	-
K5	0.2	4	5:100	-
K10	0.4	4	10: 100	-
K25	1	4	25:100	-
NiO	13.39	0	-	Pristine NiO

3.2.3   Ink Preparation for Particle Dispersion

An ink formulation was created by combining α-terpineol (Sigma-Aldrich) and diethylene glycol dibutyl ether (Sigma-Aldrich) in a 1:1 ratio under room temperature conditions. Subsequently, 8 wt.% of ethyl cellulose (Sigma-Aldrich) was introduced into the solution. This solution was then subjected to heating at 200 °C for a duration of 2

hours, ensuring the complete dissolution of the ethyl cellulose component. Following this, the ink was infused with varying proportions of NiO: SnO_2 particles (5wt%, 10wt%, and 20wt%). The composite ink was subjected to magnetic stirring for a period of 1 hour to uniformly disperse the particles. Finally, the prepared ink was securely stored within a dry cabinet for future utilization.

3.2.4 Sensor Preparation

About 4 μl of the composite ink was drop-cast on an Au-interdigitated alumina substrate through a micro-pipette. Next, the substrate was put in the furnace for 2 hours at 200 °C. Finally, the sensor was stored in a dry cabinet for future use Figure 3.1. shows an as-purchased and another loaded Au interdigitated alumina substrate with 4 μl of the ink loaded with 20wt% of the pre-synthesized K10 particles.
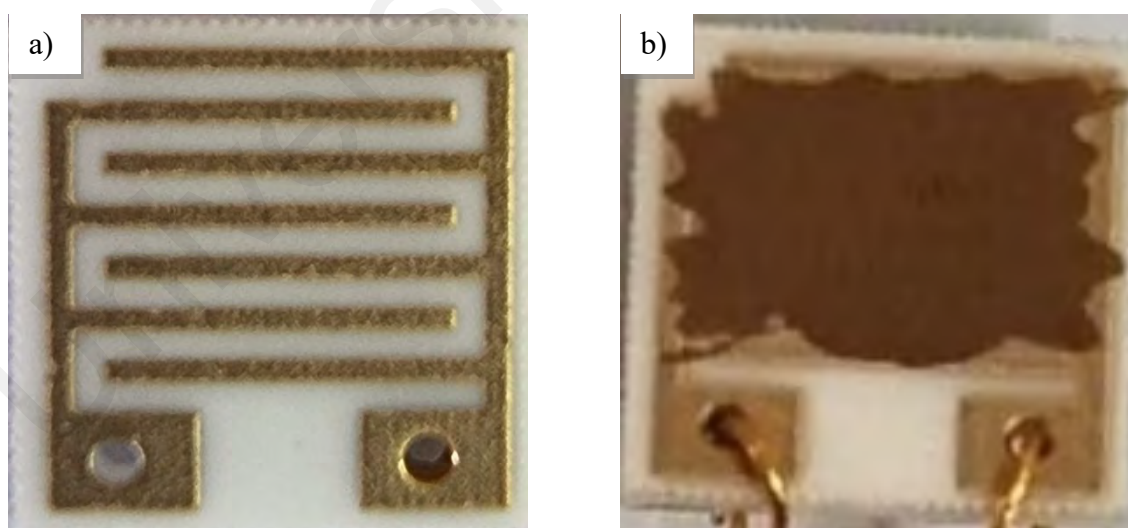
Figure 3.1 A picture of the a) As-purchased, unloaded Au-interdigitated alumina substrate and b) a loaded Au-interdigitated alumina after drop cast with 4 μl of ink loaded with 20wt% of sample K10 then heated at 200 °C at the furnace for 2 hours.

3.3 Characterization of Gas Sensors

3.3.1 Determination of Phase Content and Average Crystallite Size

After synthesis and annealing, the phase content of the heterostructure $NiO: SnO_2$, pristine NiO, and pristine SnO_2 were determined using XRD (PANalytical Xpert PRO MPD Diffractometer). CuK_α radiation with 0.1540598 nm wavelength was used at 40 kV and 40 mA and all samples were scanned at a Bragg angle (2θ) of $20°$ to $80°$.

Moreover, the average crystallite size was calculated using Scherrer's formula:

$$Crystallite\ size = K * \lambda / (\beta * cos(\theta)) \tag{3.1}$$

Where K is a constant (taken at 0.89m), λ is the wavelength of the X-rays used (=1.5406), β is the FWHM of the peak, and θ is the Bragg angle.

3.3.2 Surface Morphologies and Elemental Analysis

The surface morphology of the annealed particles of $NiO: SnO_2$, pristine NiO, and pristine SnO_2 were observed under SEM equipped with energy dispersive X-ray (EDS: EDAX-Genesis and Oxford instruments) spectroscope. Furthermore, the SEM images were analyzed with ImageJ software to determine both the porosity percentages and the average particle size of the samples.

3.4 Gas Sensing

3.4.1 Experimental Setup Design

Figure 3.2 shows a schematic diagram of the gas sensing experimental setup. For the gas sensing experiments, two gas cylinders were used. The first one contained the background gas, and the second contained the target gas, mainly 1000 ppm of acetone in

the nitrogen background; however, other gases that can be present in human breath, including ethanol, carbon dioxide, and ammonia, were also used when testing selectivity. Each cylinder was connected to a different mass flow controller (MFC) controlled by a computer through pressure regulators.

After defining the flow required of each MFC using the computer, the different gases will meet up and mix in the gas mixture before entering the quartz tube inside the horizontal tube furnace (Lindberg Blue M: TF55035COMA1). MFCs controlled the flow from the different cylinders to dilute the target gas concentration when needed.

The sensor, in the middle of the quartz tube, was connected to the data acquisition system (DAQ: Agilent 34972A) using Au wires (Alfa Aesar, 0.2 mm), and to ensure they were fixed, an Au paste (Heraeus) was used at the junctions between the Au wires and the sensor from the backside.

Finally, after the gases were blended in the gas mixture, entered the quartz tube, and encountered the sensor, they were exhausted through a water jar.
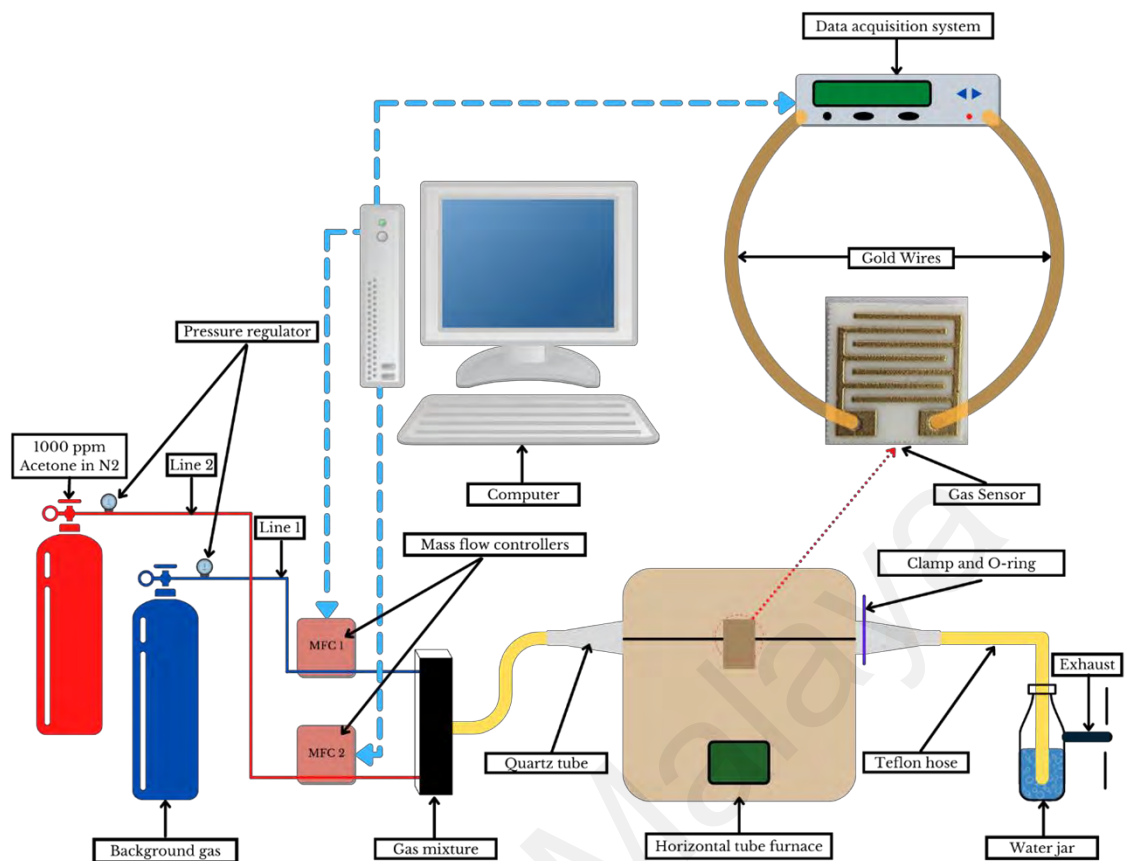
Figure 3.2 A schematic diagram of the gas sensing experimental setup.

3.4.2 Performance Aspects of Gas Sensors

There are different aspects to measuring a gas sensor's performance towards a specific gas analyte. Moreover, the main aspects that determine the functionality and reliability of a gas sensor are sensitivity, selectivity, operating temperature, response time (T_{res}), recovery time (T_{rec}), detection limit (DL), and stability. In the following sections, those aspects will be discussed in detail.

3.4.2.1 Response

For n-type-based materials, the response can be calculated by the following formulas:

In reducing gases (ex, acetone),

$$S = R_o/R_g \tag{3.2}$$

In oxidizing gases (ex, nitrous oxide),

$$S = R_g/R_o \tag{3.3}$$

In addition, for p-type-based materials, the response can be calculated by the following formulas:

In reducing gases,

$$S = R_g/R_o \tag{3.4}$$

In oxidizing gases,

$$S = R_o/R_g \tag{3.5}$$

Where S is the sensor's response, R_o and R_g are the resistances of the sensor in the background gas and when exposed to the target gas, respectively.

Responses were measured throughout this research in multiple environments, including acetone, ethanol, carbon dioxide, and oxygen at different concentration levels and different temperatures.

3.4.2.2 Selectivity

Selectivity is the ability of a gas sensor to detect a specific gas analyte in a mixture of gases. In this research, sensor K5 was tested at equal concentration level and the same operating temperatures against several gases that can be present in the breath of humans, including acetone, ethanol, carbon dioxide, and oxygen.

3.4.2.3 Operating Temperatures

The operating temperature can highly affect the response of a gas sensor. Thus, finding the optimum working temperature is crucial for better performance. This research assessed different gas sensors at 1000 ppm acetone in a nitrogen background at different operating temperatures ranging from 100 °C to 400 °C.

3.4.2.4 Response and Recovery Times

The sensor's response time (T_{res}) is defined as the time required to reach 90% of the resistance after gas exposure. On the other hand, the sensor's recovery time (T_{rec}) is defined as the time required for the resistance to reach 90% of the initial value before exposure to the target gas. This research calculated T_{res} and T_{rec} for different sensors from the response curves at the optimum temperature.

3.4.2.5 Detection Limit

The detection limit is the lowest concentration of the gas that the gas sensor can detect. Due to the limitation of the experimental setup, the lowest concentration tested in this research was 20 ppm of different gases at the optimum temperatures. However, higher concentrations of 1000, 200, 100, and 50 ppm were also tested for different gases at the optimum temperatures.

3.4.2.6 Stability

Stability is most important for a sensor to be reliable and cost-effective. The reproducibility of the sensor characteristics during a specific period of working conditions, including high temperature and the presence of a known analyte. Such

stability is referred to as operational stability. To test the operational stability of the best-performing sensors toward 1000 ppm of acetone gas, up to five cycles of consecutive exposure and withdrawal of the acetone gas were carried out. The response was measured for each cycle to check the alteration in response.

3.4.3 Gas Sensing Experiments

3.4.3.1 Preparation before Experiments

First, after connecting the gas sensor to the data acquisition system (DAQ) using the Au wires and putting the Au paste on the junctions, the gas sensor was placed inside the quartz tube and heated at 200 °C for 1 hour. This step ensured that the ink components had evaporated completely, and the Au paste had melted at the joints and fixed the Au wires. Furthermore, after the tube furnace cooled down to room temperature, the quartz tube was purged by the background gas, Synthetic air, for 10 minutes before starting any experiment. Finally, it is worth mentioning that, while exposed to the background gas, all tested sensors' resistance readings by DAQ at room temperature showed an overload (OVLD) status.

3.4.3.2 Optimum Loading Content of Particles in Ink

A final product powder made from $NiCl_2 \cdot 6H_2O$ to $SnCl_2.2H_2O$ of 10 mole% during the synthesis process was mixed with the prepared ink in different loading percentages of 5, 10, and 20 onto three aluminum substrates.

Next, the performance of the substrates was determined by measuring the resistance of the sample once in background gas, synthetic air, followed by 1000 ppm acetone gas

at 350°C. Finally, the performance results of the three samples gathered by DAQ were used to optimize the loading content of the added particles to the ink.

3.4.3.3 Optimum Temperature Experiment

In order to evaluate the optimum temperature of a particular gas sensor, the quartz tube inside the tube furnace was heated at a steady rate of 10 °C/min in the background environment until it reached a temperature where the resistance's reading changed from the overload status to an actual value. Then, starting from that first temperature where the resistance was detected, the temperature was fixed to capture the response.

The response was calculated at this temperature by recording the resistance changes for 5 minutes in the background gas, then 5 minutes in 1000 ppm of acetone gas in the N_2 background. Next, the temperature was raised by a 25 °C increment, and the last step was repeated at each new temperature.

3.4.3.4 Response, and Recovery Times and Response Experiment

At the optimum temperature, the gas sensor was introduced to a cycle of 5 minutes in the background gas followed by 5 minutes in 1000 ppm acetone in N_2 followed by 5 minutes in the background gas.

For every 5 minutes-stage, the resistances recorded were averaged. The response was measured as mentioned in section 3.3.2.1, and the response and recovery time were measured as mentioned in section 3.3.2.4.

3.4.3.5 Different Concentration Experiment

During this work, some gas sensors were tested towards various acetone concentrations. The concentrations used were 1000, 200, 100, 50, and 20 ppm acetone in N_2. In order to achieve this, background gas had to be mixed with the 1000 ppm acetone in N_2 using the MFCs. Therefore, equations 3.5 and 3.6 have been used to determine the acetone flow rate:

$$F_1 = \frac{F}{C_0} \times X \tag{3.6}$$

Where F_1 is the required flow rate in sccm for the MFC connected to the cylinder containing 1000 ppm acetone in N_2, F is the maximum flow rate in sccm, which is equal to the quartz tube volume, C_0 is the acetone concentration inside the cylinder in ppm, X is the targeted acetone concentration inside the quartz tube.

The flow rate for the MFC connected to the background gas, N_2, referred to as F_2, was calculated as follows:

$$F_2 = F - F_1 \tag{3.7}$$

As an example, to get 20 ppm targeted acetone in N_2 out of 1000 ppm acetone in an N_2 cylinder, with the quartz tube's total flow of 500 sccm, F_1 and F_2 can be determined as follows:

$$F_1 = \frac{500}{1000} \times 20 = 10 \text{ sccm, and } F_2 = 500 - 10 = 490 \text{ sccm.}$$

CHAPTER 4: RESULTS AND DISCUSSION

First, sensors K0, K1, K5, K10, and K25, synthesized with $NiCl_2$: $SnCl_2$ ratios of 0, 1, 5, 10, and 25 moles%, were characterized using XRD, SEM, EDS, elemental mapping, and ImageJ to identify, check and better understand the phases, morphologies, chemical compositions, distribution of chemical elements, and the porosity content of the synthesized materials. Next, to optimize the gas sensors, the responses of different particles-to-ink ratios, ranging from 5 to 20 wt%, were evaluated. Also, the sensitivities of sensors K0, K5, K10, and K25 were assessed at 1000 ppm acetone in a nitrogen background at 350 °C to determine the best-performing sensor among them. Furthermore, the best-performing sensor was picked for further testing. The optimum operating temperature was evaluated by testing the sensor's response at temperatures varying from 100 °C to 400 °C. Moreover, the response and recovery times of the best-performing sensor were assessed at different acetone concentrations in a nitrogen background ranging from 20 ppm to 1000 ppm. In addition, the selectivity of the sensor was tested by calculating and comparing the sensor's responses when exposed to various gases like ethanol, carbon dioxide, and ammonia. Finally, the sensor was tested for stability by recording the responses of five consecutive cycles of exposure to 200 ppm acetone in a nitrogen background. The motivation for this work was to synthesize a gas sensor that is reliable and suitable for acetone detection by evaluating its optimum operating temperature, sensitivity, selectivity, stability, and response and recovery times.

4.1 Characterization of Synthesized Particles

4.1.1 Characterization of the as-synthesized pristine SnO₂

First, Figure 4.1 (a-b) shows the SEM image of the as-synthesized, pristine SnO_2 particles. The SEM images show that the as-synthesized SnO_2 comprised agglomerations of irregularly shaped particles. The average particle size and the porosity percentage were determined by ImageJ software to be 876 nm and 10.2%, respectively. Moreover, Figure 4.2 (a-e) shows the SEM, EDX analysis, and elemental mapping for the same as-synthesized SnO_2 particles. The carbon peak shown in the EDX spectrum is there because a conductive carbon tape was used to stick the particles on the SEM sample holder. The corresponding elements' concentrations are mentioned in Figure 4.2.b.
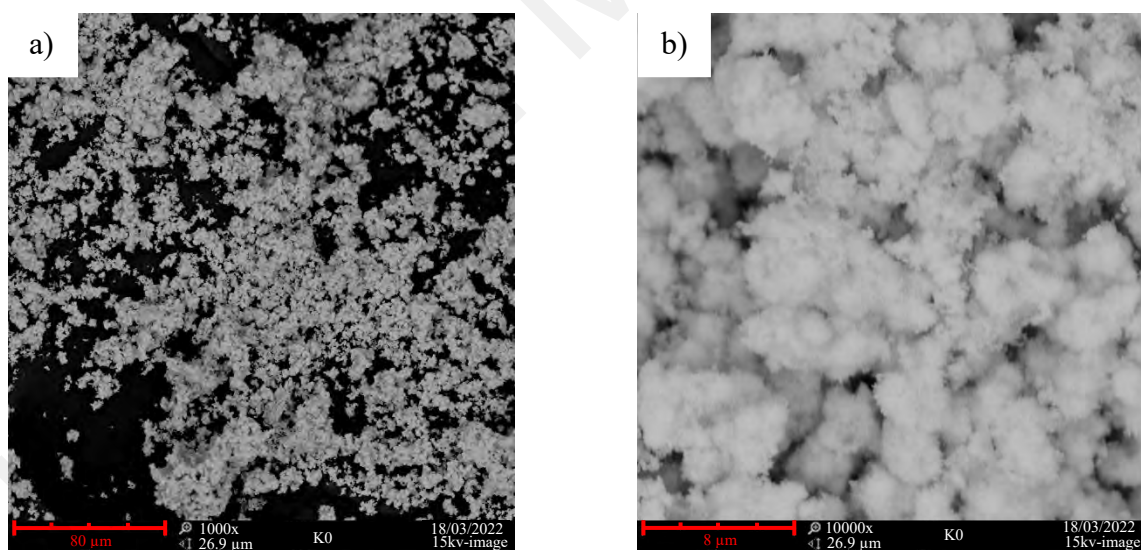
Figure 4.1 SEM images of the as-synthesized SnO₂ at different magnifications, a) 1000X, b) 10000X.

The EDX spectrum (Figure 4.2.b) shows the presence of Sn and O with 70.44 wt.% and 26.90 wt.%, respectively. The presence of carbon in EDX and the elemental mapping results from using a conductive carbon tape to adhere the particles to the SEM sample holder.

52

Element Symbol	Atomic Conc.	Weight Conc.	Stoich. Wt. Conc.
O	67.34	26.90	
Sn	23.77	70.44	96.35
C	8.89	2.67	3.65

Oxygen   **Tin**   **Carbon**
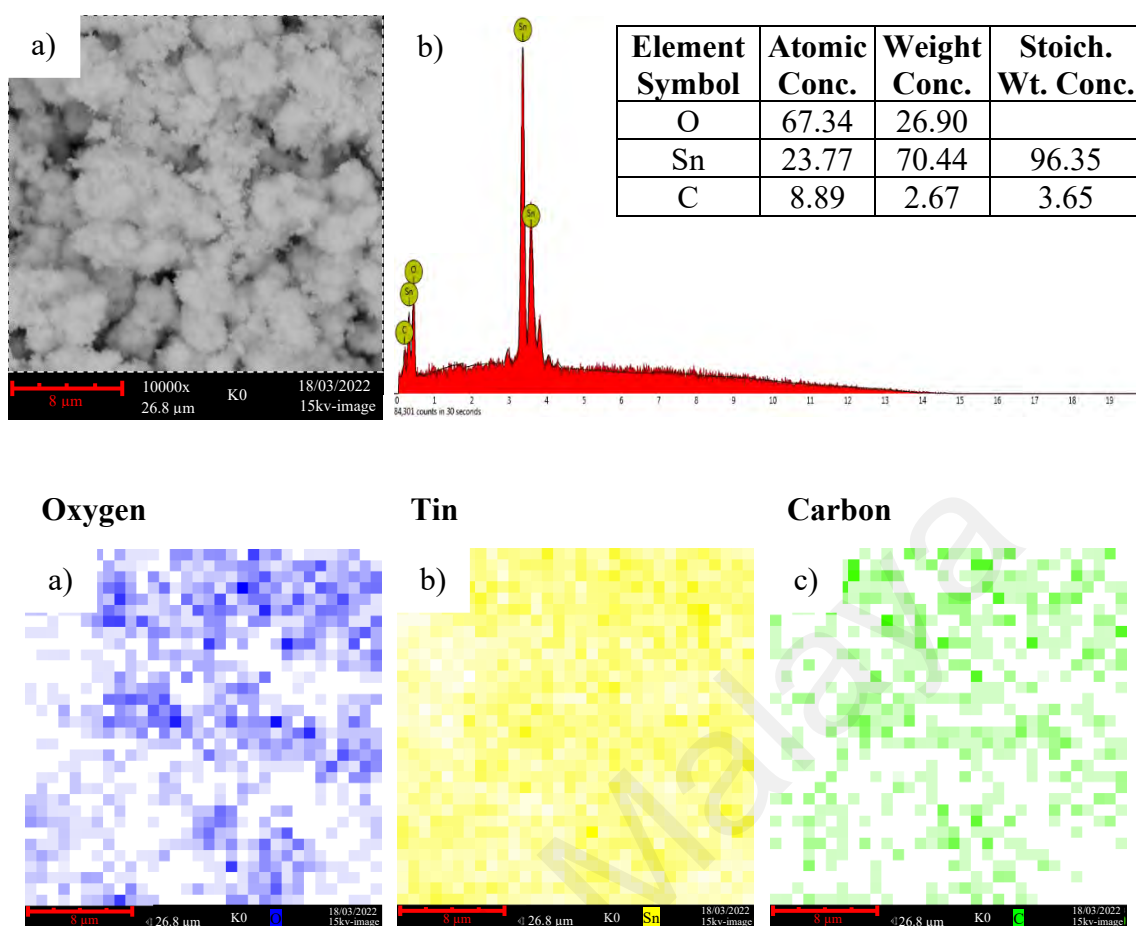
Figure 4.2 The as-synthesized SnO₂ a) SEM image at 10000X, b) EDX spectrum from the spot analysis with elements concentrations, (c-e) Elemental mapping for the elements of O (blue), Sn (yellow), and C (green), respectively.

Moreover, the elemental mapping of the particles (Figure 4.2 (c-d)) shows that the Sn and O elements were well distributed over the surface. Finally, the as-synthesized SnO₂ was characterized by XRD. Figure 4.3 reveals peaks at 2Ɵ= 26.66, 33.66, 37.79, 51.75, 54.73, 61.79, 65.40, 71.23, and 78.66 degrees were correspondent to the crystal planes (1 1 0), (1 0 1), (2 0 0), (2 1 1), (2 2 0), (3 1 0), (1 1 2), (3 0 1), (2 0 2), (3 2 1), respectively, from the SnO₂ tetragonal phase (JCPDS no. 41-1445). Moreover, the average crystallite size was calculated using Scherrer's formula (Equation 3.1) to be 8.25 nm.
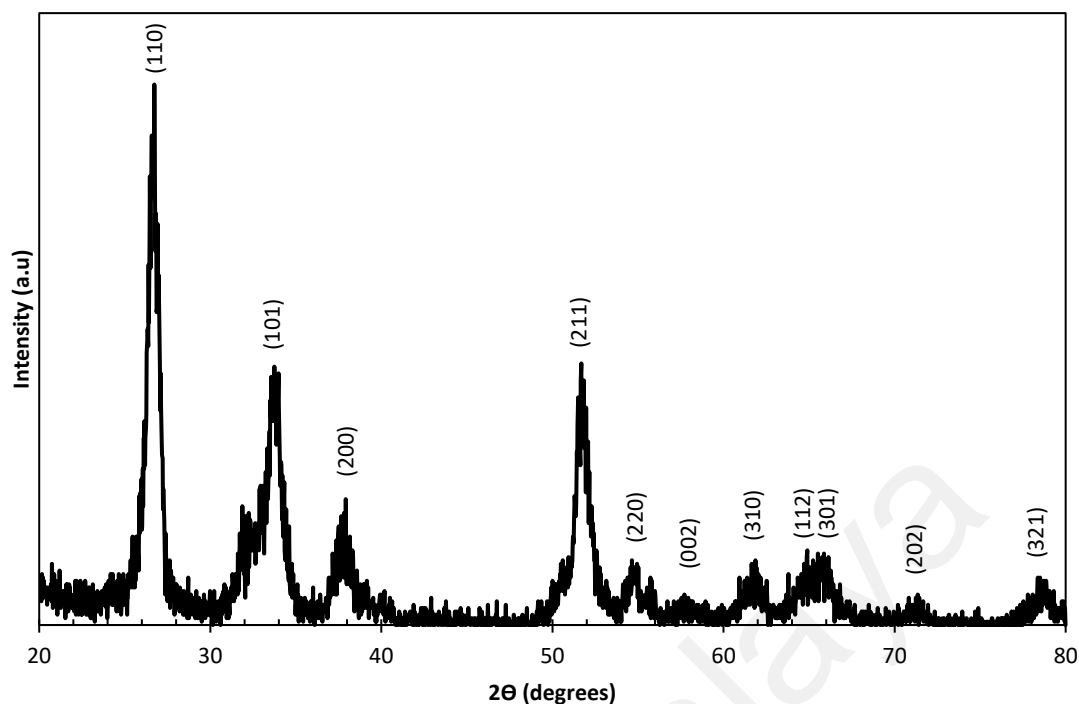
Figure 4.3 XRD Peaks for the as-synthesized SnO$_2$ (JCPDS no. 41-1445).

In summary, SEM images showed that the as-synthesized particles were agglomerated in irregular shapes. The EDX and elemental mapping confirmed the presence of Sn and O elements and that they were well dispersed all over the surface. Moreover, from XRD, the particles were well indexed to the tetragonal SnO$_2$ phase, and the average crystallite size was calculated to be 8.25 nm. Based on that, the hydrothermal synthesis of SnO$_2$ was successful.

4.1.2 Characterization of NiO

The as-synthesized NiO was characterized by XRD. Figure 4.4 reveals peaks at $2\Theta =$ 37.227, 43.253, 62.828, 75.349, 79.339 degrees which are correspondent to the (1 1 1), (2 0 0), (2 2 0), (3 1 1), (2 2 2) planes, respectively, of the Face Center Cubic (FCC) NiO

(JCPDS No. 47-1049). Moreover, using Scherrer's formula (Equation 3.1), the average crystallite size of pristine NiO was 14.51 nm.

Moreover, Figure 4.5 (a-d) shows NiO particles' SEM images. As it is seen, NiO particles tend to form in agglomerates of irregular shapes. The average particle size was determined by ImageJ software to be around 23 µm.
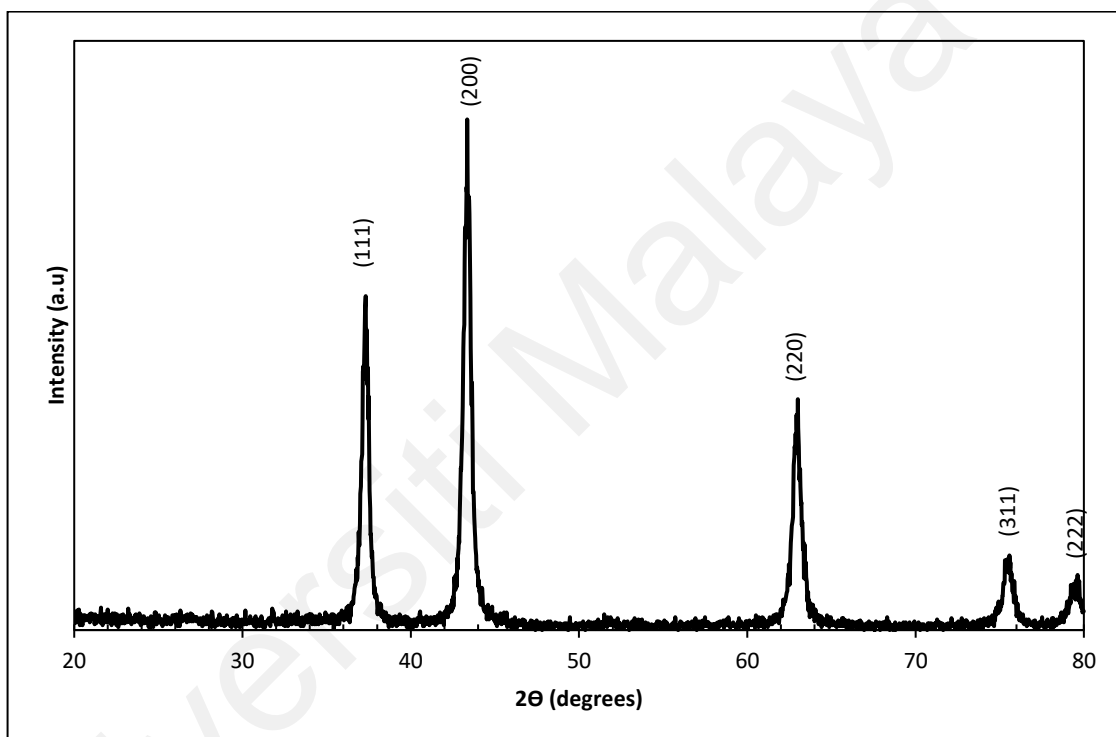
Figure 4.4 XRD peaks for the as-synthesized NiO (JCPDS no. 47-1049).
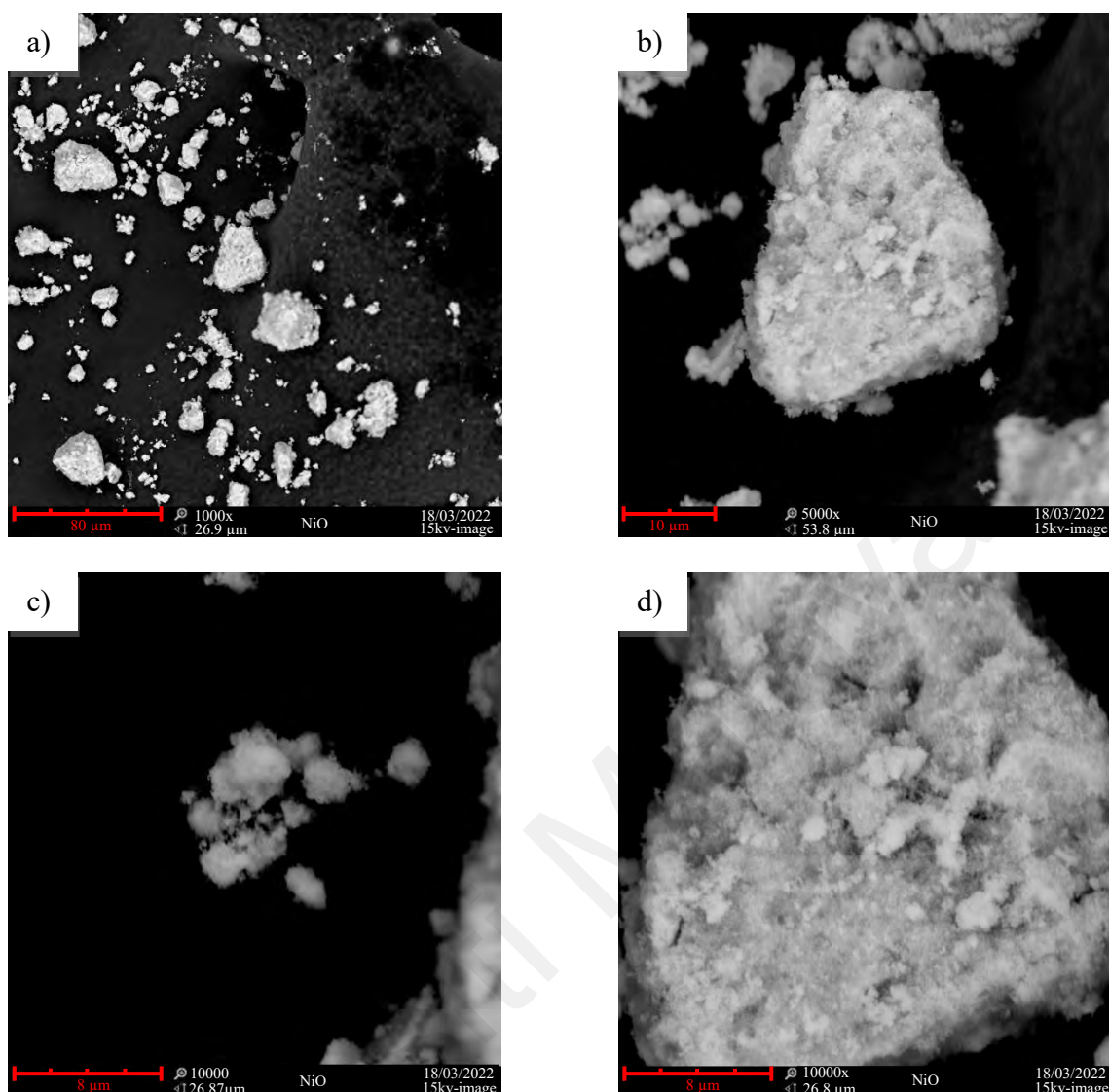
Figure 4.5 SEM images of the as-synthesized NiO at different magnifications, a) 1000X, b) 5000X, c) 10000X, and d) 10000X.

4.1.3   Characterization of NiO: SnO$_2$

As mentioned in section 3.2.1, different molar ratios of NiCl$_2$·6H$_2$O: SnCl$_2$.2H$_2$O were used in the synthesis process. Furthermore, the samples named K0, K1, K5, K10, and K25, had NiCl$_2$·6H$_2$O: SnCl$_2$.2H$_2$O molar ratios of 0%, 1%, 5%, 10%, and 25% respectively.

The XRD peaks observed for K0, K1, K5, K10, and K25, illustrated in Figure 4.6, corresponded to the planes of the SnO$_2$ tetragonal phase (JCPDS no. 41-1445). However,

due to the low nickel content in the samples, NiO intensity peaks were not detected, and additional analysis was performed to determine the presence of nickel in the samples. Furthermore, using Scherrer's formula (Equation 3.1), the average crystallite size was calculated for the samples K0, K1, K5, K10, and K25; the results obtained were 8.25, 10.47, 11.90, 12.51, and 11.41nm, respectively.

Moreover, Figure 4.7 (a-e) and Figure 4.8 (a-e) show SEM images of the K0, K1, K5, K10, and K25 at different magnification levels. In addition, the morphology of the pristine tin oxide sample, K0, is represented in Figure 4.7.a and Figure 4.8.a. As seen, K0 consisted of agglomeration of irregularly shaped small particles. Furthermore, when increasing the $NiCl_2 \cdot 6H_2O$ content during the synthesis process, it is noticeable that the morphology turned to a 3D hierarchical cauliflower-like. For the pristine NiO shown in Figure 4.7.f and Figure 4.8.f, the shape of the particles is irregular, and the particles are coarser in size than the pristine tin oxide sample, K0, and the NiO: SnO_2 hybrid samples (K1, K5, K10, and K25).

Subsequently, using ImageJ software, the average particle sizes of samples K0, K5, K10, and K25 were evaluated to be 0.876 μm,3.7 μm, 4 μm, and 9.44 μm, correspondingly, and the porosity percentages were approximated to be 10.2, 53.4, 43.3, 31.5%, respectively.
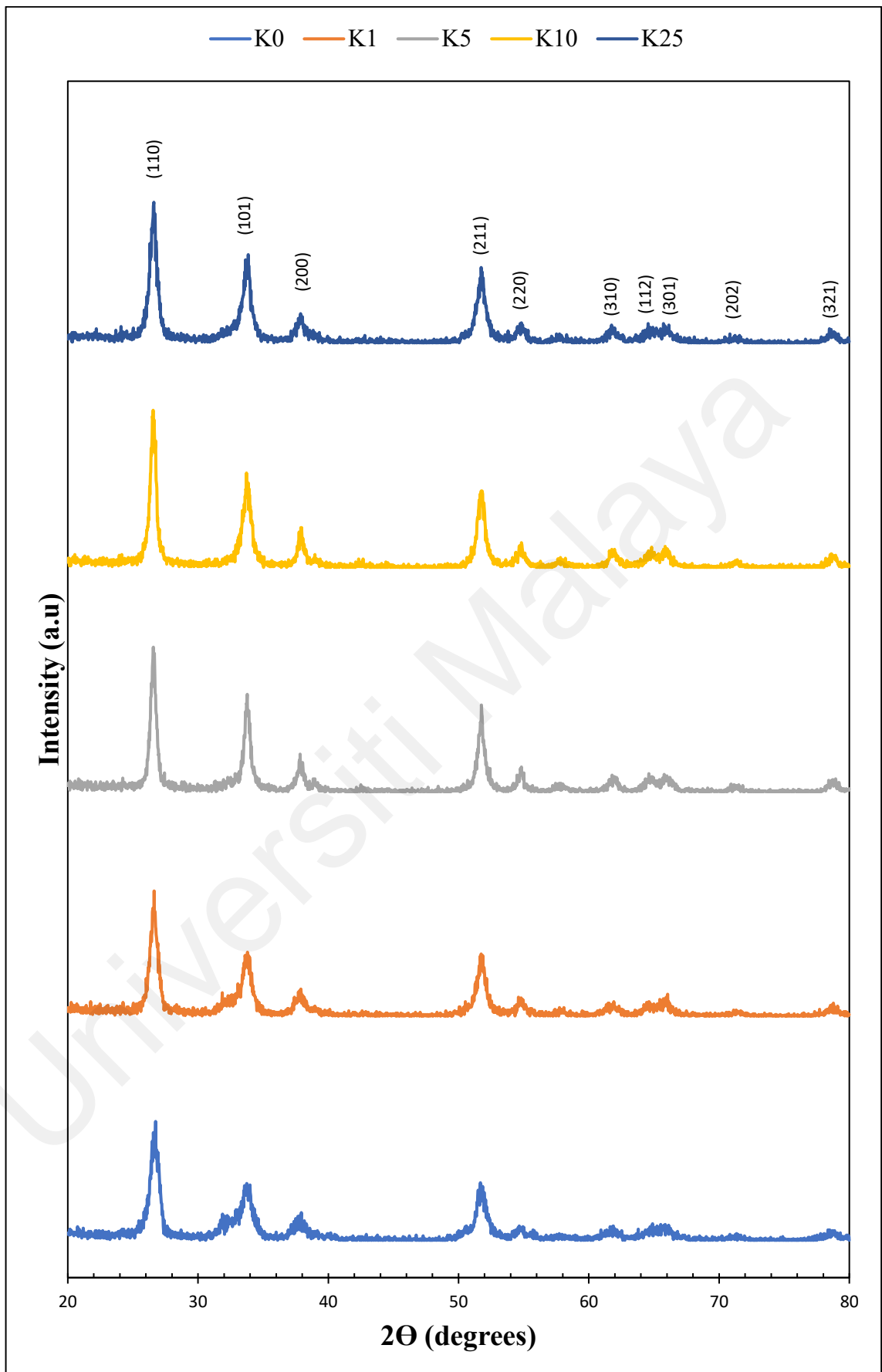
Figure 4.6 XRD pattern of samples K0, K1, K5, K10, K25, and NiO.
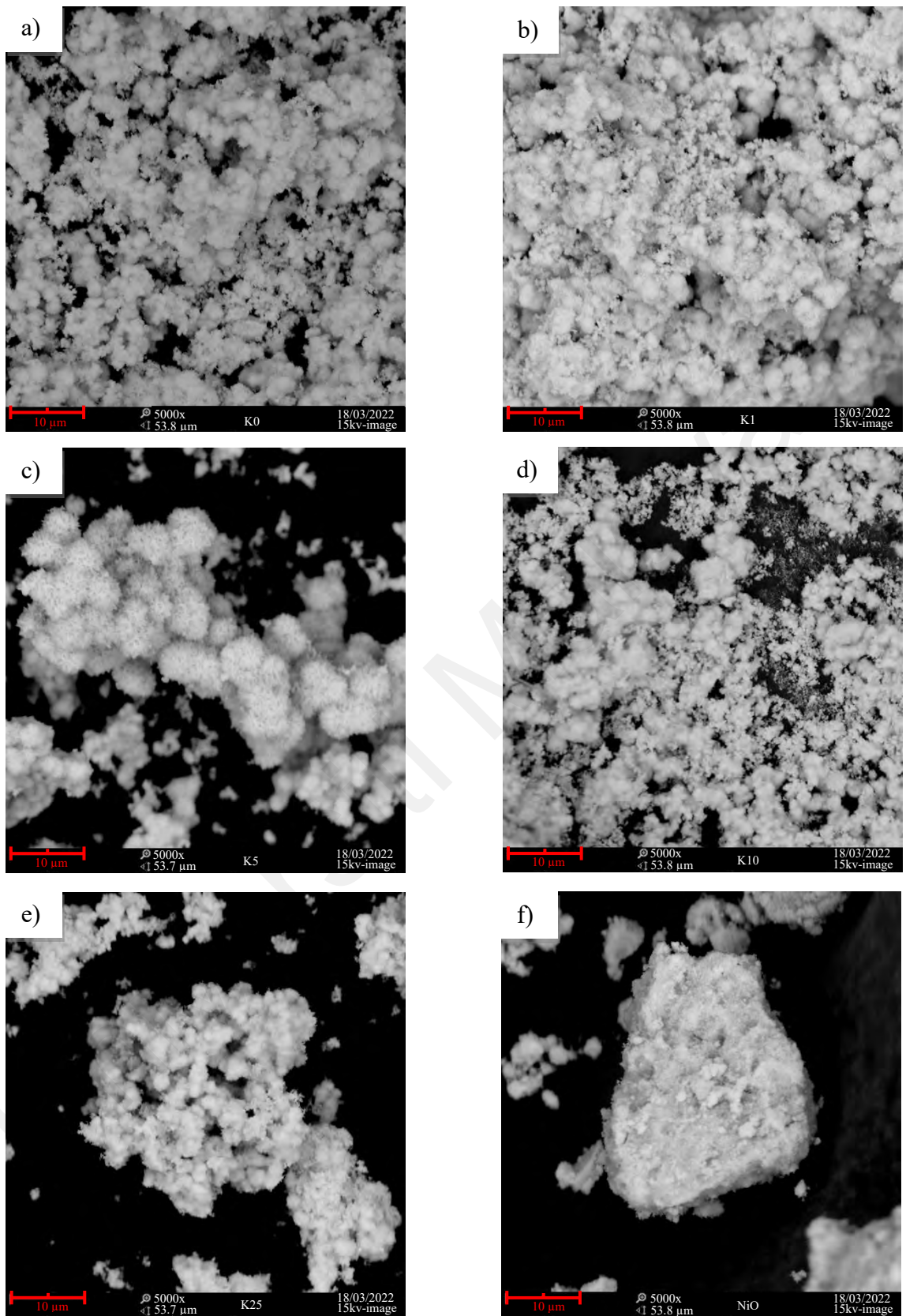
Figure 4.7 SEM images at 5000X magnification of samples a) K0, b) K1, c) K5, d) K10, e) K25, and f) pristine NiO (scale bar: 10μm).
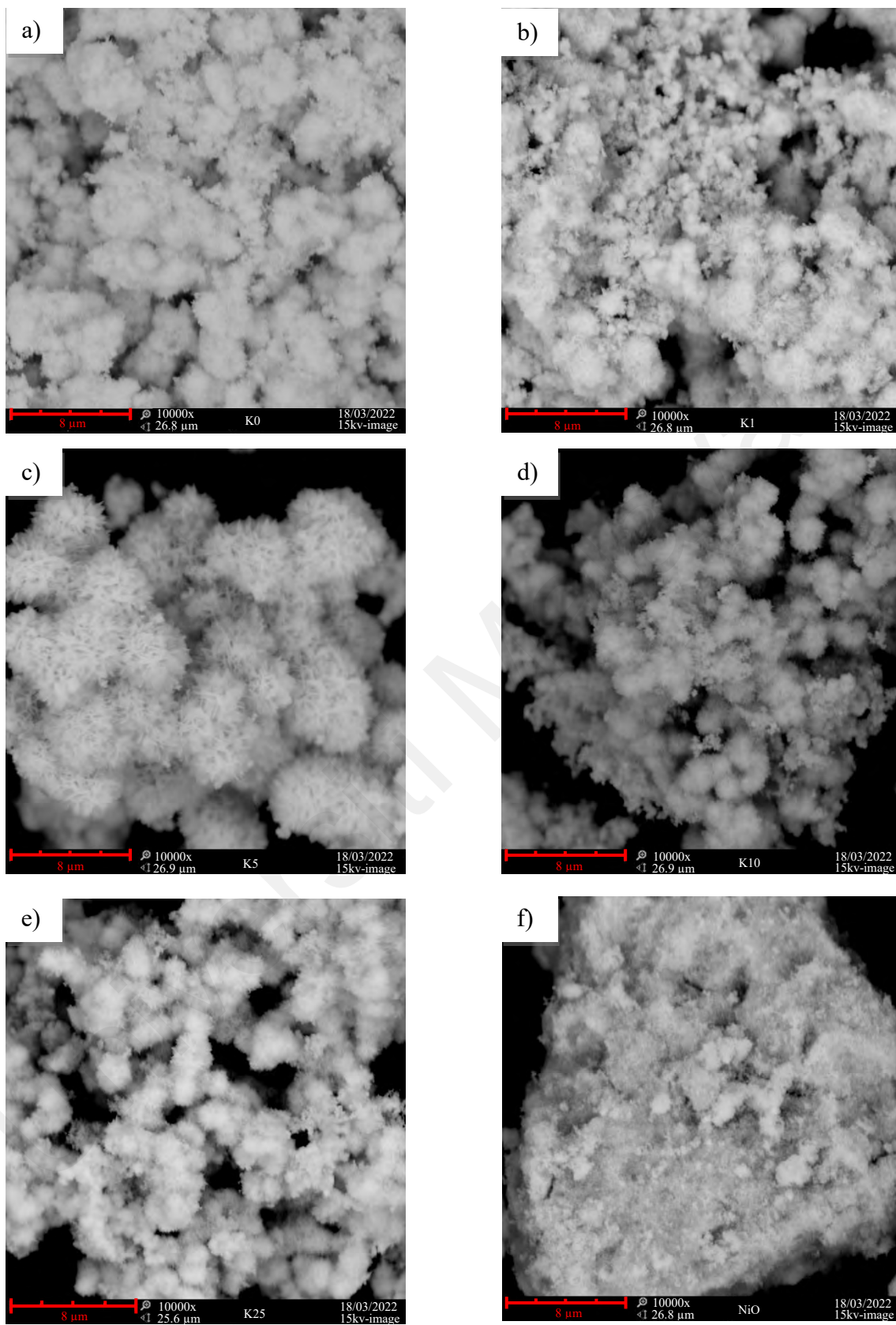
Figure 4.8 SEM images at higher magnifications of samples a) K0, b) K1, c) K5, d) K10, e) K25 and f) pristine NiO (scale bar: 8 µm).

Furthermore, EDX and elemental mapping were conducted to determine the elemental contents and their distribution. The EDX spectrums of samples K5, K10, and K25 and their elemental concentrations are shown in Figure 4.9.

Element Symbol	Atomic Conc.	Weight Conc.	Stoich. Wt. Conc.
O	59.96	32.92	
C	26.11	10.76	16.05
Sn	13.72	55.90	83.34
Ni	0.21	0.41	0.62

Element Symbol	Atomic Conc.	Weight Conc.	Stoich. Wt. Conc.
O	58.87	30.27	
C	24.95	9.63	13.81
Sn	15.33	58.49	83.89
Ni	0.85	1.60	2.30

Element Symbol	Atomic Conc.	Weight Conc.	Stoich. Wt. Conc.
O	42.18	21.98	
C	40.08	15.68	20.09
Sn	14.54	56.23	72.06
Ni	3.20	6.12	7.84
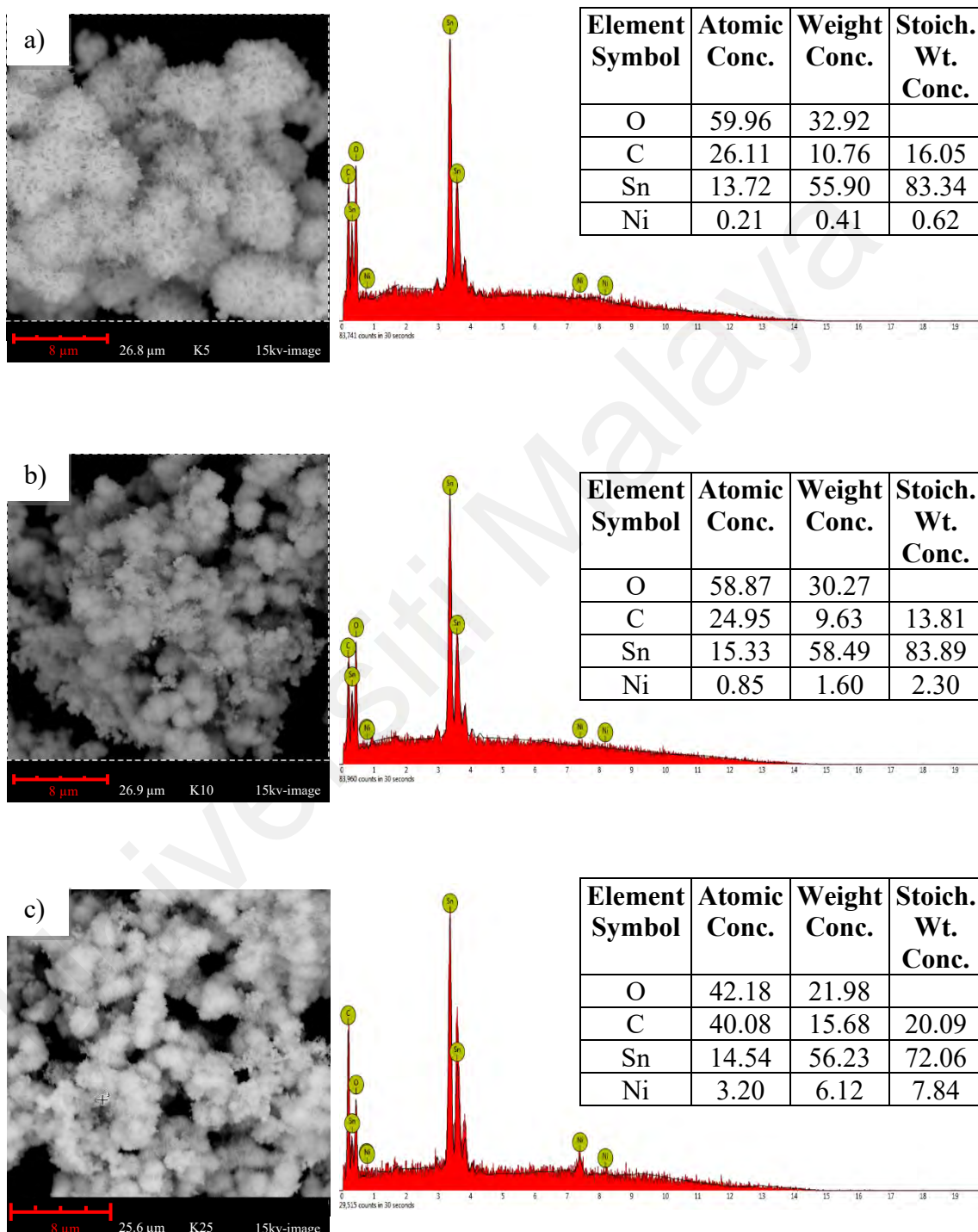
Figure 4.9 The SEM images and their corresponding EDX spectrums from the spot analysis with elements concentrations for the as-synthesized NiO:SnO₂ of samples a) K5, b) K10, and c) K25.
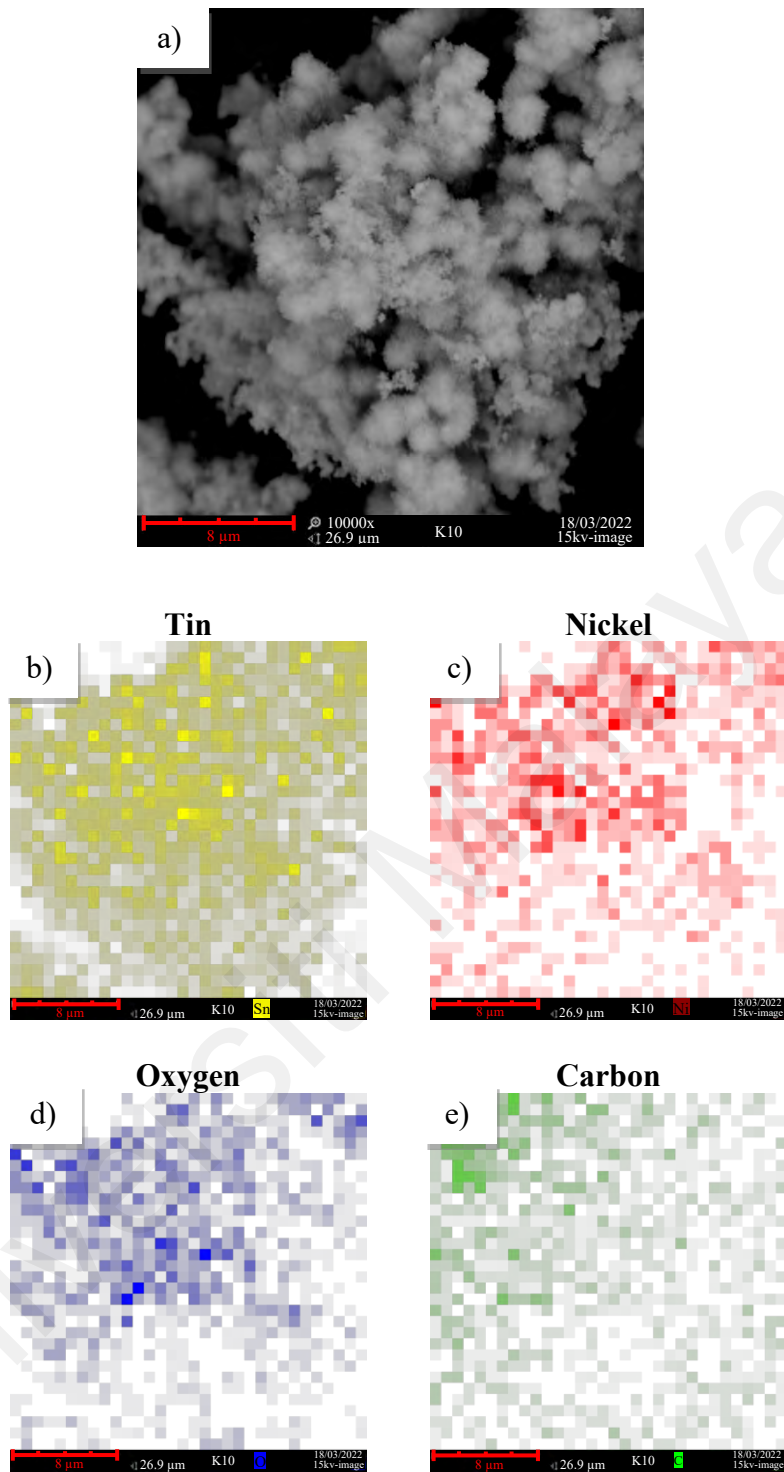
Figure 4.10 SEM image of sample K10 at 10000X, (b-e) Elemental mapping for the elements of Sn (yellow), Ni (red), O (blue), and C (green), respectively.

As seen in Figure 4.9, nickel was present in samples K5, K10, and K25 in atomic concentrations of 0.21, 0.85, and 3.20%, respectively. The presence of carbon in EDX

and the elemental mapping results from using a conductive carbon tape to adhere the particles to the SEM sample holder. After excluding the carbon content, the Ni molar percentages found in samples K1, K5, K10, and K25 were 0.1%, 0.25%, 1%, and 5%, respectively. Furthermore, from the elemental mapping of sample K10 shown in

Figure 4.10, it is seen that tin, nickel, and oxygen were well dispersed all around the cross-sectional area examined. The carbon peak shown in the EDX spectrum is there because a conductive carbon tape was used to stick the particles on the SEM sample holder. However, the presence of carbon in the elemental mapping and the EDX spectrum peaks results from using a conductive carbon tape to adhere the particles to the SEM sample holder. Despite the meticulous application of precursor ratios during the synthesis process, where the $NiCl_2.6H_2O:SnCl_2.2H_2O$ ratios for samples K5, K10, and K25 were 5, 10, and 25 moles%, respectively, the measured nickel atomic percentage via EDX analysis displayed discrepancies. The observed nickel percentages were recorded as 0.25%, 1%, and 5% for samples K5, K10, and K25, respectively.

The discrepancy between the nickel content used during the synthesis, from the precursor $NiCl_26H_2O$, and the observed nickel content in the synthesized samples as determined by EDX can be attributed to losses of nickel species during the hydrothermal synthesis process, which may arise from factors such as evaporation, decomposition, and reaction conditions. These losses can result in a lower actual concentration of nickel in the synthesized samples compared to the precursor ratio used.

In brief, the pristine SnO_2 sample's shape underwent a significant transformation from small, irregular clusters of particles, sample K0 to large, 3D cauliflower-like morphologies, samples K5, K10, and K25. Due to the low concentrations of Ni in samples K5, K10, and K25, XRD analysis was ineffective in detecting NiO peaks. However, subsequent EDX analysis confirmed the presence of small amounts of nickel, 0.25, 1, and

5 moles% in the examined areas of the K5, K10, and K25 powders after excluding the carbon content, respectively, and since elemental mapping revealed a well-dispersed distribution of Sn, Ni, and O elements throughout the cross-sectional areas examined and the XRD peaks recorded in Figure 4.4 were of (FCC) NiO; thus, the formation of NiO: SnO_2 in samples K5, K10, and K25 is concluded.

4.2 Gas Sensing

4.2.1 Optimization of Gas Sensors

4.2.1.1 Ink Loading Percentage

First, an ink was prepared following the method mentioned in section 3.2.3. Then, three sensors were made by loading the ink with 5 wt.%, 10wt%, and 20 wt.% of premade K5's particles.
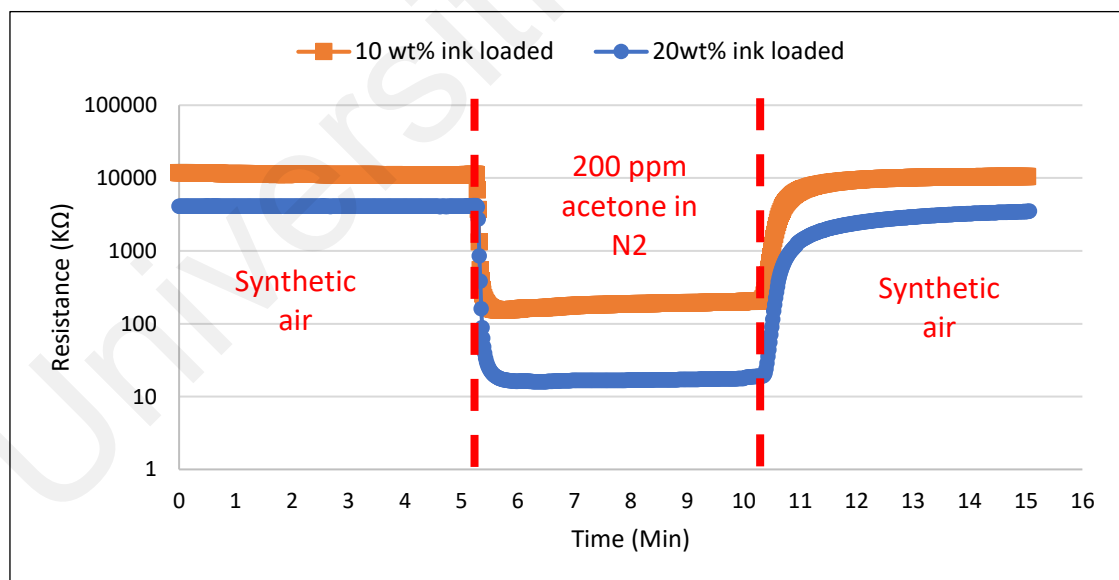
Figure 4.11 Two sensors' responses with the same NiO: SnO_2 composition having Particles: Ink loading ratio 10 wt.%, and 20wt% towards 200 ppm acetone in N_2 background at 350°C.

Furthermore, response tests were conducted at 350 °C for 200 ppm acetone in an N_2 synthetic air background to optimize the ink loading percentage for the 3 sensors.

For the 5wt% Particles: Ink sensor, the data received from (DAQ) showed an Overload (OVLD) value for the entire experiment, meaning the sensor acted as an insulator and not in the semiconducting range.

Moreover, Figure 4.11 presents the response of the 10 wt.% and 20wt% particles: ink sensors. From the graph, the initial resistances of the 20 wt.% and the 10wt% sensors averaged 4082 KΩ and 11226 KΩ, respectively. Furthermore, the responses of the 20 wt.% and the 10wt% particles: Ink sensors were measured to be 240 KΩ and 62 KΩ, respectively. From the response curve shown in Figure 4.11, the decreasing trend in terms of initial resistances of the sensors, from OVLD to 4082 KΩ to 11226 KΩ, and the increase in response values when testing the 5wt%, 10wt%, and 20wt% particles: Ink, respectively. Moreover, Figure 4.12 shows the schematics of the sensors made from inks having different wt.% of loading particles could be explained as follows:
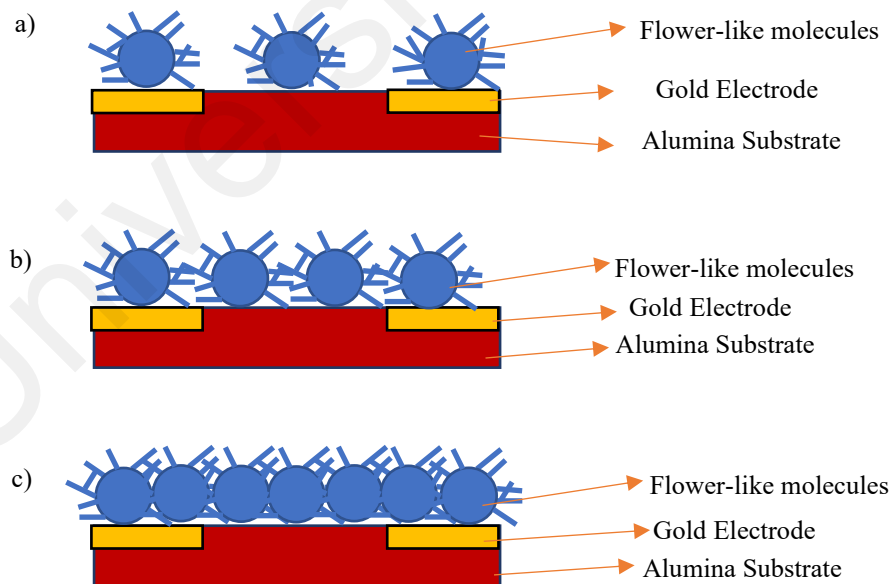
Figure 4.12 Schematic diagrams of sensors prepared from ink having different wt.% of particles a) 5 wt.%, b) 10wt%, and c) 20 wt.%.

a)   For the 5wt% particles in the ink sensor, the low concentration of particles in ink was not enough to fill the gaps between the electrodes; hence, the OVRL value was read for the entire experiment.

b)   For the 10wt% particles in ink sensor, the concentration of the particles was enough to fill the gaps between the gold electrodes; however, the initial resistance was relatively high since the molecules were barely touching each other, so when the material was exposed to synthetic air, the electronegative elements, oxygen and nitrogen, adsorbed onto the surface of the exposed particles capturing free electrons which resulted in a depletion layer across the petals and the core of the cauliflower-like molecules increasing the total resistance of the sensor. On the other hand, when the material was exposed to the reducing gas, acetone, it captured the oxygen molecules, releasing electrons into the material and decreasing resistance. However, due to the inadequate number of molecules or, in other words, the deficiency of conducting channels across the sensor, the resistance did not decrease as much as it is seen in the following case.

For the 20wt% particles in the ink sensor, even though there were more sites for oxygen to be adsorbed onto the material, the sensor's initial resistance was 2.7 times less than the 10wt% sensor because of the close contact of the molecules. Furthermore, when the sensor was exposed to acetone, the resistance dropped drastically because of the abundance of conducting channels, resulting in a response 3.87 times more than the 10% sensor. The 20wt% of particles: ink loading gave the best response. Hence, the same concentration of particles in ink was carried out for upcoming testing.

4.2.1.2   Different Molar Ratios

Different Molar Ratios of NiO: SnO_2 were tested at 350°C towards different concentrations of acetone gas in a nitrogen background. As mentioned in section 3.2.1,

Sample K0, K5, K10, K25 were synthesized using: $NiCl_2 \cdot 6H_2O$: $SnCl_2.2H_2O$ molar ratios of 0%, 5%, 10%, and 25%, respectively. Moreover, as mentioned in the previous section, the 20wt% ink loading was carried out when fabricating the four sensors.

As seen in Figure 4.13, sample K5 (5 mole % $NiCl_2 \cdot 6H_2O$: $SnCl_2.2H_2O$) showed a response of 1734 at 350°C for 1000 ppm acetone in nitrogen background compared to 1373, 869, and 391 for samples K10, K0, K25, respectively under the same conditions.

From the presented data, the response was substantially affected by the NiO content. Furthermore, the NiO content in the sample helped increase the response to some extent. However, when it exceeded a threshold percentage, it was seen to be detrimental to the acetone sensor's performance. Sample K5 was picked for further performance testing.
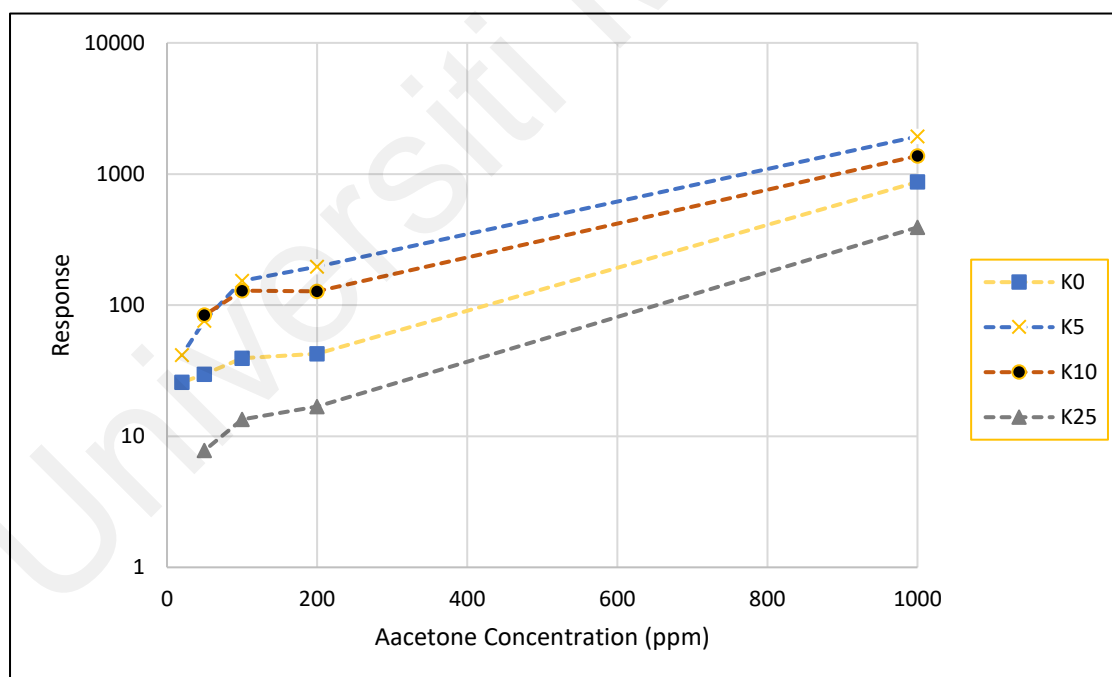
Figure 4.13 Response of sample K0, K5, K10, and K25 towards different acetone concentrations in nitrogen background at 350 °C.

4.2.2 Performance of Acetone Gas Sensors

4.2.2.1 Optimum Temperature

In order to determine the optimum operating temperature, the response of sensor K5, made from using 20wt% ink loading, was measured at different temperatures ranging from 100 to 400°C at 1000 ppm acetone in a nitrogen background.

Moreover, the K5 sensor was exposed to pure nitrogen for 5 mins (Zone A), followed by 5 mins of 1000 ppm acetone in nitrogen background (Zone B), followed by 5 mins of pure nitrogen (Zone C) at different temperatures as shown in Figure 4.14. Furthermore, observations from the latest graph will be discussed in further detail.
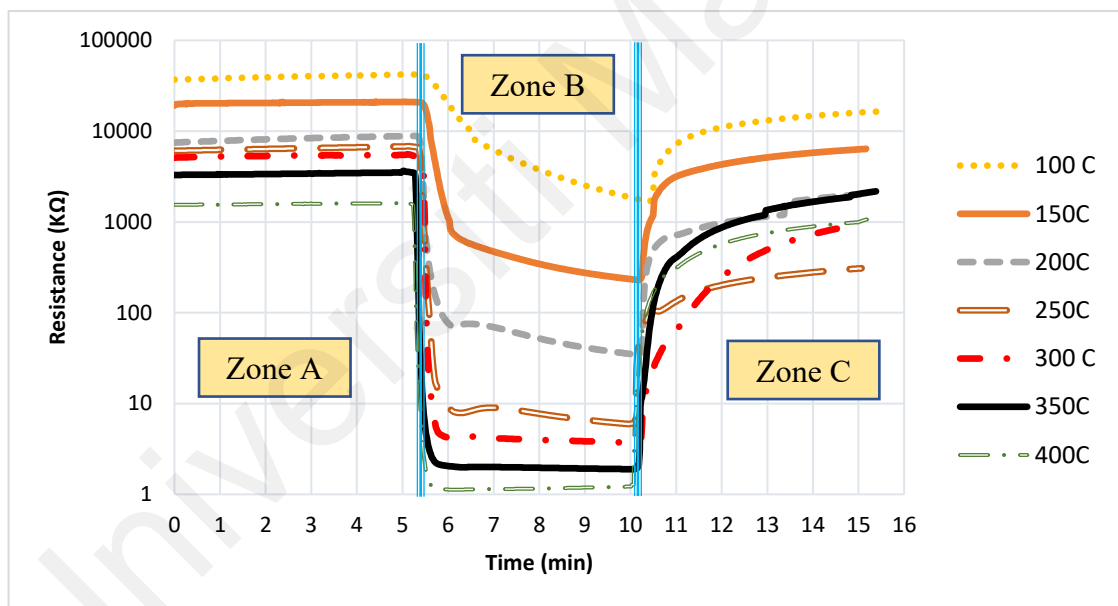
Figure 4.14 The effect of the operating temperature on the K5 sensor toward 1000 ppm of acetone gas in N₂ background.

First, in zone A, the initial average resistance of the K5 sensor decreased when the operating temperature increased. Additionally, Equation 4.1 and Equation 4.2 explain this inversely proportional relationship.

$$R = \rho \; X \; \frac{L}{A} \qquad\qquad\qquad\qquad (4.1)$$

$$\rho = \rho_0 \; X \; (1 + \alpha \; (T - T_0) \qquad\qquad\qquad\qquad (4.2)$$

Where R is the sensor's resistance, ρ is the resistivity, L is the length of the sensor, A is the cross-sectional area, ρ_0 is the resistivity at the reference temperature, T_0 is the reference temperature, T is the operating temperature, and α is the temperature coefficient of resistance (TCR). Unlike most metals, the TCR of semiconductors is a negative value. Hence, that explains the decrease in resistivity when increasing the operating temperature and, subsequently, the decrease in the resistance. Additionally, the average resistances recorded for 100, 150, 200, 250, 300, 350, and 400°C were 39908, 20544, 8254, 6440, 5347, 3396, and 1577 kΩ, respectively.

Second, in zone B, the resistance showed a similar trend, dropping when temperatures increased from 100 to 400°C. However, the resistance for the 100, 150, and 200 curves did not flatten and kept decreasing. Therefore, it is concluded that the sensor is not stable enough below 250°C.

Third, in the recovery area, zone C, it is noticeable that all samples needed more than five minutes to recover from the 1000 ppm acetone in the nitrogen background. More on that will be discussed in further detail in section 4.2.2.2.

Furthermore, the responses were measured at 100, 150, 200, 250, 300, 350, and 400 °C to be 5.09, 7.75, 168, 779, 1323, 1734, and 1271, respectively. Further, the responses of the different temperatures of sample K5 when exposed to 1000 ppm of acetone in a nitrogen background are summarized in Figure 4.15.

In addition, surface interactions are influenced by oxygen content on the sensor surface, which is greatly affected by temperature. Depending on the temperature, the SnO$_2$ surface can have O$_2^-$, O$^-$, or O^{2-} types of oxygen: O$_2^-$ when the temperature is below 180 °C, O$^-$ when the temperature is between 180 and 400 °C, and O^{2-} when the

69

temperature is above 400 C (Walker, J. M., Akbar, S. A., et al., 2019). Moreover, the O^{2-} species is unlikely to appear unless a nearby positive charge causes a significant stabilization. Techniques like electron spin resonance on oxides have been used to detect O^- and O_2^- oxygen species. When a reducing gas, like acetone, is introduced, the O^- signal decreases, implying that O^- is more reactive than O_2^- and is consumed in reactions (Madou, M. J., & Morrison, S. R, 1989). This faster consumption of oxygen analytes will lead to greater alteration in resistance, which will be reflected in the sensor's response.

To summarize, sensor K5 showed a response of 1734 at 350 °C which is 1.36, 1.31, 2.22, 10.32, 216, and 346.8 times higher than 400, 300, 250, 200, 150, and 100°C, respectively, when exposed to 1000 ppm of acetone in a nitrogen background. Therefore, 350 °C was adopted as the optimum temperature and used in the following performance test. While lower operating temperatures are preferred for healthcare applications, there may still be scenarios where a sensor operating at 350°C could be utilized. For instance, in medical research or clinical laboratories, acetone is a biomarker for certain metabolic disorders, such as diabetes and ketoacidosis. A sensor operating at 350 °C could be employed for acetone detection in breath analysis or bodily fluid samples for diagnostic purposes.
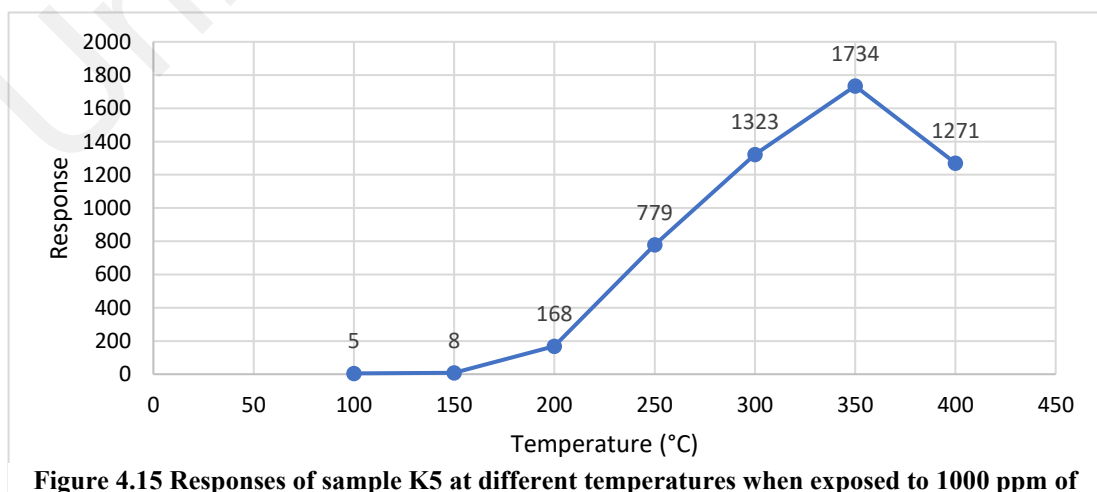
Figure 4.15 Responses of sample K5 at different temperatures when exposed to 1000 ppm of acetone in N₂ background.

4.2.2.2 Response and Recovery Times at Different Acetone Concentrations

The K5 sensor's response time was evaluated when exposed to distinct levels of acetone gas at a temperature of 350°C. As shown in Figure 4.16, it was observed that the sensor's resistance decreased at all acetone concentrations (20-1000 ppm). However, the decrease in resistance was more significant at higher concentrations of the acetone gas.

Moreover, the responses measured for 1000, 200, 100,50, and 20 ppm of acetone were 1734, 325, 170, 70, and 35, respectively, and were plotted in Figure 4.17.

Additionally, the sensor's response and recovery times were shortened when exposed to lower concentrations of acetone. Specifically, response times measured at 1000, 200, 100, 50, and 20 ppm of acetone were 45, 31, 30, 9, and 8 seconds, respectively, and the collected data are summarized in Figure 4.18. Furthermore, the way the K5 sensor behaves in response to different concentrations of acetone can be described as follows: When acetone is present in the surroundings, its molecules will adsorb onto the surface of the sensor, causing oxygen molecules to be captured and electrons to be released, resulting in a dramatic increase in the sensor's conductivity.
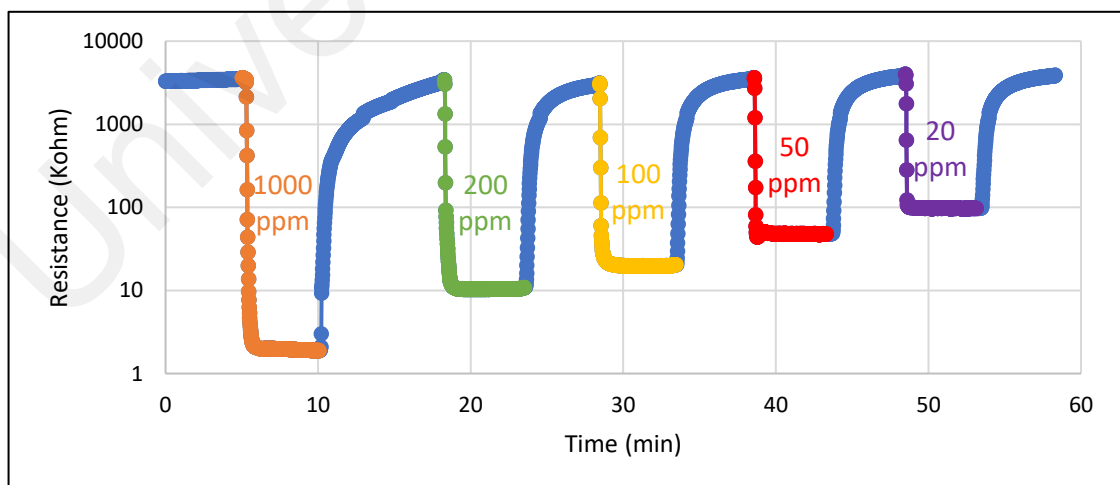
Figure 4.16 Sensor K5 exposed to different concentrations of acetone gas in N_2 background at 350°C.
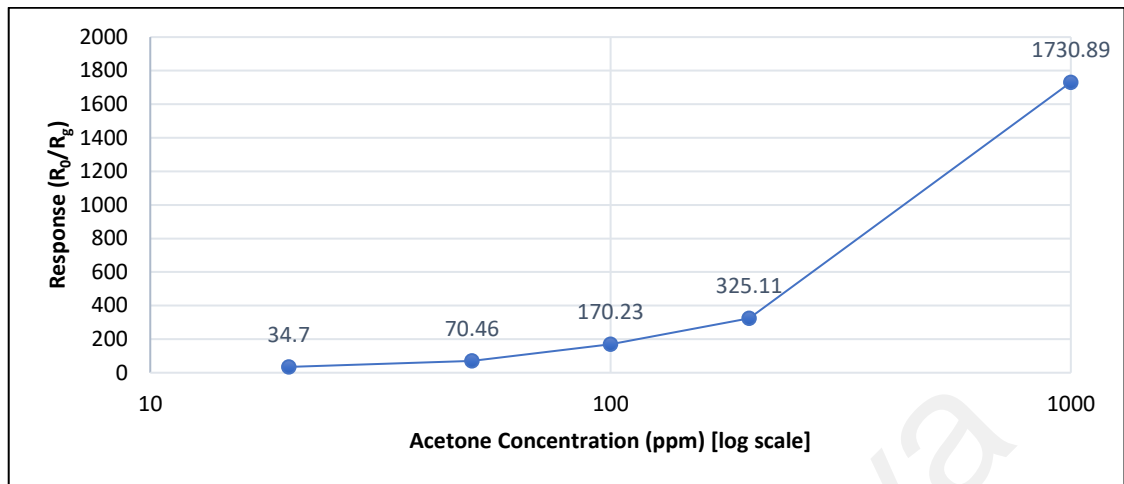
Figure 4.17 Plotted responses of the K5 sensor at various acetone concentrations in N_2 background at 350°C.
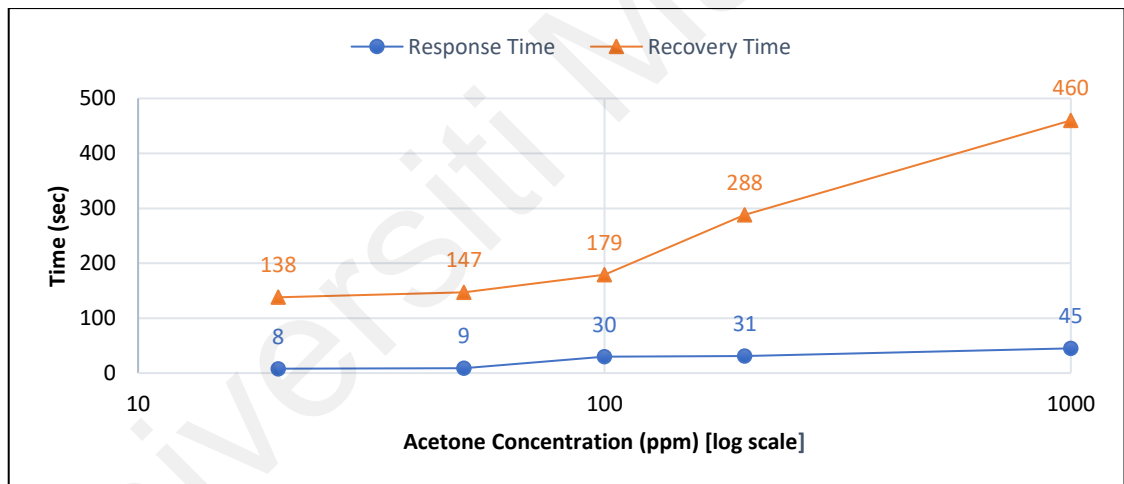
Figure 4.18 Response and recovery times for sensor K5 at various acetone concentrations in N_2 background at 350°C.

In addition, as the acetone concentration increases, more molecules will interact with the sensor, leading to a greater response. In other words, the higher the concentration of acetone surrounding the sensor, the lower the sensor's resistivity will be.

Consequently, since a higher concentration of acetone results in a greater response (R_0/R_g), meaning that the gap between the two resistances is large, the sensor takes more

time to transition from the initial resistance (R_0) to the resistance in the presence of acetone (R_g) and vice versa. Therefore, the response and recovery times recorded were directly proportional to the acetone concentration. Moreover, according to the data presented in Table 4.1, a comprehensive comparison between the present study and prior research endeavors undertaken by fellow researchers regarding response characteristics becomes evident. Notably, in terms of detecting acetone, the synthesized sensor denoted as K5 emerges as an excellent contender. When pitted against other sensors in a direct confrontation, all exposed to an identical concentration of acetone (with the exception of temperature variations for the time being), the prowess of the K5 sensor at 100 ppm is truly remarkable. With a staggering response value of 170, it stands out prominently. Only two sensors from the list manage to eclipse this performance: the Pt-doped 3D porous SnO_2 nanosheets and micro flowers, boasting an impressive 505.7 response (W. Quan et al., 2020) and the W-doped NiO hollow spheres, which exhibited a response of 198.1 (C.Wang et al., 2015). In stark contrast, the remaining sensors on the list exhibited responses ranging between 11 and 50 ppm of acetone. However, when considering operational temperatures, the 350 °C is seen to be on the high end.

To summarize, the K5 sensor's behavior was evaluated when exposed to different levels of acetone gas. The response recorded at 1000 ppm acetone was 49.87 times more than when exposed to 20 ppm acetone. However, at 20 ppm acetone, both response time and recovery time were considerably shorter than when exposed to 1000 ppm. Specifically, the response time recorded at 20 ppm was just 8 seconds, whereas the response time recorded for 1000 ppm was 45 seconds. Similarly, the recovery time recorded at 20 ppm was 2 minutes and 18 seconds, significantly shorter than the recovery time record of 7 minutes and 40 seconds at 1000 ppm. This highlights the trade-off between the sensor's sensitivity and speed of response and recovery when exposed to different acetone concentrations.

Table 4.1 Comparison between different metal oxide acetone gas sensors and the current work.

Gas sensor materials	Acetone detection range (ppm)	Operating temperature (°C)	Response (R_a/R_g) or (R_g/R_a)	Reference
ZnO NRs	100	300	32	(Y.Zeng, T.Zhang, et al., 2009)
Co-doped ZnO NFs	100	360	16	(L.Liu, S.Li, et al., 2011)
Hollow ZnO NFs	100	220	70	(S.Wei, M.Zhou, et al., 2011)
ZnO NPs	100	230	33	(Q.Jia, H.Ji, et al., 2014)
W-doped NiO hollow spheres	100	250	198.1	(C.Wang, J.Liu, et al., 2015)
ZnO flower-like hierarchical nanostructure	50 - 300	300	5 - 70	(C.Peng, J.Guo, et al., 2016)
2D ZnO nanosheet	200	300	110	(P.Wang, D.Wang, et al., 2016)
Porous WO_3 NFs	50	270	55.6	(Wei, S., Zhao, G., et al., 2016)
NiO/ZnO hollow spheres	100	275	29.8	(C.Liu, L.Zhao, et al., 2017)
$SnO_2/Au-In_2O_3$ core-shell Nanoflowers	100	280	14	(F.Li, T.Zhang, et al., 2017)
2D C_3N4- SnO_2 composite	100	380	29	(J.Hu, C.Zou, et al., 2017)

Table 4.1 continued.

Gas sensor materials	Acetone detection range (ppm)	Operating temperature (°C)	Response (R_a/R_g) or (R_g/R_a)	Reference
Fe_2O_3/CuO mesoporous skeleton	100	300	50	(L.Zhang, B.Dong, et al., 2017)
$ZnO-Fe_3O_4$	50	485	47	(L.Zhang, B.Dong, et al., 2017)
ZnO porous nanosheets	5-1000	300	10 - 205	(S.Li, L.Zhang, et al., 2017)
Fe_2O_3 NPs	100	340	9	(S.Liang, J.Li, et al., 2017)
Co_3O_4 nanocubes	1000	240	5.41	(T.Zhou, T.Zhang, et al., 2017)
Co_3O_4 nanosheet array	1000	111	36.5	(Z.Zhang, L.Zhu, et al., 2017)
$PrFeO_3$	200	180	141	(L.Ma, S.Ma, et al., 2018)
$ZnCo_2O_4$ NPs	200	200	38.2	(Y.Xiong et al., 2018)
Sm_2O_3/SnO_2 hierarchical structures	0.1-100	250	1.2-41.1	(Y.Zhang et al., 2018)
$BiFeO_3$ NPs	10	350	12	(Chakraborty, Pal, et al., 2019)
Al-doped ZnO nanoparticles	10	450	245	(R.Yoo., Güntner, et al., 2019)
N-incorporated SnO_2	100	300	357 [*]	(X.Guan, , Y.Wang, et al., 2019)

Table 4.1 continued.

Gas sensor materials	Acetone detection range (ppm)	Operating temperature (°C)	Response (R_a/R_g) or (R_g/R_a)	Reference
NiFe$_2$O$_4$ NPs	100	250	27.4	(Zhang, S., Jiang, W., et al., 2019)
Fe$_2$O$_3$ NPs	100	300	11.6	(D.Han & M.Zhao, 2020)
Co$_3$O$_4$ loaded SnO$_2$ nanowires	0.5-50	300	2.6-70	(H.Kim et al., 2020)
Pt-doped 3D porous SnO$_2$ nanosheets and micro flowers	0.5 - 100	153	2.1 - 505.7	(W.Quan, X.Hu, et al., 2020)
SnO$_2$ pod-like micro-nanostructure	1 - 500	280	2 - 28	(H.Yu, Y.Zhang, et al., 2021)
NiO nanostructures	50 - 500	325	2.3 - 3.4	(S.Kaowphong et al., 2021)
TiO$_2$ nanorod	100	320	12.3	(S.Cao, N.Sui, et al., 2022)
NiO: SnO$_2$ (Sensor K5)	**20**	**350**	**34.7**	**This work**
	100	**350**	**170**	
	200	**350**	**325**	
	1000	**350**	**1734**	

[*] The response is defined as $S = R_0/R_g - 1$

4.2.2.3 Selectivity Test

Sensor K5 was exposed to different gas environments to test its selectivity. As seen in Figure 4.19, K5 was exposed to carbon dioxide (CO_2), ammonia (NH_3), ethanol (C_2H_6O), and acetone ($(CH_3)_2CO$), all at the same concentration of 200 ppm for approximately 5 minutes at 350°C. Furthermore, the responses recorded for carbon dioxide, ammonia, ethanol, and acetone were 2.31, 2.3, 136.22, and 329.84, respectively (Figure 4.20).

To summarize, sensor K5 showed excellent selectivity for acetone detection at the optimum temperature of 350°C. The sensor's response to acetone was 142.74 folds higher than its reaction to carbon dioxide, 143.39 folds higher than its reaction to ammonia, and 2.42 folds higher than its reaction to ethanol.
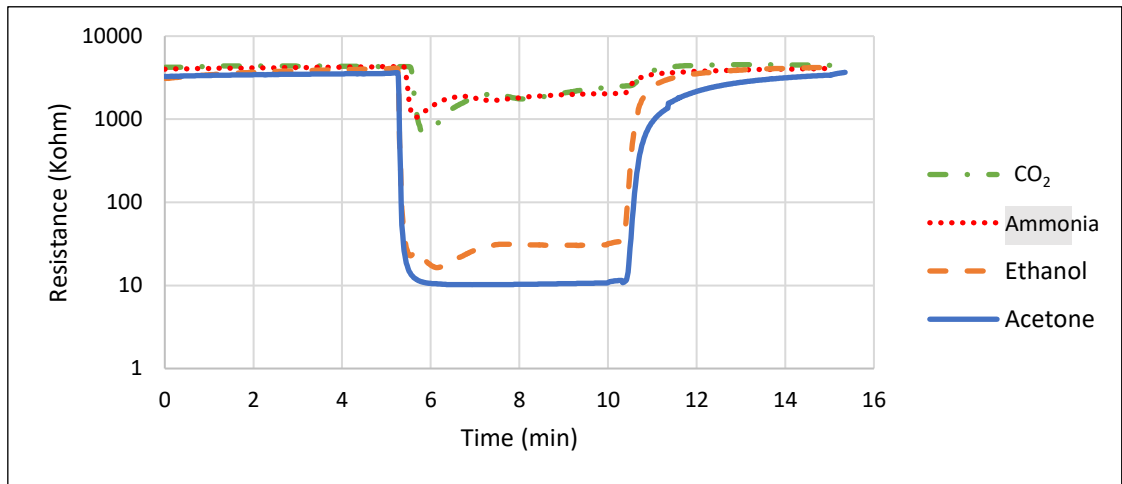
Figure 4.19 Sensor K5 exposed to 200 ppm of carbon dioxide, ammonia, ethanol, and acetone in N₂ background at 350 °C.
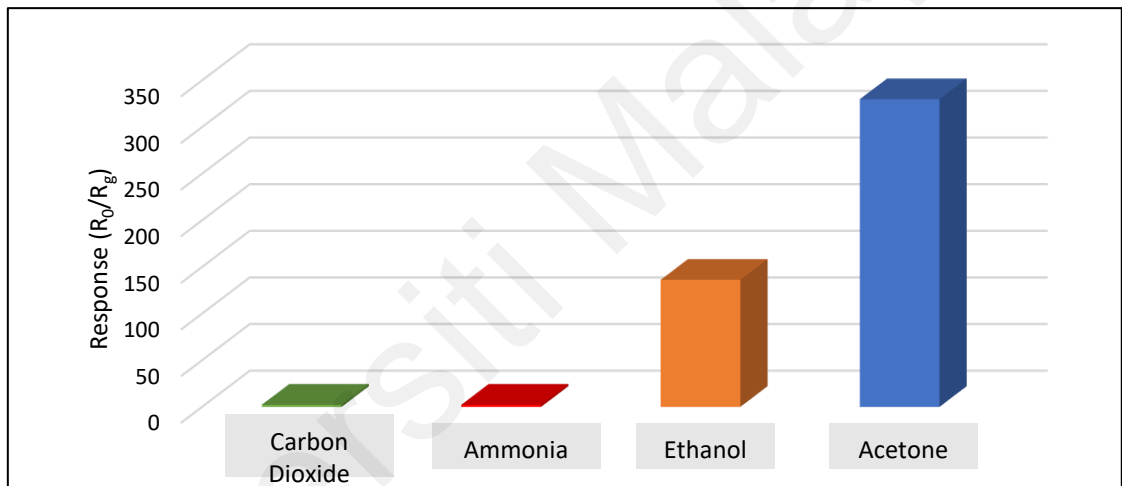
Figure 4.20 K5 Sensor Responses to 200 ppm of carbon dioxide, ammonia, ethanol, and acetone in N₂ background at 350 °C.

4.2.2.4 Repeatability Test

The K5 sensor was evaluated for stability at its optimal temperature of 350°C. Figure 4.21 illustrates the process where the sensor was repeatedly exposed and then not exposed to 200 ppm of acetone in a nitrogen background for a total of five cycles. Moreover, the responses recorded for cycles 1-5 were 329.84, 314.62, 313.25, 317.47, and 309.85, respectively. Also, the response and recovery times were evaluated. The response times recorded ranged between 29 to 38 seconds, with an average of 34.2 seconds, while the

recovery times ranged between 164 to 211 seconds, with an average of 180.2 seconds (Figure 4.22). In summary, the K5 sensor demonstrated consistent performance with a deviation of only 4.61 to 6.01% from the initial cycle's recorded response.
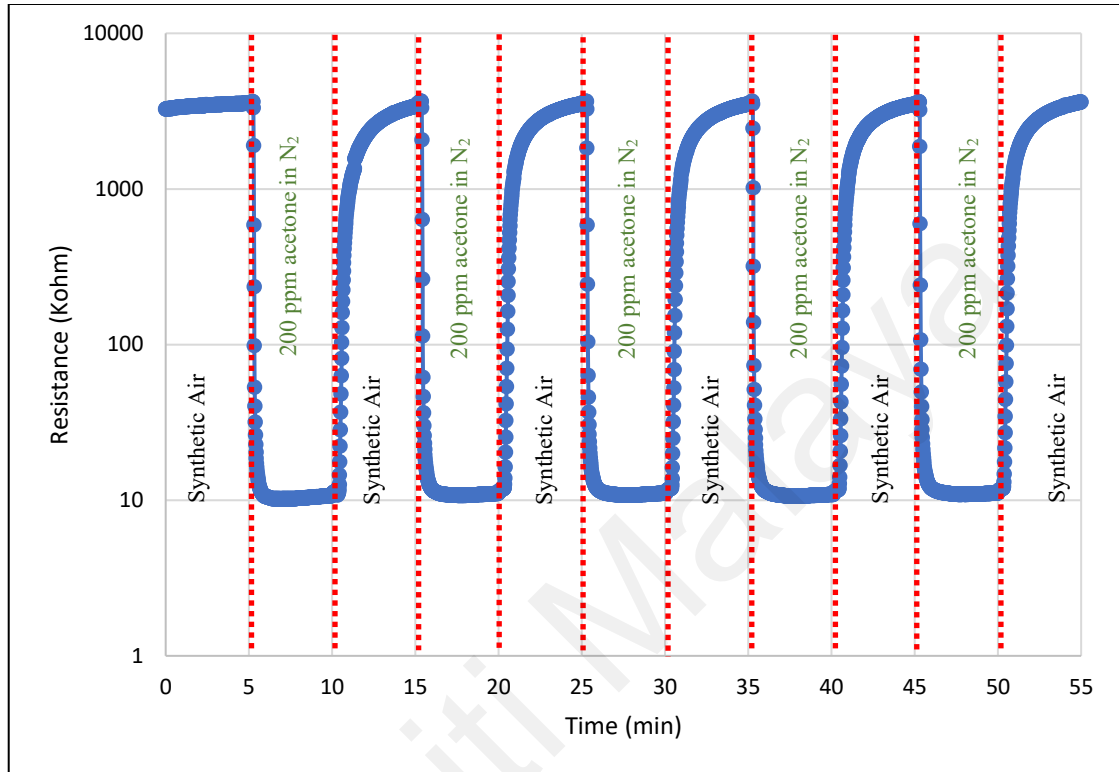
Figure 4.21 Five repeated cycles of exposure followed by the absence of 200 ppm of acetone in N$_2$ background at 350 °C.
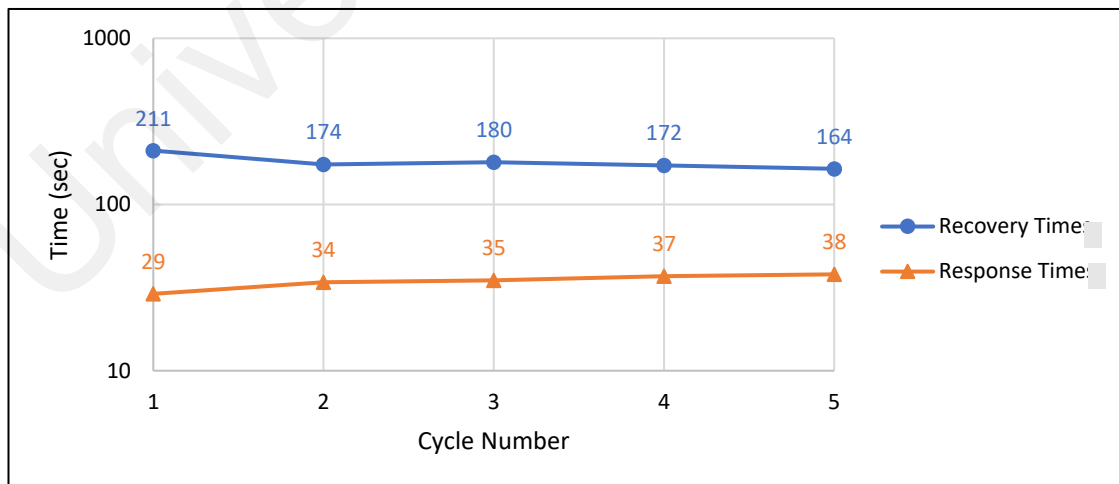
Figure 4.22 The response and recovery times for five cycles of 200 ppm acetone in N$_2$ background at 350 °C.

4.3   Gas Sensing Mechanism

The widely accepted explanation for how the current in the n-type, pristine SnO_2 resistive sensor is modulated is as follows:

The oxygen attaches to the surface and takes electrons, creating a depleted layer in the metal oxide, which increases resistance. Next, when a reducing gas is present, it reacts with the adsorbed oxygen, releasing it from the surface and the electrons back into the metal oxide, which reduces resistance. Theoretically, when a p-type material, like NiO, is combined with SnO_2, electrons will flow from the n-type to the p-type part, and holes will flow from the p-type to the n-type part until equilibrium is reached. Once equilibrium is reached, the n-type resistance, or the backbone, should have increased since it has lost some of its mobility carriers, electrons, in that process.

Moreover, Figure 4.23 shows the response-recovery curves of samples K0 and K5 at different acetone concentrations. When not exposed to acetone, the resistance of the K0 sample (pristine SnO_2) was seen to be greater than sample K5, which should be the opposite if the heterojunction effect is the main contributor to the sensing mechanism. The small amounts of NiO present in the samples are the reason behind the minimal effect of heterojunction on the samples' initial resistances.

Furthermore, when acetone gas is present, it is seen that the K5 sensor's resistance drops significantly more than the pristine SnO_2. Due to this drastic fall in resistance, the primary reason for the enhanced response of the K5 sensor is the adsorption of the analyte gas.
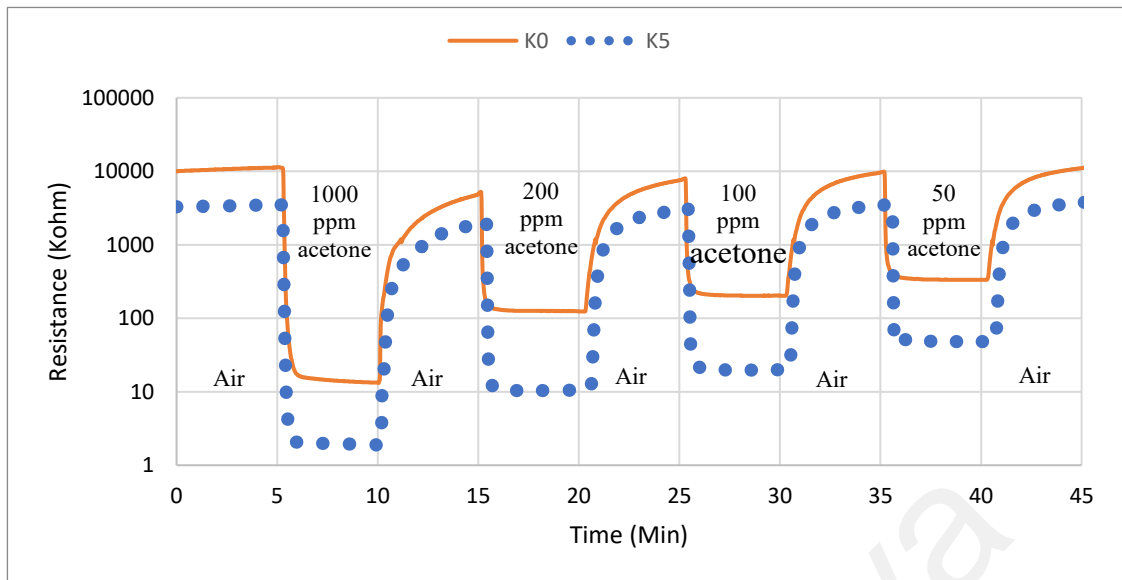
Figure 4.23 Response-recovery curve of samples K0 and K5 at 1000, 200, 100, and 50 ppm of acetone in N_2.

Moreover, the shape and geometry of the cauliflower-like NiO: SnO_2 synthesized particles with a higher surface-to-volume ratio are considered to be the primary reason behind the superior adsorption of the analyte gas compared to the irregular particles of the pristine sample to some extent.

Additionally, the particle sizes of samples K5, K10, and K25 were evaluated to be 3.7 μm, 4 μm, and 9.44 μm, respectively, while the responses recorded at 350 °C for 1000 ppm acetone were 1734, 1373, and 391, respectively. It is clear that there is an inversely proportional relationship between the particle size of the synthesized NiO: SnO_2 samples and the response recorded. Therefore, even though the particle size for K0 was significantly smaller than the other NiO: SnO_2 samples (0.876 μm), it is concluded that the second major influencer after the geometry is the particle sizes of the samples.

To provide a deeper understanding, the distinct reactions exhibited by sensors K0 and K5 when exposed to air and acetone gas can be elucidated by analyzing their material composition, surface morphology, and interactions within their immediate surroundings.

a) Response in Air:

Sensor K0: This sensor is made of pristine SnO_2 with an agglomerated particle structure. The non-porous, irregular structure provides limited active sites for gas adsorption and interaction. When exposed to air, oxygen molecules may adsorb onto the available surface sites of the SnO_2 particles. This interaction captures electrons from the material, leading to the formation of electron depletion layers and, subsequently, an increase in resistance. Due to the agglomerated and non-porous nature of K0's structure, the available oxygen adsorption sites are limited, resulting in higher resistance readings.

Sensor K5: This sensor is composed of SnO_2 with a small amount of NiO and features a cauliflower-like, porous morphology. The porous structure significantly increases the available surface area for gas interaction. When exposed to air, the highly porous nature of K5 allows a larger number of oxygen molecules to adsorb onto the surface, leading to the capture of electrons and the creation of electron depletion layers. While the resistance still increases due to oxygen adsorption, the higher number of active sites in the porous structure might mitigate the overall resistance increase compared to K0.

b)   Response to Acetone Gas:

Sensor K0: When exposed to acetone gas, the agglomerated particle structure of K0 offers limited active sites for acetone adsorption and reaction. The non-porous nature hinders efficient gas-surface interactions. As acetone molecules interact with the surface, a limited number of electrons are released back into the material, causing a moderate reduction in resistance. The lack of a highly reactive surface limits the sensor's response to acetone.

Sensor K5: The cauliflower-like, porous morphology of K5 is a key factor here. When exposed to acetone gas, the increased surface area with numerous active sites allows for efficient interaction between acetone molecules and the sensor's surface.

82

The small quantity of NiO might enhance the sensor's selectivity towards acetone. As acetone molecules react with the adsorbed oxygen on the surface, a significant number of electrons are released, causing a substantial reduction in resistance. The highly porous structure amplifies the sensor's sensitivity and response to acetone gas.

Furthermore, as depicted in Figure 4.24, a schematic illustration delineates the sensing mechanism within NiO: SnO_2 samples. Initially, within an ambient air environment, Figure 4.24.a, oxygen molecules (O_2) undergo adsorption onto the surfaces of both the core and the delicate petal-like structures of the cauliflower-like NiO: SnO_2 particles as shown in Equation 4.3. This interaction results in the capture of electrons and the creation of electron depletion layers, visualized in red. Consequently, the sensor's overall resistance experiences an elevation.

$$O_2 + 2e^- \longrightarrow 2O^- \tag{4.3}$$

Upon exposure to acetone gas, Figure 4.24.b, a chemical reaction transpires between the acetone molecules and the adsorbed oxygen analytes shown in Equation 4.4. This reaction culminates in the formation of water and carbon dioxide, consequently liberating electrons back into the material and inducing a dramatical decline in its resistance. The sensor's responsiveness is quantified by computing the ratio of resistance measured in ambient air (R_a) to that obtained in the analyte gas (R_g), R_a / R_g.

$$C_3H_6O + 8O^- \longrightarrow 3H_2O + 3CO_2 \tag{4.4}$$
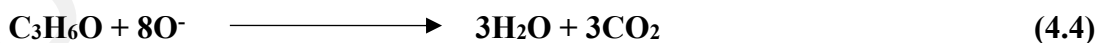
In summary, the differences in material composition and morphology between K0 and K5 play pivotal roles in determining their responses to air and acetone gas. The porous, cauliflower-like structure of K5, along with the inclusion of a small amount of NiO, significantly enhances its sensitivity and reactivity towards both air and acetone gas, leading to pronounced changes in resistance compared to the non-porous and agglomerated structure of K0. This pivotal observation elucidates the rationale behind the

K5 sample's remarkable response—measuring an excellent twofold increase compared to the pristine K0 sample.

a) In air
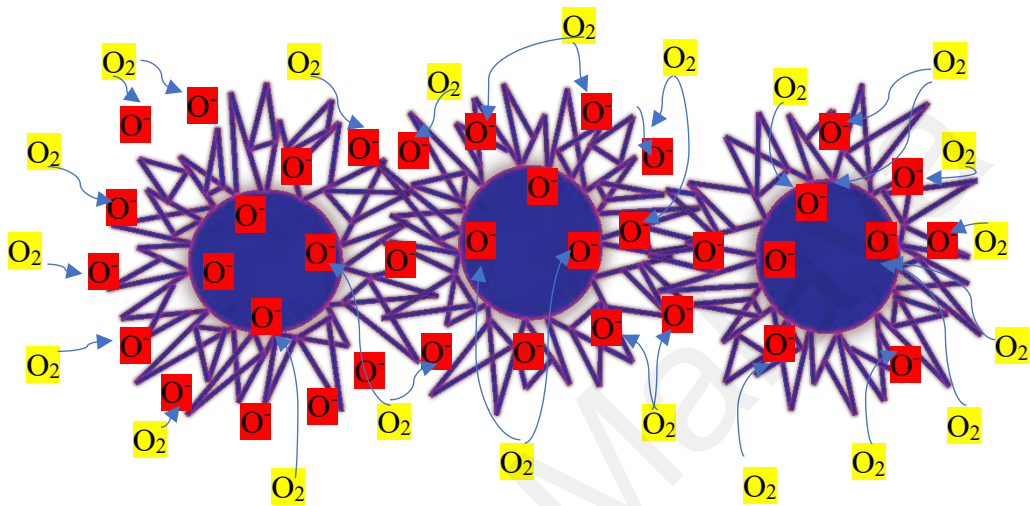
b) In acetone
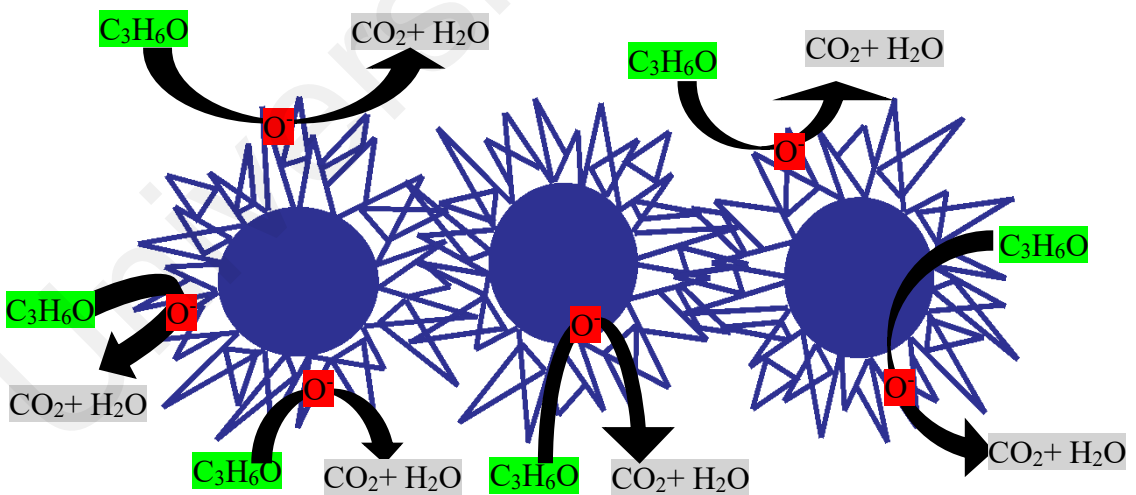
Figure 4.24 Schematic diagram for the sensing mechanism of NiO:SnO$_2$.

4.4   Summary of Gas Sensing

The K5 sensor with the cauliflower-like hierarchy microstructure of NiO: SnO_2 synthesized using a simple and cost-effective hydrothermal method showed great performance in acetone gas sensing, recording a response of 1734 at 1000 ppm at 350 °C. The optimum operating temperature for K5 was determined to be 350 °C, with fast response and recovery times of only 8 seconds and 2 minutes 18 seconds at 20 ppm of acetone, respectively. In addition, Table 4.2 provides a comparative analysis between this study and prior research involving SnO_2 or NiO combined with other materials for acetone detection. It evaluates their respective responses, operating temperatures, as well as response and recovery times towards acetone gas.

Furthermore, K5 demonstrated high selectivity for acetone detection and excellent operational stability over repeated cycles of acetone exposure. Finally, the primary factor contributing to the superior adsorption of analyte gas is the cauliflower-like shape and geometry of the NiO:SnO_2 synthesized particles, which offer a higher surface-to-volume ratio. Additionally, particle size analysis indicates a secondary influence, with smaller particle sizes correlating with higher response levels. Hence, while particle geometry is the primary factor, particle size emerges as a crucial secondary factor influencing the gas sensing performance of NiO:SnO_2 samples.

Table 4.2 Comparative analysis of acetone detection characteristics in SnO₂, and NiO-based sensors: Previous research versus current study.

T_{res}= response time, T_{rec}= recovery time, NA= not applied.

Material	Acetone detection range	Operating temperature (°C)	Response (R_a/R_g) or (R_g/R_a)	T_{res} (Acetone conc.)	T_{rec} (Acetone con.)	Reference
NiO - (0.7 wt% Pt) nanotubes	100 ppm	200	9	NA	NA	(J.Fu et al., 2013)
SnO₂ - (5 wt% Pt) porous fibers	1-3 ppm	300	2-3.5	11 s (0.12 ppm)	6 s (0.12 ppm)	(J.Shin et al., 2013)
SnO₂ porous fibers	1-3 ppm	300	1.63-1.33	NA	NA	(J.Shin et al., 2013)
SnO₂ - (0.05 wt% multi walled carbon nanotubes (MWCNTs)) nanocomposite	0.5- 5ppm	200	20-170	120 s (2.5 ppm)	180 s (2.5 ppm)	(S.Salehi et al., 2014)
SnO₂ - (3.13 wt% reduced graphene oxide (rGO)) film	10-2000 ppm	25	1.02-1.11	107 s (10 ppm)	95 s (10 ppm)	(D.Zhang et al., 2015)
ZnO - (~50 wt% SnO₂) nanofibers	5-40000 ppm	300	13.3-13	19 s (100 ppm)	9 s (100 ppm)	(S.Yan et al., 2015)
SnO₂ - (~1.1 wt% Pd) nanofibers	1-300 ppm	275	4-150	NA	NA	(W.Tang et al., 2015)
ZnO - (8 wt% NiO) microflowers	10-100 ppm	300	3.6-23.5	3 s (100 ppm)	41 s (100 ppm)	(C.Liu et al., 2016)
ZnO - Ni porous templated-maize straw	0.8-800 ppm	275	1.6-85	1 s (100 ppm)	20 s (ppm)	(C.Liu et al., 2017)

Table 4.2 continued.

Material	Acetone detection range	Operating temperature (°C)	Response (R_a/R_g) or (R_g/R_a)	T_{res} (Acetone conc.)	T_{rec} (Acetone con.)	Reference
NiO/ZnO hollow spheres	100 ppm	275	29.8	1 s (100 ppm)	20 s (100 ppm)	(C.Liu et al., 2017)
SnO_2/Au-In_2O_3 core-shell nanoflowers	5-100 ppm	300	3.8-12.1	2 s (100 ppm)	9 s (100 ppm)	(F.Li et al., 2017)
SnO_2 - polypyrrole (PPY) fiber	100 ppm	25	1.05	NA	NA	(S.Bagchi et al., 2017)
ZnO - Ni porous templated-maize straw	1-500 ppm	340	1.8-280	6 s (100 ppm)	2 s (100 ppm)	(X.Zhang et al., 2017)
PdO-NiO/NiCo2O4 truncated nanocages	10-1000 ppm	210	1.34-5.41	19 s (100 ppm)	30 s (100 ppm)	(T.Zhou et al., 2018)
Sm_2O_3/SnO_2 hierarchical structures	0.1-100 ppm	250	1.2-41.1	NA	NA	(Y.Zhang et al., 2018)
SnO_2 doped with N	1-100 ppm	300	7-357	1.19 min (100 ppm)	1.52 min (100 ppm)	(X.Guan et al., 2019)
Co_3O_4 loaded SnO_2 nanowires	0.5- 50 ppm	300	2.6-70	20 s (50 ppm)	122 s (50 ppm)	(H.Kim et al., 2020)
Pt-doped 3D porous SnO_2 nanosheets and micro flowers	50 ppb-1000 ppm	153	2.1-505.7	440 s (50 ppb) 130 s (100 ppm)	370 s (50 ppb) 140 s (100 ppm)	(W.Quan et al., 2020)

Table 4.2 continued.

Material	Acetone detection range	Operating temperature (°C)	Response (R_a/R_g) or (R_g/R_a)	T_{res} (Acetone conc.)	T_{rec} (Acetone con.)	Reference
SnO_2 pod-like micro-nanostructure	1-500 ppm	280	2-28	5 s (100 ppm)	34 s (100 ppm)	(H.Yu et al., 2021)
NiO nanostructures	50-500 ppm	325	2.3-3.4	NA	NA	(S.Kaowphong et al., 2021)
NiO: SnO_2 (Sensor K5) 3D-Cauliflower	**20-1000 ppm**	**350**	**34.7-1734**	**8 s (20 ppm)**	**78 s (20 ppm)**	**This work**

CHAPTER 5: CONCLUSION AND RECOMMENDATIONS

5.1 Conclusion

This research successfully synthesized a highly desirable cauliflower-like hierarchy microstructure of NiO: SnO_2 through a simple and cost-effective hydrothermal method. The resulting microstructures exhibited significantly increased average crystallite size compared to pristine SnO_2. The shape and porosity of the cauliflower-like NiO: SnO_2 particles, characterized by their higher surface-to-volume ratio, are attributed as the primary factor for the enhanced adsorption of the analyte gas compared to the irregular particles in the pristine sample. Employing ImageJ software, sample K5's porosity percentage was found to be about 53.4% while sample K0 had a porosity percentage of about 10.2%. Furthermore, the particle sizes of samples K5, K10, and K25 were evaluated using ImageJ to be 3.7 μm, 4 μm, and 9.44 μm, respectively, with corresponding gas response values at 350 °C for 1000 ppm acetone in nitrogen of 1734, 1373, and 391. This reveals an inversely proportional relationship between the particle size and gas response. Despite the smaller particle size of K0 (0.876 μm) compared to other NiO: SnO_2 samples, it is evident that particle size acts as the second major influencer after geometry in gas sensing.

Moreover, since sensor K5 recorded the highest response compared to the other sensors, sensor K5 was chosen for further performance testing. For acetone gas sensing tests, first, sensor K5 was assessed at a fixed concentration of 200 ppm of acetone in a nitrogen background in various temperatures to determine the optimum operating temperature. At 350°C, sensor K5 exhibited a response of 1734, surpassing values at other temperatures: 5.09, 7.75, 168, 779, 1323, and 1271 at 100, 150, 200, 250, 300, and 400°C, respectively. This indicates that 350°C is the optimal operating temperature for sensor K5. Although lower operating temperatures are typically favored for healthcare

applications, a sensor operating at 350°C could find utility, particularly in medical research or clinical laboratories, where acetone detection in breath analysis samples is essential for diagnosing metabolic disorders like diabetes and ketoacidosis.

Following that, the sensor's performance was meticulously evaluated by measuring its response and recovery times at different concentrations of acetone. For example, at a concentration of 20 ppm of acetone in N_2, the sensor recorded a good response time of 8 seconds and a relatively rapid recovery time of 2 minutes and 18 seconds, highlighting its ability to respond quickly and effectively to changes in acetone concentration. Furthermore, the sensor's responses were measured at various concentrations of acetone, including 1000, 200, 100, 50, and 20 ppm, recording values of 1734, 325, 170, 70, and 35, respectively. These results highlight the sensor's remarkable ability to quickly and efficiently respond to changes in acetone concentration, making it a highly efficient and effective option for acetone detection, particularly at lower concentrations. Next, the selectivity of sensor K5 was examined by exposing it to 200 ppm of acetone, carbon dioxide, ammonia, and ethanol in a nitrogen background at the optimum temperature of 350 °C. The sensor's response to acetone was 142.74, 143.39, and 2.42 times greater than its response to carbon dioxide, ammonia, and ethanol, respectively, demonstrating excellent selectivity for acetone detection. Finally, the durability of sensor K5 was thoroughly evaluated through a series of repeated cycles of exposure and absence to 200 ppm of acetone balanced with N_2. The results revealed that the sensor's responses in cycles 2-5 were consistent, deviating by a mere 4.61 to 6.01% from the initial response. In light of that, the records indicate that the sensor maintains its operational stability and performance at the working temperature, making it an exceptionally durable and reliable option for acetone detection.

These results demonstrate the effectiveness of the as-prepared nickel oxide: tin oxide with high-surface-to-volume ratio nanoparticles for enhanced gas sensor performance, making it a highly sought-after and promising solution for acetone detection.

5.2   Recommendations and Future Work

Despite its critical role in assessing sensor performance, the detection limit (DL) could not be directly tested in this research due to limitations in the experimental setup. Future investigations should prioritize addressing these limitations and devising methodologies to accurately determine the DL of the NiO: SnO_2 nanoparticle-based gas sensor. This endeavor may entail optimizing experimental protocols, calibration procedures, and sensitivity testing methodologies to achieve reliable and reproducible DL measurements. By doing so, valuable insights into the sensor's sensitivity and detection capabilities can be obtained.

Furthermore, it is imperative to investigate the long-term stability of the NiO: SnO_2 nanoparticle-based gas sensor to assess its durability and reliability over extended periods of continuous operation. Future research should center on conducting prolonged stability tests under real-world conditions to evaluate the sensor's performance over time, including potential degradation or drift in sensitivity. Monitoring the sensor's response to acetone or other target gases over an extended period will provide insights into stability factors, such as material degradation, sensor fouling, or environmental influences.

Additionally, exploring the integration of NiO: SnO_2 nanoparticles into sensor arrays presents a promising avenue for enhancing gas detection selectivity and sensitivity, particularly for acetone. By amalgamating multiple sensor elements with distinct sensing materials or operating principles, sensor arrays can offer complementary responses to

various gases, thereby enhancing overall detection accuracy and reliability. Integration into sensor arrays enables simultaneous detection of multiple gases and discrimination between different analytes based on their unique response patterns, facilitating precise and reliable acetone detection for diabetes monitoring.

Moreover, delving into the investigation of novel hybrid nanocomposites incorporating NiO: SnO_2 nanoparticles with materials such as graphene, PEDOT: PSS, nanotubes, or polyaniline (Pani) presents an exciting opportunity to enhance sensor performance through synergistic effects. By combining the unique properties of NiO: SnO_2 nanoparticles with those of other functional materials, researchers can tailor the composition, structure, and properties of hybrid nanocomposites to achieve specific sensing objectives. For instance, graphene-based nanocomposites may provide enhanced electrical conductivity and surface area, while additions of PEDOT: PSS or Pani can improve gas adsorption and catalytic activity. This exploration of novel hybrid nanocomposites could yield sensors with enhanced sensitivity, selectivity, and lower operating temperatures, thereby advancing gas sensing technology for various applications, including diabetes monitoring.

REFERENCES

Abduljawwad, M., Khaleel, M., Ogedengbe, T.S., & Abraheem, S. (2023). Sensors for daily utilization. *International Journal of Electrical Engineering and Sustainability*, 106-119.

Akhir, M. A., Rezan, S., Mohamed, K., Arafat, M., Haseeb, A., & Lee, H. (2019). Synthesis of SnO2 Nanoparticles via Hydrothermal Method and Their Gas Sensing Applications for Ethylene Detection. *Materials Today: Proceedings, 17,* 810-819.

Al-Hardan, N., Abdullah, M., & Aziz, A. A. (2013). Performance of Cr-doped ZnO for acetone sensing. *Applied Surface Science, 270*, 480-485.

Arafat, M. M., Dinan, B., Akbar, S. A., & Haseeb, A. S. (2012). Gas Sensors Based on One Dimensional Nanostructured Metal-Oxides: A Review. *Sensors, 12*(6), 7207-7258.

Arafat, M. M., Haseeb, A. S. M. A., & Akbar, S. A. (2014). Developments in semiconducting oxide-based gas-sensing materials. *Comprehensive Materials Processing, 13*, 205–219.

Asal, M., & Nasirian, S. (2019). Enhanced low-level acetone detection by zinc/tin bimetallic oxides nanocomposite with long-term stability. *Journal of Materials Science: Materials in Electronics, 31*(2), 920-929.

Bagchi, S., & Ghanshyam, C. (2017). Understanding the gas sensing properties of polypyrrole coated tin oxide nanofiber mats. *Journal of Physics D: Applied Physics, 50*(10), 105302.

Baharuddin, A. A., Ang, B. C., Haseeb, A. S. M. A., Wong, Y. C., & Wong, Y. H. (2019). Advances in chemiresistive sensors for acetone gas detection. *Materials science in semiconductor processing, 103*, 104616.

Balamurugan, C., Song, S., & Kim, H. (2018). Enhancing Gas Response Characteristics of Mixed Metal Oxide Gas Sensors. *Journal of the Korean Ceramic Society, 55*(1), 1-20.

Betty, C.A., Choudhury, S., & Shah, A. (2023). Nanostructured metal oxide semiconductors and composites for reliable trace gas sensing at room temperature. *Surfaces and Interfaces, 36*, 102560.

Bharathi, P., Mohan, M. K., Shalini, V., Harish, S., Navaneethan, M., Archana, J., . . . Hayakawa, Y. (2020). Growth and influence of Gd doping on ZnO nanostructures for enhanced optical, structural properties and gas sensing applications. *Applied Surface Science, 499*, 143857.

Bharti, S. P., Singh, E., & Kumar, U. (2017). Synthesis and Characterization of Nickel Doped Tin Oxide Nanoparticles by Hydrothermal Method. *Nanoscience and Nanotechnology Research, 4*(3), 115–119.

Bhowmik, B., Hazra, A., Dutta, K., & Bhattacharyya, P. (2014). Repeatability and Stability of Room-Temperature acetone Sensor Based on TiO2 Nanotubes: Influence of Stoichiometry Variation. *IEEE Transactions on Device and Materials Reliability, 14*(4), 961-967.

Brahma, S., Yeh, Y., Huang, J., & Liu, C. (2021). Cu-doped p-type ZnO nanostructures as unique acetone sensor at room temperature (~25 °C). *Applied Surface Science, 564*, 150351.

Cao, S., Sui, N., Zhang, P., Zhou, T., Tu, J., & Zhang, T. (2022). TiO2 nanostructures with different crystal phases for sensitive acetone gas sensors. *Journal of Colloid and Interface Science, 607*, 357-366.

Cao, W., & Duan, Y. (2006). Breath Analysis: Potential for Clinical Diagnosis and Exposure Assessment. *Clinical Chemistry, 52*(5), 800-811.

Chakraborty, S., & Pal, M. (2019). Highly selective and stable acetone sensor based on chemically prepared bismuth ferrite nanoparticles. *Journal of Alloys and Compounds*, *787*, 1204–1211.

Chang, X., Qiao, X., Li, K., Wang, P., Xiong, Y., Li, X., . . . Xue, Q. (2020). UV assisted ppb-level acetone detection based on hollow ZnO/MoS2 nanosheets core/shell heterostructures at low temperature. *Sensors and Actuators B: Chemical, 317*, 128208.

Chen, Y. J., Xue, X. Y., Wang, Y. G., & Wang, T. H. (2005). Synthesis and ethanol sensing characteristics of single crystalline SnO2 nanorods. *Applied Physics Letters, 87*(23), 233503.

Cheng, P., Lv, L., Wang, Y., Zhang, B., Zhang, Y., Zhang, Y., . . . Xu, L. (2021). SnO2/ZnSnO3 double-shelled hollow microspheres based high-performance acetone gas sensor. *Sensors and Actuators B: Chemical, 332,* 129212.

Choi, S., Katoch, A., Kim, J., & Kim, S. S. (2014). Remarkable Improvement of Gas-Sensing Abilities in p-type Oxide Nanowires by Local Modification of the Hole-Accumulation Layer. *ACS Applied Materials & Interfaces, 7*(1), 647-652.

Deng, C., Zhang, J., Yu, X., Zhang, W., & Zhang, X. (2004). Determination of acetone in human breath by gas chromatography–mass spectrometry and solid-phase microextraction with on-fiber derivatization. *Journal of Chromatography B, 810*(2), 269-275.

Du, Y., Wang, W., Li, X., Zhao, J., Ma, J., Liu, Y., & Lu, G. (2012). Preparation of NiO nanoparticles in microemulsion and its gas sensing performance. *Materials Letters, 68*, 168-170.

Eranna, G., Joshi, B. C., Runthala, D. P., & Gupta, R. P. (2004). Oxide Materials for Development of Integrated Gas Sensors—A Comprehensive Review. *Critical Reviews in Solid State and Materials Sciences, 29*(3-4), 111-188.

Fields, L. L., Zheng, J. P., Cheng, Y., & Xiong, P. (2006). Room-temperature low-power hydrogen sensor based on a single tin dioxide nanobelt. *Applied Physics Letters, 88*(26), 263102.

Fu, J., Zhao,C., Zhang, J., Peng,Y., & Xie, E. (2013). Enhanced gas sensing performance of electrospun Pt-functionalized NiO nanotubes with chemical and electronic sensitization. *ACS applied materials & interfaces*, *5*(15), 7410–7416.

Galassetti, P. R., Novak, B., Nemet, D., Rose-Gottron, C., Cooper, D. M., Meinardi, S., . . . Blake, D. R. (2005). Breath ethanol and acetone as Indicators of Serum Glucose Levels: An Initial Report. *Diabetes Technology & Therapeutics, 7*(1), 115-123.

Gemeinhardt, H., & Sharma, J. (2023). Machine-Learning-Assisted Leak Detection Using Distributed Temperature and Acoustic Sensors. *IEEE Sensors Journal, 24*(2).

Goel, N., Kunal, K., Kushwaha, A., & Kumar, M. (2023). Metal oxide semiconductors for gas sensing. *Engineering Reports, 5*(6), e12604.

Goldoni, A., Alijani, V., Sangaletti, L., & D'arsiè, L. (2018). Advanced promising routes of carbon/metal oxides hybrids in sensors: A review. *Electrochimica Acta, 266*, 139-150.

Gong, H., Zhao, C., Niu, G., Zhang, W., & Wang, F. (2020). Construction of 1D/2D α-Fe2O3/SnO2 Hybrid Nanoarrays for Sub-ppm acetone Detection. *Research,* 1-11.

Guan, X., Wang, Y., Luo, P., Yu, Y., Chen, D., & Li, X. (2019). Incorporating N Atoms into SnO2 Nanostructure as an Approach to Enhance Gas Sensing Property for acetone. *Nanomaterials, 9*(3), 445.

Gunawan, P., Mei, L., Teo, J., Ma, J., Highfield, J., Li, Q., & Zhong, Z. (2012). Ultrahigh Sensitivity of Au/1D α-Fe2O3 to acetone and the Sensing Mechanism. *Langmuir, 28*(39), 14090-14099.

Guo, T., Yao, M., Lin, Y., & Nan, C. (2015). A comprehensive review on synthesis methods for transition-metal oxide nanostructures. *CrystEngComm, 17*(19), 3551-3585.

Gupta, M., Verma, A., Chaudhary, P., & Yadav, B.C. (2023). MXene and their integrated composite-based acetone sensors for monitoring of diabetes. *Materials Advances*.

Hakim, S. A., Liu, Y., Zakharova, G. S., & Chen, W. (2015). Synthesis of vanadium pentoxide nanoneedles by physical vapour deposition and their highly sensitive behavior towards acetone at room temperature. *RSC Advances, 5*(30), 23489-23497.

Haldorai, Y., & Shim, J. (2014). Fabrication of Metal Oxide–Polymer Hybrid Nanocomposites. *Organic-Inorganic Hybrid Nanomaterials Advances in Polymer Science,* 249-281.

Han, D., & Zhao, M. (2020). Facile and simple synthesis of novel iron oxide foam and used as acetone gas sensor with sub-ppm level. *Journal of Alloys and Compounds*, *815*, 152406.

Hu, J., Yang, J., Wang, W., Xue, Y., Sun, Y., Li, P., . . . Chen, Y. (2018). Synthesis and gas sensing properties of NiO/SnO2 hierarchical structures toward ppb-level acetone detection. *Materials Research Bulletin, 102*, 294-303.

Hu, J., Zou, C., Su, Y., Li, M., Yang, Z., Ge, M., & Zhang, Y. (2017). One-step synthesis of 2D C3N4-tin oxide gas sensors for enhanced acetone vapor detection. *Sensors and Actuators B: Chemical*, *253*, 641–651.

Hu, K., Wang, F., Liu, H., Li, Y., & Zeng, W. (2020). Enhanced hydrogen gas sensing properties of Pd-doped SnO2 nanofibres by Ar plasma treatment. *Ceramics International, 46*(2), 1609-1614.

Hübner, M., Simion, C., Tomescu-Stănoiu, A., Pokhrel, S., Bârsan, N., & Weimar, U. (2011). Influence of humidity on CO sensing with p-type CuO thick film gas sensors. *Sensors and Actuators B: Chemical, 153*(2), 347-353.

Jia, Q., Ji, H., Zhang, Y., Chen, Y., Sun, X., & Jin, Z. (2014). Rapid and selective detection of acetone using hierarchical ZnO gas sensor for hazardous odor markers application. *Journal of Hazardous Materials*, *276*, 262–270.

John, R.A.B., & Kumar, A.R. (2023). Tuning the p-type conductivity of NiO for the room temperature formaldehyde detection. *Inorganic Chemistry Communications, 150*, 110445.

Jung, S., Choi, S., & Kim, S. S. (2012). Fabrication and properties of trench-structured networked SnO2 nanowire gas sensors. *Sensors and Actuators B: Chemical,* 171-172, 672-678.

Kaowphong, S., Chachvalvutikul, A., Hongsith, N., Ren, J., & Prasatkhetragarn, A. (2021). Synthesis of NiO Nanostructures by Sonocatalyzed Microwave Irradiation Technique and Their acetone Sensing Properties. *Integrated Ferroelectrics, 214*(1), 205-216.

Kaur, H., Bhatti, H. S., & Singh, K. (2019). Europium doping effect on 3D flower-like SnO2 nanostructures: Morphological changes, photocatalytic performance and fluorescence detection of heavy metal ion contamination in drinking water. *RSC Advances, 9*(64), 37450-37466.

Khomarloo, N., Mohsenzadeh, E., Gidik, H., Bagherzadeh, R., & Latifi, M. (2024). Overall perspective of electrospun semiconductor metal oxides as high-performance gas sensor materials for NOx detection. *RCS Advances, 14*(11), 7806-7824.

Khuspe, G. D., Navale, S. T., Chougule, M. A., & Patil, V. B. (2013). ammonia gas sensing properties of CSA doped PANi-SnO2 nanohybrid thin films. *Synthetic Metals, 185*, 1–8.

Kim, H., Cai, Z., Chang, S. P., & Park, S. (2020). Improved sub-ppm acetone sensing properties of SnO2 nanowire-based sensor by attachment of Co3O4 nanoparticles. *Journal of Materials Research and Technology*, *9*(1), 1129-1136.

Kishore, K. R., Balamurugan, D., & Jeyaprakash, B. G. (2021). CuO nanograins: Synthesis and acetone vapour detection. *Journal of Materials Science: Materials in Electronics, 32*(1), 1204-1220.

Kondo, T., Sato, Y., Kinoshita, M., Shankar, P., Mintcheva, N. N., Honda, M., . . . Kulinich, S. A. (2017). Room temperature ethanol sensor based on ZnO prepared via laser ablation in water. *Japanese Journal of Applied Physics, 56*(8), 080304.

Kononova, I., Moshnikov, V., & Kononov, P. (2023). SnO₂-Based Porous Nanomaterials: Sol-Gel Formation and Gas-Sensing Application. *Gels, 9*(4), 283.

Koo, W., Yu, S., Choi, S., Jang, J., Cheong, J. Y., & Kim, I. (2017). Nanoscale PdO Catalyst Functionalized Co3O4 Hollow Nanocages Using MOF Templates for Selective Detection of acetone Molecules in Exhaled Breath. *ACS Applied Materials & Interfaces, 9*(9), 8201-8210.

Korotcenkov, G. (2007). Metal oxides for solid-state gas sensors: What determines our choice? *Materials Science and Engineering: B, 139*(1), 1-23.

Korotcenkov, G. (2008). The role of morphology and crystallographic structure of metal oxides in response of conductometric-type gas sensors. *Materials Science and Engineering: R: Reports, 61*(1-6), 1-39.

Korotcenkov, G., Macsanov, V., Brinzari, V., Tolstoy, V., & Schwank, J. (2003). NANO-SIZE SnO2 FILMS DEPOSITED BY SILD METHOD: STRUCTURAL AND GAS RESPONSE CHARACTERIZATION. *Physics, Chemistry and Application of Nanostructures*.

Kumar, J. P., Giri, S. D., & Sarkar, A. (2018). Mesoporous NiO with different morphology: Synthesis, characterization and their evaluation for oxygen evolution reaction. *International Journal of Hydrogen Energy, 43*(33), 15639-15649.

Li, E., Cheng, Z., Xu, J., Pan, Q., Yu, W., & Chu, Y. (2009). Indium Oxide with Novel Morphology: Synthesis and Application in C2H5OH Gas Sensing. *Crystal Growth & Design, 9*(5), 2146-2151.

Li, F., Zhang, T., Gao, X., Wang, R., & Li, B. (2017). Coaxial electrospinning heterojunction SnO2/Au-doped In2O3 core-shell nanofibers for acetone gas sensor. *Sensors and Actuators B: Chemical, 252,* 822–830.

Li, G., Su, Y., Chen, X., Chen, L., Li, Y., & Guo, Z. (2019). Enhanced chemiresistive sensing performance of well-defined porous CuO-doped ZnO nanobelts toward VOCs. *Nanoscale Advances, 1*(10), 3900-3908.

Li, S., Zhang, L., Zhu, M., Ji, G., Zhao, L., Yin, J., & Bie, L. (2017). acetone sensing of ZnO nanosheets synthesized using room-temperature precipitation. *Sensors and Actuators B: Chemical, 249*, 611-623.

Li, Z., Huang, Y., Zhang, S., Chen, W., Kuang, Z., Ao, D., . . . Fu, Y. (2015). A fast response & recovery H2S gas sensor based on α-Fe2O3 nanoparticles with ppb level detection limit. *Journal of Hazardous Materials, 300*, 167-174.

Li, Z., Li, H., Wu, Z., Wang, M., Luo, J., Torun, H., . . . Fu, Y. (2019). Advances in designs and mechanisms of semiconducting metal oxide nanostructures for high-precision gas sensors operated at room temperature. *Materials Horizons, 6*(3), 470-506.

Li, Z., Zhang, Y., Zhang, H., & Yi, J. (2021). MOF-derived Au-loaded Co3O4 porous hollow nanocages for acetone detection. *Sensors and Actuators B: Chemical, 344,* 130182.

Liang, S., Li, J., Wang, F., Qin, J., Lai, X., & Jiang, X. (2017). Highly sensitive acetone gas sensor based on ultrafine α-Fe2O3 nanoparticles. *Sensors and Actuators B: Chemical, 238*, 923–927.

Liu, C., Wang, B., Liu, T., Sun, P., Gao, Y., Liu, F., & Lu, G. (2016). Facile synthesis and gas sensing properties of the flower-like NiO-decorated ZnO microstructures. *Sensors and Actuators B: Chemical, 235*, 294-301.

Liu, C., Zhao, L., Wang, B., Sun, P., Wang, Q., Gao, Y., Liang, X., Zhang, T., & Lu, G. (2017). acetone gas sensor based on NiO/ZnO hollow spheres: Fast response and recovery, and low (ppb) detection limit. *Journal of Colloid and Interface Science, 495*, 207–215.

Liu, G., Zhu, L., Yu, Y., Qiu, M., Gao, H., & Chen, D. (2021). WO3 nanoplates for sensitive and selective detections of both acetone and NH3 gases at different operating temperatures. *Journal of Alloys and Compounds, 858*, 157638.

Liu, L., Li, S., Zhuang, J., Wang, L., Zhang, J., Li, H., Liu, Z., Han, Y., Jiang, X., & Zhang, P. (2011). Improved selective acetone sensing properties of Co-doped ZnO nanofibers by electrospinning. *Sensors and Actuators B: Chemical, 155*(2), 782–788.

Liu, M., Song, P., Yang, Z., & Wang, Q. (2021). Hierarchical assembly of SnO2 nanorod on spindle-like α-Fe2O3 for enhanced acetone gas-sensing performance. *Ceramics International, 47*(9), 12181–12188.

Liu, X., Cheng, S., Liu, H., Hu, S., Zhang, D., & Ning, H. (2012). A Survey on Gas Sensing Technology. *Sensors, 12*(7), 9635-9665.

Liu, X., Jiang, L., Jiang, X., Tian, X., Sun, X., Wang, Y., . . . Xu, X. (2018). Synthesis of Ce-doped In2O3 nanostructure for gas sensor applications. *Applied Surface Science, 428*, 478-484.

Lu, X., Zhang, W., Wang, C., Wen, T., & Wei, Y. (2011). One-dimensional conducting polymer nanocomposites: Synthesis, properties and applications. *Progress in Polymer Science, 36*(5), 671-712.

Lu, Y., Ma, Y. H., Ma, S. Y., Jin, W. X., Yan, S. H., Xu, X. L., Jiang, X. H., Wang, T. T., Yang, H. M., Chen, H., & Qiang, Z. (2016b). Synthesis of cactus-like NiO nanostructure and their gas-sensing properties. *Materials Letters, 164*, 48–51.

Lu, Y., Ma, Y., Ma, S., & Yan, S. (2017). Hierarchical heterostructure of porous NiO nanosheets on flower-like ZnO assembled by hexagonal nanorods for high-performance gas sensor. *Ceramics International, 43*(10), 7508-7515.

Madou, M. J., & Morrison, S. R. (1989). Solid/Gas interfaces. *Chemical Sensing with Solid State Devices*, 67–104, Elsevier.

Ma, L., Ma, S. Y., Shen, X. F., Wang, T. T., Jiang, X. H., Chen, Q., Qiang, Z., Yang, H. M., & Chen, H. (2018). PrFeO3 hollow nanofibers as a highly efficient gas sensor for acetone detection. *Sensors and Actuators B: Chemical, 255*, 2546–2554.

Marques, G., & Pitarma, R. (2019). A Cost-Effective Air Quality Supervision Solution for Enhanced Living Environments through the Internet of Things. *Electronics, 8*(2), 170.

Masikini, M., Chowdhury, M., & Nemraoui, O. (2020). Review—Metal Oxides: Application in Exhaled Breath acetone Chemiresistive Sensors. *Journal of The Electrochemical Society, 167*(3), 037537.

Mokoena, T. P., Swart, H. C., & Motaung, D. E. (2019). A review on recent progress of p-type nickel oxide based gas sensors: Future perspectives. J*ournal of Alloys and Compounds, 805*, 267-294.

Murugan, C., Subramanian, E., & Padiyan, D. P. (2014). P–n Heterojunction formation in polyaniline–SnO2 organic–inorganic hybrid composite materials leading to enhancement in sensor functionality toward benzene and toluene vapors at room temperature. *Synthetic Metals, 192*, 106-112.

Narjinary, M., Rana, P., Sen, A., & Pal, M. (2017). Enhanced and selective acetone sensing properties of SnO2-MWCNT nanocomposites: Promising materials for diabetes sensor. *Materials & Design, 115*, 158-164.

Nazemi, H., Joseph, A., Park, J., & Emadi, A. (2019). Advanced Micro- and Nano-Gas Sensor Technology: A Review. *Sensors, 19*(6), 1285.

Park, K., Cho, H., Lee, J., Song, Y., Kim, W., & Choa, Y. (2020). Design of highly porous SnO2-CuO nanotubes for enhancing H2S gas sensor performance. *Sensors and Actuators B: Chemical, 302*, 127179.

Peng, C., Guo, J., Yang, W., Shi, C., Liu, M., Zheng, Y., . . . Yang, Y. (2016). Synthesis of three-dimensional flower-like hierarchical ZnO nanostructure and its enhanced acetone gas sensing properties. *Journal of Alloys and Compounds, 654,* 371-378.

Popa, C., Petrus, M., & Bratu, A. M. (2015). Ammonia and ethylene biomarkers in the respiration of the people with schizophrenia using photoacoustic spectroscopy. *Journal of Biomedical Optics*, *20*(5), 057006.

Quan, W., Hu, X., Min, X., Qiu, J., Tian, R., Ji, P., . . . Zheng, H. (2020). A Highly Sensitive and Selective ppb-Level acetone Sensor Based on a Pt-Doped 3D Porous SnO2 Hierarchical Structure. *Sensors, 20*(4), 1150.

Righettoni, M., Schmid, A., Amann, A., & Pratsinis, S. E. (2013). Correlations between blood glucose and breath components from portable gas sensors and PTR-TOF-MS. *Journal of Breath Research, 7*(3), 037110.

Rodríguez-Torres, M., Altuzar, V., Mendoza-Barrera, C., Beltrán-Pérrez, G., Castillo-Mixcóatl, J., & Mūnoz-Aguirre, S. (2023). Acetone Detection and Classification as Biomarker of Diabetes Mellitus Using a Quartz Crystal Microbalance Gas Array. *Sensors, 23*(24), 9823.

Saeedi, P., Petersohn, I., Salpea, P., Malanda, B., Karuranga, S., Unwin, N., Colagiuri, S., Guariguata, L., Motala, A. A., Ogurtsova, K., Shaw, J. E., Bright, D., & Williams, R. (2019). Global and regional diabetes prevalence estimates for 2019 and projections for 2030 and 2045: Results from the International Diabetes Federation Diabetes Atlas, 9th edition. *Diabetes Research and Clinical Practice, 157*, 107843.

Sakhare, R. D., Khuspe, G. D., Navale, S. T., Mulik, R. N., Chougule, M. A., Pawar, R. C., Lee, C. S., Sen, S., & Patil, V. B. (2013). Nanocrystalline SnO2 thin films: Structural, morphological, electrical transport and optical studies. *Journal of Alloys and Compounds, 563*, 300–306.

Salehi, S., Nikan, E., Khodadadi, A. A., & Mortazavi, Y. (2014). Highly sensitive carbon nanotubes–SnO2 nanocomposite sensor for acetone detection in diabetes mellitus breath. *Sensors and Actuators B: Chemical*, *205*, 261-267.

Shaalan, N., Yamazaki, T., & Kikuta, T. (2011). Influence of morphology and structure geometry on NO2 gas-sensing characteristics of SnO2 nanostructures synthesized via a thermal evaporation method. *Sensors and Actuators B: Chemical, 153*(1), 11-16.

Shao, S., Wu, H., Wang, S., Hong, Q., Koehn, R., Wu, T., & Rao, W. (2015). Highly crystalline and ordered nanoporous SnO2 thin films with enhanced acetone sensing property at room temperature. *J. Mater. Chem. C, 3*(41), 10819-10829.

Simo, A., Kaviyarasu, K., Mwakikunga, B., Mokwena, M., & Maaza, M. (2017). Room temperature volatile organic compound gas sensor based on vanadium oxide 1-dimension nanoparticles. *Ceramics International, 43*(1), 1347-1353.

Shin, J., Choi, S. J., Lee, I., Youn, D. Y., Park, C. O., Lee, J. H., ... & Kim, I. D. (2013). Thin-wall assembled SnO2 fibers functionalized by catalytic Pt nanoparticles and their superior exhaled-breath-sensing properties for the diagnosis of diabetes. *Advanced Functional Materials*, *23*(19), 2357-2367.

Singh, S., Sreelekha, G., Adak, C., Shukla, R.P., & Kabmle, V. (2023). Metal Oxide-based Gas Sensor Array for the VOCs Analysis in Complex Mixtures using Machine Learning.

Song, P., Wang, Q., & Yang, Z. (2012). Preparation, characterization and acetone sensing properties of Ce-doped SnO2 hollow spheres. *Sensors and Actuators B: Chemical, 173*, 839-846.

Suematsu, K., Ma, N., Watanabe, K., Yuasa, M., Kida, T., & Shimanoe, K. (2018). Effect of Humid Aging on the Oxygen Adsorption in SnO2 Gas Sensors. *Sensors, 18*(1), 254.

Sun, H., Saeedi, P., Karuranga, S., Pinkepank, M., Ogurtsova, K., Duncan, B. B., Stein, C., Basit, A., Chan, J. C. N., Mbanya, J. C., Pavkov, M. E., Ramachandaran, A., Wild, S. H., James, S., Herman, W. H., Zhang, P., Bommer, C., Kuo, S., Boyko, E. J., & Magliano, D. J. (2022). IDF Diabetes Atlas: Global, regional and country-level diabetes prevalence estimates for 2021 and projections for 2045. *Diabetes Research and Clinical Practice, 183*, 109119.

Sun, P., Zhao, W., Cao, Y., Guan, Y., Sun, Y., & Lu, G. (2011). Porous SnO2 hierarchical nanosheets: Hydrothermal preparation, growth mechanism, and gas sensing properties. *CrystEngComm, 13*(11), 3718.

Tan, Y., & Zhang, J. (2023). Highly sensitive ethanol gas sensors based on Co-doped SnO2 nanobelts and pure SnO2 nanobelts. *Physica E: Low-dimensional systems and Nanostructures, 147*, 115604.

Tang, W., Wang, J., Qiao, Q., Liu, Z., & Li, X. (2015). Mechanism for acetone sensing property of Pd-loaded SnO2 nanofibers prepared by electrospinning: Fermi-level effects. *Journal of Materials Science, 50*(6), 2605-2615.

Tian, K., Wang, X., Yu, Z., Li, H., & Guo, X. (2017). Hierarchical and Hollow Fe2O3 Nanoboxes Derived from Metal–Organic Frameworks with Excellent Sensitivity to H2S. *ACS Applied Materials & Interfaces, 9*(35), 29669-29676.

Tofighi, G., Degler, D., Junker, B., Müller, S., Lichtenberg, H., Wang, W., . . . Grunwaldt, J. (2019). Microfluidically synthesized Au, Pd and AuPd nanoparticles supported on SnO2 for gas sensing applications. *Sensors and Actuators B: Chemical, 292*, 48-56.

Turner, C., Walton, C., Hoashi, S., & Evans, M. (2009). Breath acetone concentration decreases with blood glucose concentration in type I diabetes mellitus patients during hypoglycaemic clamps. *Journal of Breath Research, 3*(4), 046004.

Ulanowska, A., Kowalkowski, T., Trawińska, E., & Buszewski, B. (2011). The application of statistical methods using VOCs to identify patients with lung cancer. *Journal of Breath Research*, *5*(4), 046008.

Vanalakar, S. A., Gang, M. G., Patil, V. L., Dongale, T. D., Patil, P. S., & Kim, J. H. (2018). Enhanced Gas-Sensing Response of Zinc Oxide Nanorods Synthesized via Hydrothermal Route for nitrogen Dioxide Gas. *Journal of Electronic Materials, 48*(1), 589-595.

Walker, J. M., Akbar, S. A., & Morris, P. A. (2019). Synergistic effects in gas sensing semiconducting oxide nano-heterostructures: A review. *Sensors and Actuators B: Chemical, 286*, 624-640.

Wang, C., Liu, J., Yang, Q., Sun, P., Gao, Y., Liu, F., Zheng, J., & Lu, G. (2015). Ultrasensitive and low detection limit of acetone gas sensor based on W-doped NiO hierarchical nanostructure. *Sensors and Actuators B: Chemical, 220*, 59–67.

Wang, P., Wang, D., Zhang, M., Zhu, Y., Xu, Y., Ma, X., & Wang, X. (2016). ZnO nanosheets/graphene oxide nanocomposites for highly effective acetone vapor detection. *Sensors and Actuators B: Chemical, 230*, 477–484.

Wei, S., Zhao, G., Du, W., & Tian, Q. (2016). Synthesis and excellent acetone sensing properties of porous WO 3 nanofibers. *Vacuum, 124*, 32–39.

Wei, S., Zhou, M., & Du, W. (2011). Improved acetone sensing properties of ZnO hollow nanofibers by single capillary electrospinning. *Sensors and Actuators B: Chemical, 160*(1), 753–759.

Witkiewicz, Z., Jasek, K., & Grabka, M. (2023). Semiconductor gas sensors for detecting chemical warfare agents and their stimulants. *Sensors, 23*(2), 3272.

Wongrat, E., Chanlek, N., Chueaiarrom, C., Thupthimchun, W., Samransuksamer, B., & Choopun, S. (2017). acetone gas sensors based on ZnO nanostructures decorated with Pt and Nb. *Ceramics International, 43*, S557-S566.

Wu, D., Li, C., Kong, Q., Shi, Z., Zhang, D., Wang, L., . . . Lin, Q. (2018). Photocatalytic activity of Lu 3 /TiO 2 prepared by ball milling method. *Journal of Rare Earths, 36*(8), 819-825.

Xiao, X., Liu, L., Ma, J., Ren, Y., Cheng, X., Zhu, Y., . . . Deng, Y. (2018). Ordered Mesoporous Tin Oxide Semiconductors with Large Pores and Crystallized Walls for High-Performance Gas Sensing. *ACS Applied Materials & Interfaces, 10*(2), 1871-1880.

Xiaoxi, H.E., Hongfeng, C.H.A.I., Yifan, L.U.O., Lingfeng, M.I.N., Debliquy, M., & Zhang, C. (2023). Metal oxide semiconductor gas sensing materials for early lung cancer diagnosis. *Journal of Advanced Ceramics, 12*(2).

Xiong, Y., Zhu, Z., Ding, D., Lu, W., & Xue, Q. (2018). Multi-shelled ZnCo2O4 yolk-shell spheres for high-performance acetone gas sensor. *Applied Surface Science, 443*, 114–121.

Xu, K., Duan, S., Tang, Q., Zhu, Q., Zhao, W., Yu, X., . . . Yuan, C. (2019). P–N heterointerface-determined acetone sensing characteristics of α-MoO3@NiO core@shell nanobelts. *CrystEngComm, 21*(38), 5834-5844.

Xu, S., Zhang, H., Qi, L., & Xiao, L. (2019). Conductometric acetone vapor sensor based on the use of gold-doped three-dimensional hierarchical porous zinc oxide microspheres. *Microchimica Acta, 186*, 1-8.

Xu, Y., Zheng, L., Yang, C., Liu, X., & Zhang, J. (2020). Highly sensitive and selective electronic sensor based on Co catalyzed SnO2 nanospheres for acetone detection. *Sensors and Actuators B: Chemical, 304*, 127237.

Yan, S. H., Ma, S. Y., Xu, X. L., Li, W. Q., Luo, J., Jin, W. X., ... & Song, H. S. (2015). Preparation of SnO2–ZnO hetero-nanofibers and their application in acetone sensing performance. *Materials Letters*, *159*, 447-450.

Yang, B., Myung, N. V., & Tran, T. (2021). 1D Metal Oxide Semiconductor Materials for Chemiresistive Gas Sensors: A Review. *Advanced Electronic Materials, 7*(9), 2100271.

Yoo, R., Güntner, A. T., Park, Y., Rim, H. J., Lee, H.-S., & Lee, W. (2019). Sensing of acetone by Al-doped ZnO. *Sensors and Actuators B: Chemical, 283*, 107–115.

Yu, H., Zhang, Y., Dong, L., & Wang, J. (2021). Fabricating pod-like SnO2 hierarchical micro-nanostructures for enhanced acetone gas detection. *Materials Science in Semiconductor Processing, 121*, 105451.

Yuan, Z., Li, R., Meng, F., Zhang, J., Zuo, K., & Han, E. (2019). Approaches to Enhancing Gas Sensing Properties: A Review. *Sensors, 19*(7), 1495.

Yunusa, Z., Hamidon, Mohd. N., Kaiser, A., & Awang, Z. (2014). Gas Sensors: A *Review. Sensors & Transducers, 168*(4), 61–75.

Zeng, Y., Zhang, T., Yuan, M., Kang, M., Lu, G., Wang, R., Fan, H., He, Y., & Yang, H. (2009). Growth and selective acetone detection based on ZnO nanorod arrays. *Sensors and Actuators B: Chemical*, *143*(1), 93–98.

Zhang, D., Liu, A., Chang, H., & Xia, B. (2015). Room-temperature high-performance acetone gas sensor based on hydrothermal synthesized SnO2-reduced graphene oxide hybrid composite. *Rsc Advances*, *5*(4), 3016-3022.

Zhang, D., Yang, Z., Wu, Z., & Dong, G. (2019). Metal-organic frameworks-derived hollow zinc oxide/cobalt oxide nanoheterostructure for highly sensitive acetone sensing. *Sensors and Actuators B: Chemical, 283*, 42-51.

Zhang, L., Dong, B., Xu, L., Zhang, X., Chen, J., Sun, X., Xu, H., Zhang, T., Bai, X., Zhang, S., & Song, H. (2017). Three-dimensional ordered ZnO–Fe3O4 inverse opal gas sensor toward trace concentration acetone detection. *Sensors and Actuators B: Chemical*, *252*, 367–374.

Zhang, N., Yu, K., Li, Q., Zhu, Z. Q., & Wan, Q. (2008). Room-temperature high-sensitivity H2S gas sensor based on dendritic ZnO nanostructures with macroscale in appearance. *Journal of Applied Physics, 103*(10), 104305.

Zhang, S., Jiang, W., Li, Y., Yang, X., Sun, P., Liu, F., Yan, X., Gao, Y., Liang, X., Ma, J., & Lu, G. (2019). Highly-sensitivity acetone sensors based on spinel-type oxide (NiFe2O4) through optimization of porous structure. *Sensors and Actuators B: Chemical*, *291*, 266–274.

103

Zhang, S., Yang, M., Liang, K., Turak, A., Zhang, B., Meng, D., . . . Yang, M. (2019). An acetone gas sensor based on nanosized Pt-loaded Fe2O3 nanocubes. *Sensors and Actuators B: Chemical, 290*, 59-67.

Zhang, X., Dong, Z., Liu, S., Shi, Y., Dong, Y., & Feng, W. (2017). Maize straw-templated hierarchical porous ZnO: Ni with enhanced acetone gas sensing properties. *Sensors and Actuators B: Chemical*, *243*, 1224-1230.

Zhang, X., Wang, W., Zhang, D., Mi, Q., & Yu, S. (2021). Self-powered ethanol gas sensor based on the piezoelectric Ag/ZnO nanowire arrays at room temperature. *Journal of Materials Science: Materials in Electronics, 32*(6), 7739-7750.

Zhang, Y., Zhou, L., Liu, Y., Liu, D., Liu, F., Liu, F., Yan, X., Liang, X., Gao, Y., & Lu, G. (2018). Gas sensor based on samarium oxide loaded mulberry-shaped tin oxide for highly selective and sub ppm-level acetone detection. *Journal of Colloid and Interface Science, 531*, 74–82.

Zhang, Z., Zhu, L., Wen, Z., & Ye, Z. (2017). Controllable synthesis of Co3O4 crossed nanosheet arrays toward an acetone gas sensor. *Sensors and Actuators B: Chemical*, *238*, 1052–1059.

Zhang, Z.A., Nie, L.F., Zhou, Q., Song, Z.D., & Pan, G.B. (2023). Chemiresistive H2S gas sensors based on composites of ZnO nanocrystals and foam-like GaN fabricated by photoelectrochemical etching and a sol-gel method. *Sensors and Actuators B: Chemical, 393*, 134148.

Zhao, C., Fu, J., Zhang, Z., & Xie, E. (2013). Enhanced ethanol sensing performance of porous ultrathin NiO nanosheets with neck-connected networks. *RSC Advances, 3*(12), 4018.

Zhao, Y., Sun, Y., Yin, X., Yin, G., Wang, X., Jia, F., & Liu, B. (2018). Effect of Surfactants on the Microstructures of Hierarchical SnO2 Blooming Nanoflowers and their Gas-Sensing Properties. *Nanoscale Research Letters, 13*(1).

Zhou, T., Liu, X., Zhang, R., Wang, Y., & Zhang, T. (2018). NiO/NiCo2O4 truncated nanocages with PdO catalyst functionalization as sensing layers for acetone detection. *ACS applied materials & interfaces*, *10*(43), 37242-37250.

Zhou, T., Zhang, T., Deng, J., Zhang, R., Lou, Z., & Wang, L. (2017). p-type Co3O4 nanomaterials-based gas sensor: Preparation and acetone sensing performance. *Sensors and Actuators B: Chemical, 242,* 369-377.

Zhou, X., Cheng, X., Zhu, Y., Elzatahry, A. A., Alghamdi, A., Deng, Y., & Zhao, D. (2018). Ordered porous metal oxide semiconductors for gas sensing. *Chinese Chemical Letters, 29*(3), 405-416.

Zhu, G., Xi, C., Xu, H., Zheng, D., Liu, Y., Xu, X., & Shen, X. (2012). Hierarchical NiO hollow microspheres assembled from nanosheet-stacked nanoparticles and their application in a gas sensor. *RSC Advances, 2*(10), 4236.

Zhu, L., Li, Y., & Zeng, W. (2017). Enhanced ethanol sensing and mechanism of Cr-doped ZnO nanorods: Experimental and computational study. *Ceramics International, 43*(17), 14873-14879.